Development of efficient and practical numerical tools for the Overall Interaction Concept approach

Mémoire

Amir Elmaraghy

Maîtrise en génie civil - avec mémoire
Maître ès sciences (M. Sc.)

Québec, Canada

Development of efficient and practical numerical tools for the Overall Interaction Concept approach

Thesis

Amir Elmaraghy

Under the supervision of:

Nicolas Boissonnade, directeur de recherche

Mario Fafard, codirecteur de recherche

Résumé

Le concept O.I.C. (Overall Interaction Concept) permet de vérifier la résistance et la stabilité des membrures selon une approche purement numérique. Cette approche a été utilisée, dans une étude précédente, afin de quantifier l'apport positif d'une force de tension sur la résistance et stabilité d'une membrure en flexion. La méthode de l'O.I.C. requiert le multiplicateur plastique de la section afin de calculer l'élancement de la pièce λ ainsi que le facteur khi χ. L'étude précédente omettait, par manque d'outils numériques, les efforts de cisaillement dans le calcul de la résistance plastique des membrures. Cela causait des résultats imprécis pour les membrures courtes. Le travail effectué dans cette étude est alors en deux volets: i) Développer un outil numérique permettant de calculer la résistance plastique des sections symmétriques et non symmétriques selon des efforts provoquant des contraintes axiales et des contraintes de cisaillement et ii) Utiliser cet outil afin de calculer la résistance et la stabilité de membrures en traction ayant des charges transversales provoquant de la flexion et du cisaillement. Le développement de l'outil numérique permettant le calcul de la résistance plastique sous contraintes axiales et de cisaillement a été complété avec succès. L'utilisation de cet outil a permis de confirmer l'influence non négligeable du cisaillement sur la résistance plastique des poutres courtes et ainsi améliorer les résultats de la méthode O.I.C. pour les membrures en tension et flexion.

Abstract

The O.I.C. concept is a numerical approach that calculates the overall resistance and stability of a member. This approach has been used in a previous study on the beneficil effect of a tension load on the overall resistance and stability of a member in flexure. The O.I.C. method requires the plastic multiplication factor of the cross-section to calculate the member slenderness λ and the khi factor χ. Altough, the previous study omitted the shear internal forces in the plastic capacity of the cross-section due to a lack of numerical tools. For short members where shear internal forces were dominant, the resistance and stability results were imprecise. The present work is divided in two main objectives: i) To develop a numerical tool to calculate the plastic capacity of doubly and mono-symmetric cross-sections for axial and shear loads and ii) Use the developed numerical tool to consider the shear internal forces effects for members under tension and bending. The cross-section plastic capacity tool has been successfully developed. The tool has also confirmed the non-negligeable influence of shear loads on the plastic capacity of short members. The short members resistance and stability results were imporved using the numerical tool.

Table of contents

List of figures

List of tables

Abbreviations and symbols

Abbreviations

E.N.A.: Elastic Neutral Axis

F.E.M.: Finite Element Method

F.N.R.: Full Newton-Raphson

M.N.R.: Modified Newton-Raphson

O.I.C.: Overall Interaction Concept

P.I.F.: Partial Internal Forces method

P.N.A.: Plastic Neutral Axis

Chapter 1

α, β: Constants defined in the Eurocode 3 for the bi-axial formula.

Φ: Reduction coefficient defined in the standards.

γ_{mo}: Coefficient defined in the Eurocode 3 standard.

χ_L: Cross-section local buckling factor.

χ_{L+G}: Cross-section local and global buckling factor.

λ_L: Cross-section local relative slenderness.

λ_{L+G}: Member local and global relative slenderness.

ρ: Bending moment reduction factor defined in the Eurocode 3 standard.

τ_y: Shear yield stress.

A, A_g: Gross cross-section area.

A_w, A_v: Shear area of cross-section.

b: I-beam flange width.

b / t: Plate slenderness ratio calculated with the width and the thickness of a plate.

C_f: Factored axial loads applied to the member.

C_y: Axial plastic capacity of the cross-section.

F_s: Ultimate shear stress.

f_y: Material yield stress.

m: number of fiber divisions along the plate long side.

$M_{N,y,Rd}$, $M_{N,z,Rd}$: Reduced plastic bending moment capacity considering the applied axial loads, respectively in the major-axis and minor-axis.

$M_{y,Ed}$, $M_{z,Ed}$: Factored bending moments applied to the member, respectively in the major-axis and minor-axis.

$M_{pl,y,Rd}$, $M_{pl,z,Rd}$: Plastic bending moment resistance of a member, respectively in the major-axis and minor-axis.

$M_{y,V,Rd}$: Reduced major-axis plastic bending moment capacity considering the applied shear loads.

M_{fx}, M_{fy}: Factored major-axis and minor-axis bending moments applied to the member.

M_{px}, M_{py}: Plastic bending moment resistance of a member, respectively in the major-axis and minor-axis in the CSA S16 standard.

M_r: Bending moment resistance of a member.

n: number of fiber divisions along the plate thickness.

N_{Ed}: Factored axial loads applied to the member.

$N_{pl,Rd}$: Axial plastic capacity of the cross-section.

r: Cross-section filet radius.

R_{pl}: Load multiplier to reach the plastic resistance of a cross-section.

$R_{cr,L}$: Load multiplier to reach the local buckling resistance of a cross-section.

$R_{cr,G}$: Load multiplier to reach the global buckling resistance of a member.

R_{ult}: Ultimate member resistance considering local cross-section and global member instabilities.

t_f: I-beam flange thickness.

t_w: I-beam web thickness.

V_r: Shear resistance of a member.

V_{Ed}: Factored shear loads applied to the member.

$V_{pl,Rd}$: Shear plastic capacity of the cross-section.

$W_{pl,y}$: Major-axis plastic section modulus of a cross-section.

Z, Z_y, Z_z: Plastic cross-section modulus in the defined direction.

Chapter 2

$\{\Delta\varepsilon\}$: The vector of incremental strains.

$\Delta\varepsilon_o$: Incremental axial load strain.

ε_p: Total equivalent plastic strain.

ε_u: Maximum allowable strain of a fiber in the R_{pl} program.

ε_x: Axial strain used to determine the axial stress using a stress-strain material law.

ε_{xi}: Axial strain of an individual fiber.

ε_{xi-1}: Cumulative axial strain of an individual fiber at the last iteration.

$\Delta\varepsilon_{xi}$: Incremental axial strain of an individual fiber at the current iteration.

γ_i: Shear strain of an individual fiber.

γ_{oct}: Octahedral shear strain.

$\gamma_{xy}, \gamma_{yz}, \gamma_{zx}$: Engineering shear strains.

λ: Load step factor in a non-linear analysis.

ω_i: Individual fiber warping function.

$\Delta\varphi_y$: Incremental bending moment curvature around the Y-axis.

$\Delta\varphi_z$: Incremental bending moment curvature around the Z-axis.

σ_x: Axial stress determined using a stress-strain material law.

σ_{xi}: Axial stress of an individual fiber.

σ_{VM}: The von Mises yield criterion.

τ_i: Shear stress of an individual fiber.

τ_{oct}: Octahedral shear stress.

τ_{pl}: Shear yield stress of a material.

τ_{xy}, τ_{xy_i}: - Shear stress in the Y-axis direction.

- Shear stress of an individual fiber in the Y-axis direction.

τ_{xz}, τ_{xz_i}: - Shear stress in the Z-axis direction.

- Shear stress of an individual fiber in the Z-axis direction.

A_i: Individual fiber area.

B_w: The warping bi-moment

E: Young Modulus.

E_p: Young Modulus of a material in the plastic range.

E_t: Tangent Young Modulus for a given set of stress and strain values.

E_{t_i}: Individual fiber Tangent Young Modulus for a given set of stress and strain values.

$\{F_{ext}\}$: External force vector in the Tangent Stifness method.

$\{F_{int}\}$: Internal force vector in the Tangent Stifness method.

$\{F_{tot}\}$: Total load vector to be applied on the cross-section in the Tangent Stifness method.

G: Shear Modulus.

I_i: Individual fiber second moment of inertia.

I_{yy}: Second moment of inertia around the Y-axis.

I_{zz}: Second moment of inertia around the Z-axis.

J_2: Second invariant of the stress deviator tensor.

k: The yield stress in pure shear of the material.

$[K_{cs}]$: The tangent stiffness matrix.

M_y: Numerically integrated internal bending moment around the Y-axis of the cross-section.

M_z: Numerically integrated internal bending moment around the Z-axis of the cross-section.

N: Numerically integrated internal axial load over the cross-section.

q: Shear flow of a cross-section.

Q: First moment of inertia of the cross-section.

$\{R\}$: The unbalanced force vector in the Tangent Stifness method.

R_N: Resultant axial force from the numerical integration of the fibers.

R_{My}: Resultant bending moment around the Y-axis from the numerical integration of the fibers.

R_{Mz}: Resultant bending moment around the Z-axis from the numerical integration of the fibers.

V: Integrated shear load of a cross-section in the proper direction.

V_y: Integrated shear load of a cross-section in the Y-axis direction.

V_z: Integrated shear load of a cross-section in the Z-axis direction.

$y_{cg,i}$: Individual fiber position along the Y-axis relative to the cross-section center of gravity.

y_i: Individual fiber position along the Y-axis relative to a given reference point.

$z_{cg,i}$: Individual fiber position along the Z-axis relative to the cross-section center of gravity.

z_i: Individual fiber position along the Z-axis relative to a given reference point.

Chapter 3

h: Height of cross-section.

L: Length of member in a 3D model.

M_{yp}: Numerically integrated plastic bending moment capacity around the Y-axis of the cross-section.

M_{zp}: Numerically integrated plastic bending moment capacity around the Z-axis of the cross-section.

N_p: Numerically integrated plastic axial force capacity of the cross-section.

V_{yp}: Numerically integrated plastic shear capacity of a cross-section in the Y-axis direction.

Chapter 4

b_{ft}: Top flange width of an I-beam.

b_{fb}: Bottom flange width of an I-beam.

M_y: Interaction curve intermediate bending moment loading around the Y-axis.

M_z: Interaction curve intermediate bending moment loading around the Z-axis.

N: Interaction curve intermediate axial loading.

t_{ft}: Top flange thickness of an I-beam.

t_{fb}: Bottom flange thickness of an I-beam.

V_y: Interaction curve intermediate shear load along the Y-axis.

w: Web thickness of an I-beam.

Chapter 5

β: Ratio of the tension load over the applied bending moment.

λ_G, λ_{MB}: Member global relative slenderness.

χ_G, χ_{MB}: Global member buckling factor.

χ_{LT}: Global buckling factor for governing lateral-buckling cases.

λ_{LT}: Member slenderness for governing lateral-buckling cases.

M_{cr}: Critical bending moment capacity.

$M_{pl,Rk}$: Cross-section plastic capacity under pure major-axis bending.

$M_{pl,N,Rk}$: Cross-section plastic capacity under axial load and major-axis bending.

M_u: Ultimate member capacity calculated using 3D shell elements models.

M_z: Applied bending moment load.

N_t: Applied tension load.

q: Transversal uniforme load intensities.

R_{cr}: Critical instability load multiplier.

$R_{cr(N,M,V)}$: Critical instability load multiplier for axial, bending and shear loads.

$R_{pl(N,M,V)}$: Cross-section plastic capacity load multiplier for axial, bending and shear loads.

R_u: Ultimate member resistance capacity load multiplier.

$R_{u(N,M,V)}$: Ultimate resistance capacity load multiplier for axial, bending and shear loads.

Acknowledgments

I would like to sincerely thank Mr. Nicolas Boissonnade and Mr. Mario Fafard for their support leading to the completion of this study. Their valuable help and expertise allowed me to learn advanced notions in the field of steel structures and numerical procedures. I would also like to specifically aknowledge the countless hours that Mr. Boissonnade spent sharing his knowledge in a productive and pleasant environnement.

I would also like to sincerely thank my family for their support and patience throughout this work. Your support and encouragements gave me not only the motivation to complete this work, but the perfect environnement to do so.

Introduction

The use of steel in the construction industry has been strong since many years. Steel structures have multiple advantages during and after the life expectancy of the structure. The erection process of steel structure can be done quickly as the members are pre-fabricated and simple to assemble. Steel is also able to withstand great loads while being lighter than other types of materials. Also, the ductile behavior of steel is beneficial for the safety of the structure. Since this material has been in use for a good number of years, engineers have developed an extensive knowledge on the design of such structures. Although the design and resistance of steel structures and their components are well covered through the standards, the advances in high strength steel will require further knowledge, design approaches and advanced numerical tools.

As of today, the various standards typically define four buckling resistance classes, according to the cross-section slenderness. The *b / t* ratios of the constituting plates of the cross-section define the analysis methodology to be used. For a simple beam under major-axis bending, the buckling resistance curve, as shown in Figure 1, has three distinct zones: fully plastic, inelastic and elastic.

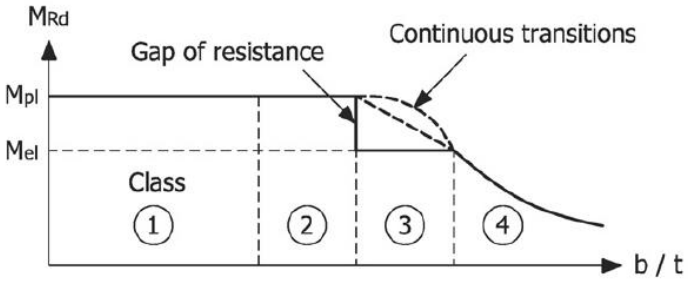

Figure 1 – Major-axis bending buckling resistance (Boissonnade, Hayeck, Saloumi, & Nseir, 2017)

The first zone is characterized by class 1 compact members where the instabilities does not affect the resistance; therefore, a plastic analysis may be performed. The second zone, representing class 2 cross-sections, is where inelastic buckling occurs as a combination of pure section resistance and instability. The third zone represents the response of slender elements with class 3 cross-sections and is governed by elastic buckling. For members having class 4 cross-sections, the effective properties must be calculated and used for the design.

Because the structures are increasing in complexity and size, the use of performant materials will become of prime importance. While a lot of research has been conducted about local and global instabilities of regular steel members, the advancement of high strength steel poses a new subject of research. The reduced plate thicknesses of high strength steel cross-sections will require new methods of predicting the resistance of a given member. The method will have to treat adequately the local and global resistance behavior of a structural member. Such new method is the Overall Interaction Concept (O.I.C.). Within the O.I.C., the resistance of the member may be characterized by an interaction between the cross-section resistance and the member instability

The general O.I.C. procedure is shown in Figure 2. The process can be separated in two main steps: cross-sectional local behavior and member global behavior. First, the cross-section plastic capacity, for a given load set, is computed. This factor, R_{pl}, corresponds to the maximum plastic capacity of the cross-section, without considering any instabilities. The global member behavior design check requires the calculation of the global buckling factor $R_{cr,G}$. This factor uses the first global eigenmode shape to characterize the member instability. If no cross-sectional local instabilities are considered χ_L, which will be the case in the context of this work, the global khi factor χ_{L+G} is calculated by dividing the member ultimate resistance factor R_{ult} by the cross-section plastic factor R_{pl}.

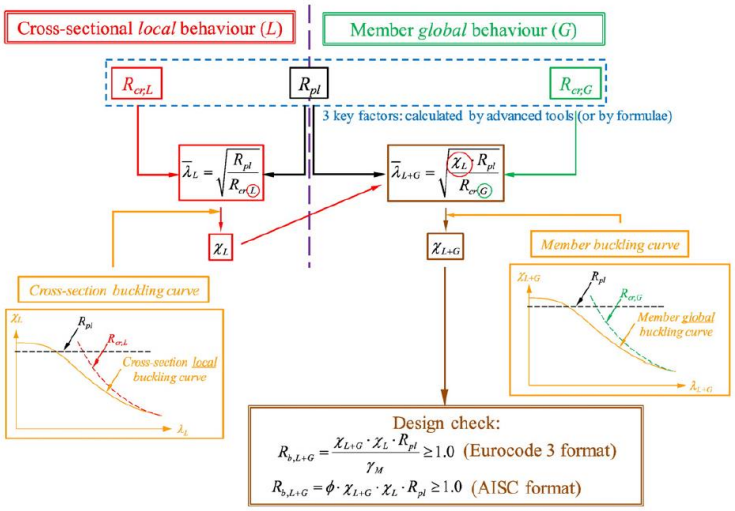

Figure 2 – O.I.C. design flowchart

Following the O.I.C. concept, the development of adequate tools is required. Although the tools themselves will incorporate complex theories and internal procedures, they will have to

not only be accurate but also simple to use. In the context of this work, the tool developed will carry the plastic capacity of cross-sections R_{pl}. To demonstrate the developed tool within the course of this work, the case of members under axial loading and bending moments will be studied.

Depending on the loading configuration of a member, tensile or compressive forces may have either a positive or negative effect on the overall resistance of the member. Two prior master thesis have been working on that specific subject (Silva, 2013) and (Epiney, 2015). The work of (Epiney, 2015) adopted the O.I.C. framework. At the cross-sectional level, the bending capacity is reduced by both type of axial loading. However, the axial load direction has an influence on the critical bending moment of the member. The negative effect of compressive forces on the bending resistance of members is usually well covered in the standards but less so for the beneficial effect of tensile forces. This thesis will refine the results provided by the work of (Epiney, 2015) by using improved tools to consider the effect of shear forces, caused by transversal loads, on the overall tension and bending resistance of members. This thesis will elaborate on the O.I.C. design method by describing the work already done within the method framework and improved tools will be developed to achieve a practical yet powerful use of the method.

In summary, the main goal of this work will be to develop and validate an advanced tool on the plastic capacity of cross-sections specifically adapted to suit the O.I.C. framework. First, the state-of-the-art on the plastic capacity calculations of cross-sections will be described. With the proper objectives regarding the tool capacities, the methodology to program the tool will be defined. The fundamental theory and characteristics of the developed tool will be described. From there, a validation study will be conducted to validate the programmed tool. With the confirmation of the tool's validity, a study on the beneficial effects of tensile loading on the resistance of member in bending will be conducted.

Chapter 1 – State-of-the-art and methodology

The following chapter will review the available literature on the plastic capacity of cross-sections. First, a review of the methods proposed in selected standards will be done. Then, a review of the available numerical methods will be performed. This study will demonstrate the limitations of current methods and highlight the necessity to develop an advanced cross-section plastic capacity tool. The development objectives of the plastic capacity tool will be defined from the information gathered in this chapter.

1.1 – Provisions in design standards

1.1.1 – CSA S16

This section will describe the provisions on the plastic capacity of cross-sections in the Canadian steel standard CSA S16. For class 1 and 2 sections, the plastic interaction equation for axial and biaxial bending forces is shown in equation (1).

$$\frac{C_f}{C_y} + 0.85\frac{M_{fx}}{M_{px}} + 0.6\frac{M_{fy}}{M_{py}} \leq 1.0$$
$$\frac{M_{fx}}{M_{px}} + \frac{M_{fy}}{M_{py}} \leq 1.0 \quad (1)$$

where M_{fx}, M_{fy} and C_f are, respectively, the major-axis and minor-axis factored moments and the factored axial load applied to the cross-section. M_{px}, M_{py} and C_y are, respectively, the major-axis and minor-axis bending moment plastic capacities and the axial plastic capacity of the cross-section. To calculate the plastic resisting moments of the member, the following formula is used:

$$M_p = \varphi Z f_y \quad (2)$$

where Z represents the plastic section modulus and f_y the yield stress. The reduction factor, in the context of this study, will be defined as $\Phi=1$. The axial plastic capacity is calculated using the following formula:

$$C_y = \varphi A_g f_y \quad (3)$$

where A_g represents the gross area of the cross-section.

Equation (1) is a linear combination of the following equations:

$$\frac{C_f}{C_y} + 0.85\frac{M_{fx}}{M_{px}} \leq 1.0 \tag{4}$$

$$\frac{C_f}{C_y} + 0.6\frac{M_{fy}}{M_{py}} \leq 1.0 \tag{5}$$

Equation (4) represents the interaction between the axial force and the uniaxial major-axis bending moment and Equation (5) represents the interaction between the axial force and the uniaxial minor-axis bending. These equations are derived from the lower bound theorem. The lower bound theorem specifies that the internal forces must be in equilibrium with the applied loads. Therefore, the plastic stresses distribution in the section may be chosen arbitrarily if it satisfies the static equilibrium requirements. The standard uses a stress distribution in which the axial stress is distributed to a portion of the web and the bending stress is distributed to the flanges.

The combined shear and moment interaction for a transversely stiffened web member is covered in the standard. For class 1 and 2 members, the combined plastic bending and shear resistance verification is done with the following interaction formula:

$$0.727\frac{M_f}{M_r} + 0.455\frac{V_f}{V_r} \leq 1 \tag{6}$$

where M_f and V_f are, respectively, the factored moment and shear loads applied. The resisting moment M_r, in the context of this work focusing on the plastic resistance, is the plastic bending moment M_p and does not account for any member or local instabilities. V_r is the shear resistance of the cross-section. The plastic shear resistance is defined in the code as:

$$V_r = 0.8\varphi A_w F_s \tag{7}$$

where A_w represents the shear area of the member and F_s the ultimate shear stress. The shear area considered varies according to the steel cross-section fabrication method. The shear areas considered for hot-rolled shapes and welded shapes are shown in Figure 3.

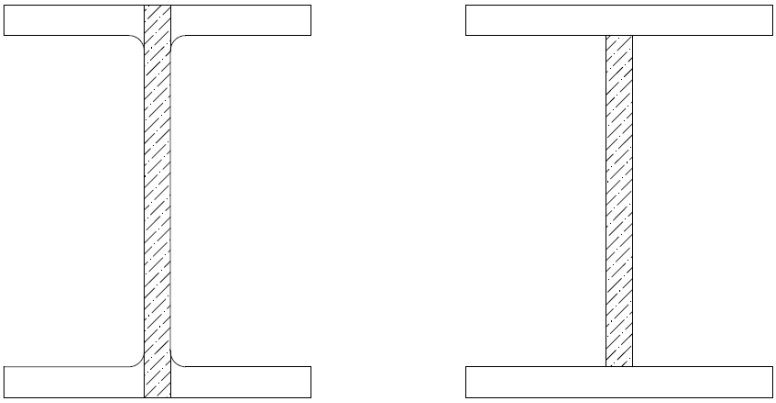

Figure 3 – Shear area for a) Hot-rolled sections b) Welded sections

According to the von Mises criterion, the shear yield stress for a ductile material is defined as:

$$\tau_y = \frac{f_y}{\sqrt{3}} = 0.577\, f_y \tag{8}$$

where τ_y is the shear yield stress and f_y the tensile yield strength of the material. The CSA S16 standard considers the beneficial effect of strain hardening on the shear yield stress. For compact sections, under the assumption that no local instabilities will occur, the shear yield limit defined in the standard is defined as:

$$F_s = \tau_y = 0.66\, f_y \tag{9}$$

No provisions for other loading interaction are provided within the CSA S16. For such loadings, the results validation will be based on analytical and numerical simulations.

1.1.2 – Eurocode 3

For doubly-symmetric I-beam class 1 and 2 sections, the plastic interaction set of equations for axial and bending forces is shown in equation (10).

$$\begin{gathered} M_{N,y,Rd} = M_{pl,y,Rd}\frac{(1-n)}{(1-0.5a)} \leq M_{pl,y,Rd} \\ n = \frac{N_{Ed}}{N_{pl,Rd}} \\ a = \frac{A-2bt_f}{A} \leq 0.5 \\ M_{N,z,Rd} = M_{pl,z,Rd}\; for\; n \leq a \\ M_{N,z,Rd} = M_{pl,z,Rd}\left[1-\left(\frac{n-a}{1-a}\right)^2\right]\; for\; n > a \end{gathered} \tag{10}$$

where $M_{N,y,Rd}$ is the reduced major-axis bending resistance, $M_{pl,y,Rd}$ the major-axis plastic bending moment resistance, $M_{N,z,Rd}$ the reduced minor-axis bending resistance, $M_{pl,z,Rd}$ the minor-axis bending resistance, N_{Ed} the applied axial load, $N_{pl,Rd}$ the plastic axial resistance, b the flange width and t_f the I-beam flange thickness.

The plastic interaction equation for axial and biaxal bending forces is shown in equation (11).

$$\left[\frac{M_{y,Ed}}{M_{N,y,Rd}}\right]^{\alpha} + \left[\frac{M_{z,Ed}}{M_{N,z,Rd}}\right]^{\beta} \leq 1 \qquad \alpha = 2 \qquad \beta = 5n \geq 1 \tag{11}$$

Eurocode 3 also provides a set of equations to consider the interaction between major-axis bending and vertical shear. For doubly-symmetric I-shapes, the major-axis bending resistance is reduced following the equation below:

$$M_{y,V,Rd} = \frac{\left(W_{pl,y} - \frac{\rho A_w{}^2}{4t_w}\right) f_y}{\gamma_{mo}} \leq M_{pl,y,Rd} \qquad M_{pl,y,Rd} = \frac{W_{pl,y} f_y}{\gamma_{mo}} \tag{12}$$

where $M_{y,V,Rd}$ is the reduced plastic bending moment resistance, $M_{y,c,Rd}$ the plastic bending moment resistance, $W_{pl,y}$ the plastic section modulus, A_w the shear area of the member, t_w the web thickness, f_y the tensile yield strength of the material. The reduction factor, in the context of this study, will be defined as $\gamma_{mo}=1$.

The principle of this formula is to artificially remove portions of the web under shear loads to the plastic modulus of the section $W_{pl,y}$. Therefore, most of the bending resistance is provided by the flanges of the section. The factor ρ is calculated only when the vertical shear force is greater than half the plastic shear capacity of the cross-section. Therefore, no interaction between bending and shear force is considered and the cross-section has full bending resistance. It will be seen further that the interaction does occur before reaching that threshold.

$$\rho = \left(\frac{2V_{Ed}}{V_{pl,Rd}} - 1\right)^2 \tag{13}$$

where ρ is the reduction factor used to determine the reduced bending resistance of members under bending and shear loads, V_{Ed} is the shear factored load and $V_{pl,Rd}$ the plastic shear resistance. Contrarily to the Canadian S16 standard, the Eurocode 3 plastic shear resistance does not consider strain hardening and is given by:

$$V_{pl,Rd} = \frac{A_v(\frac{f_y}{\sqrt{3}})}{\gamma_{mo}} \tag{14}$$

where A_v is the shear area, similarly to A_w in the Canadian standard CSA S16.

The shear area considered in the calculation of the shear plastic capacity of a cross-section has a non-negligible influence on the results. For hot-rolled cross-sections, the Eurocode 3 considers the shear area showed in Figure 4, where the fillets and portions of the flanges are considered in A_v. For welded sections, only the web area is considered, similarly to Figure 3 b).

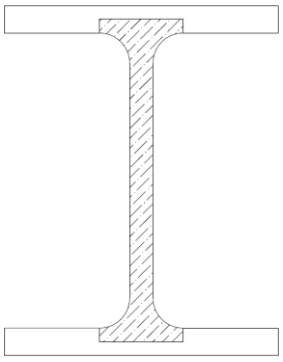

Figure 4 – Shear area considered in Eurocode 3

No provisions for singly-symmetric cross-sections are provided within the Eurocode. For such sections, the results validation will be based on analytical and numerical simulations.

1.2 – Available numerical tools

Various standards such as the Canadian Standards (CSA S16) and Eurocode 3 suggest interaction formulas to determine the plastic resistance of cross-sections, but these equations are specific to a limited number of geometries and loading cases. No interaction formula

exists to consider arbitrary internal forces combinations and geometries. Therefore, numerical methods will be explored to overcome such limitations.

The Finite Element Method is the most general and precise numerical approach. The F.E.M. method and applications are well described and documented in many books and scientific articles, such as (Bathe, 2014). F.E.M. modeling allows for complex geometries, geometric and material non-linear calculations and an extensive list of available F.E.M. software. Within F.E.M. modeling, a cross-section plastic analysis requires to model not only the section, but also the beam in 3D. Therefore, the modeling process and the analysis of finite elements are complicated and only an experienced user can provide precise and reliable results.

Another method to calculate the plastic capacity of cross-sections is the P.I.F. (Partial Internal Forces). The P.I.F. has been developed and explained in (Kindmann, 2011). The approach is a quasi-analytical method that distribute the normal and shear stresses over the constituting plates of the cross-section. The elastic stress distributions, for each different cross-section geometries must be known to determine the corresponding internal forces applied to each constituting plate. The method handles axial force, bi-axial moments, bi-axial shear, torsion and warping bi-moment. The P.I.F. method, in the reference cited above, has only been detailed for cross-sections with 3 plates, oriented perpendicularly. The P.I.F. method only allows for thin-walled cross-section using a single type of material. The method is based on a perfectly plastic material law and the effect of radiuses has not been considered. The P.I.F. method considers all the required internal forces but is very specific to steel cross-sections and is limited in terms of applicability.

In a previous thesis (Epiney, 2015), the R_{RESIST} program, based on the fiber decomposition approach, has been implemented. The general idea of the method is to decompose the cross-section area into fibers, thus creating integration points across the cross-section surface. The normal deformations and bending curvatures are increased proportionally to determine the strain distributions over the cross-section. With the calculated normal strains and the material stress-strain curve, the normal stresses, for each fiber, can be calculated and numerically integrated over the cross-section to determine the internal forces. Although the method is accurate for doubly-symmetric cross-sections, restrictions regarding other possible cross-

section shapes render this program not general enough for arbitrary cross-section shapes. The fiber decomposition allows for various materials within the cross-section. Also, the program does not support the shear internal forces.

The alternative is to use the fiber decomposition method coupled with the tangent stiffness method (Santathadaporn & Chen, 1971). This method uses a non-linear Newton-Raphson algorithm to provide an accurate yet simple way of calculating the cross-section plastic capacity for any cross-section shapes under axial load and bi-axial bending. In addition to the advantage of defining various shape geometries, the section may be composed of multiple materials. Each fiber is linked to a material stress-strain curve, allowing for composite section analysis and complex material behavior. Further details will be given in the following sections.

1.3 – R_{RESIST} program description

The *RESIST* program calculates the plastic capacity of doubly-symmetric I-section, singly symmetric I-section and HSS cross-sections. In the program, following the Euler-Bernoulli theory, plane sections remain plane. Therefore, for the various loading conditions, the program increments the cross-section plane of deformations. From the plane and the geometrical properties of the cross-section, the strains at key locations are calculated. From the strains, the resulting stresses of each fiber are then computed and integrated until achieving convergence at each increment. The strain distribution in each fiber is determined by the purely normal deformation, the major-axis and the minor-axis curvature. The shear stresses are not supported by the tool.

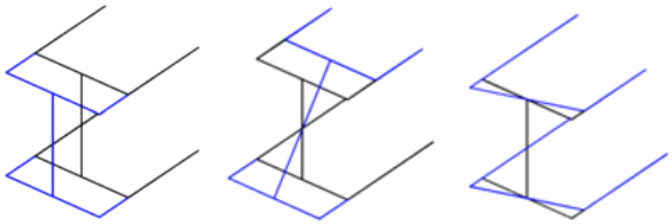

Figure 5 – a) Normal deformation b) Major-axis curvature c) Minor-axis curvature

Each fiber is related to a stress-strain relationship corresponding to the material defined. The deformations of each fiber, taken at its center, are incremented until a given maximum

deformation limit is obtained. This maximum limit can be set arbitrarily. To obtain full plasticity, 10 times the elastic deformation limit is often sufficient. With this limit, the cross-section is far into the elasto-plastic phase or fully yielded. The program supports the interaction between axial and bi-axial bending efforts. It also supports multiple material laws and consider the filet radiuses. Although the program provides accurate results for doubly-symmetric sections, convergence problems and inaccuracies were found when calculating the plastic capacity of singly-symmetric I-sections.

1.3.1 – R_{RESIST} program limitations

The program is limited in its usage regarding the geometry of the cross-sections to be analysed. Even though the mono-symmetric I-beam cross-section is included within the program options, the internal forces equilibrium is not respected. Initially, in the elastic stress zone, the curvatures of the cross-section rotate around the elastic neutral axis (center of gravity) as it coincides with the plastic neutral axis. Therefore, the strain distribution, in the elastic zone, is valid. As a result of the asymmetry, the spread of plasticity of the fibers across the section creates a loss in equilibrium of the internal stresses. In a simple case of major-axis bending, that phenomenon can be represented by the inequalities of the yielded areas above and below the elastic neutral axis. To keep the stresses in equilibrium, a shift of the plastic neutral axis should occur away from the geometrical center of gravity. The shift can either be along one or two axes of the cross-section. For uniaxial bending moment, the neutral axis will only shift in one axe. For biaxial bending, the neutral axis will shift in both axes. The shift of the plastic neutral axis was not handled in the R_{RESIST} program as the curvatures are always rotated around the elastic neutral axis. This leads to false results in the elasto-plastic range as a major-axis bending moment would create a resulting axial effort. Therefore, the tension and compression zone efforts, produced by the bending load, do not balance.

Tests have been conducted to determine the error related to the method compared to theorical results. Two major-axis bending moment cases have been considered to confirm the statements above: one test for a doubly-symmetric I-beam and one test for a singly-symmetric I-beam. Previous mesh density tests have already been conducted in (Epiney, 2015). Therefore, adequate meshing precision has been used. Each cross-section plates have been divided horizontally and vertically in 5 or 10 divisions. The number of horizontal and vertical

divisions are denoted respectively by the *m* and *n*. The doubly-symmetric section chosen is a W410x85 and the mono-symmetric section is a WRF1000x340. The yield limit (f_y) is defined at 350 MPa.

Table 1 - R_{RESIST} plastic capacity results for singly and doubly-symmetric I-Section

	Analytical M_{pl} [kN·m]	R_{RESIST} M_{pl} [kN·m]	Error [%]
Doubly-symmetric W410x85			
$\boldsymbol{m = n = 5}$	605.50	606.00	0.08
$\boldsymbol{m = n = 10}$	605.50	608.25	0.45
Mono-Symmetric WRF1000x340			
$\boldsymbol{m = n = 5}$	5583.20	6500.00	14.10
$\boldsymbol{m = n = 10}$	5583.20	(Diverged)	-

For the doubly-symmetric section, the results are in very good accordance with the analytical results. The slightly higher error, for the more refined meshing, may be caused by numerical errors as the number of operations is greater. Among the convergence problems, the plastic capacities obtained for the singly-symmetric I-beam are not satisfactory. An error of 14.1 % could produce major design errors in practice as the plastic capacity is not safe-sided.

From the results described above, the *R_{RESIST}* program is limited to doubly-symmetric cross-sections. Convergence problems and errors on the plastic capacity of mono-symmetric cross-sections limits the usability of *R_{RESIST}*.

1.4 – Description of the O.I.C. Concept

The previous section discussed the plastic resistance of a member cross-section. Although, the global resistance of a member is not limited to the cross-section plastic capacities. This section will present a new method to calculate the overall resistance of a member.

The O.I.C. (Overall Interaction Concept) is a design method that incorporates multiple advantages, in accuracy and consistency, compared to current methods prescribed in the standards. The O.I.C. is a concept where key design values can be determined with specific attention regarding the local instabilities and global instabilities of the cross-section and the member. The method relies on the resistance-instability concept, with various generalized

slenderness and buckling factors. The goals for the designing engineers are to provide a safe but economical design to their client. As of today, the engineers strictly base their designs on the various design codes applicable to their region. While all being close to each other, the codes have slightly different design philosophies and degree of explanations behind the equations provided. Every standard is based on the cross-section classification as an initial design step. The cross-section class is defined by the most detrimental plate classification, by means of *b / t* ratios, of the constituting plates of the cross-section. Some inconsistencies may be observed at the class 2 and class 3 border. Figure 6 illustrates the sudden gap of resistance at the class 2-3 border.

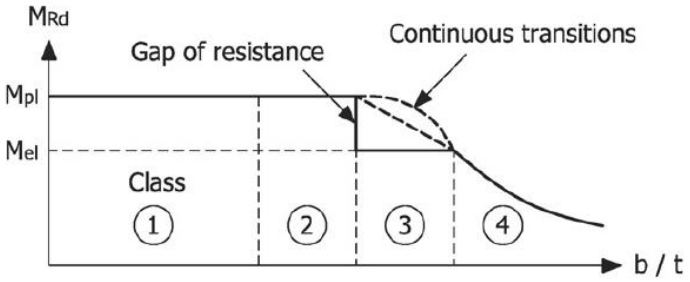

Figure 6 – Bending resistance gap at the class 2-3 limit

A major advantage of the O.I.C. method is to consider the cross-section as a whole, instead of assuming "ideal support conditions" for the cross-section constituting plates. There are indeed non-negligible interactions between the elements of a given cross-section. For example, the flanges stiffness of an I-section, which are considered as pinned-free elements, have an influence on the support conditions of the web, usually considered as pinned-pinned. By increasing the flanges thicknesses, the web supports tend to be close to clamped-clamped, modify the buckling behavior and lead to over-conservative results (Boissonnade et al., 2017).

While those standards are there to simplify the design of structures, some techniques used are cumbersome, such as the calculation of the effective properties of class 4 sections. The extensive number of calculations needed may discourage the use of high strength steel as most of the constituting plates of an element are slender.

The O.I.C. concept is an open and general methodology which removes the barrier of classes and performs the analysis and design according to any section shape and any grade or type of steel used. Figure 7 demonstrates the basic principles and application steps of the O.I.C. design method. The lambda factor λ_{rel} represents the slenderness of the element by considering the relation between the full plastic capacity of the member and the critical instability limit. The khi factor χ defines the relation between the plastic resistance and the element ultimate failure.

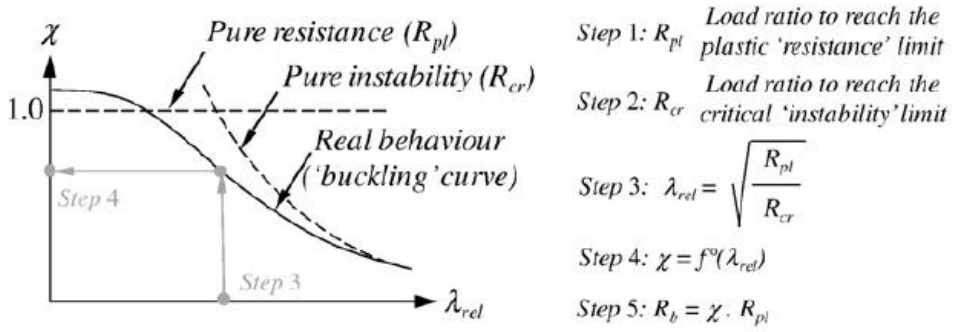

Figure 7 – O.I.C. basic principles

1.5 – Objectives and methodology

Even though steel doubly-symmetric I-beams are used the most in practice, a numerical tool is required to perform the plastic capacity analysis of arbitrary cross-sections. The O.I.C. is a general design approach; therefore, the numerical tools must be used for any section geometries. The first objective is to develop and validate a numerical tool to determine the plastic load multiplier of arbitrary steel cross-sections under axial and bi-axial loading. The second objective is to include, within the tool, the effects of shear forces, major-axis and minor-axis shear, on the plastic capacity of cross-sections. With the program validated for normal and shear loads, the study previously done by (Epiney, 2015) will be reviewed and completed. In summary, the objectives of this work are to (i) precisely calculate the plastic capacity of unsymmetrical cross-sections, (ii) consider the shear forces detrimental effects on the plastic capacity through the von Mises criterion and (iii) to consider the influence of shear for members in bending (transversal loading) and tension.

Chapter 2 – Plastic capacity of cross-sections

From the chapter above, it is known that the plastic capacity multiplier of cross-sections is a required parameter in the O.I.C. approach. This chapter will present and detail an approach to calculate the plastic capacity multiplier of cross-sections. The approach has been described in (Santathadaporn & Chen, 1971). Although, this approach only calculates the plastic capacity multiplier for cross-sections under axial and bi-axial loading. Using this approach, a numerical program R_{pl} will be developed. With the objective to include the shear loads effects on the plastic capacity of cross-sections, a review of the shear theory will be presented. A method to implement the shear effects into the numerical tool will be proposed. In summary, this chapter will describe the approach used to develop the numerical tool R_{pl} and the approach used to implement the effects of shear loads on the plastic capacity of cross-section into R_{pl}.

2.1 – Cross-section tangent stiffness method

The cross-section tangent stiffness method has been described by (Santathadaporn & Chen, 1971). The method relies on the tangent stiffness of the cross-section and the Newton-Raphson convergence algorithm. The tangent stiffness matrix is built by numerically integrating the cross-section stresses during the iteration process. The cross-section is divided into fibers and the stresses are calculated at the center of each fiber. While performing a non-linear analysis, the external loads are applied gradually. To apply the loads gradually, the total external loading is divided into load steps. Therefore, the internal forces, contained within the cross-section in the iteration process, will also increase gradually.

The general idea of this method is to build, for each iteration, the tangent stiffness matrix of the cross-section. The tangent stiffness matrix is used in conjunction with the external loads of the given load step to iterate toward an equilibrium of the cross-section deformations and internal stresses. Within a load step, the tangent stiffness is calculated to predict the incremental strains of the fibers in relation to the out-of-balance force vector. The generalized strains are the axial deformations and the major-axis and minor-axis bending curvatures. To reach the next load step, the iteration procedure must have converged to an equilibrium for the current state of loading. Essentially, this method has been developed to build interaction diagrams for steel and concrete sections under axial load and biaxial bending.

2.1.1 – Meshing and section properties

The first step of the process is to discretize the cross-section into multiple fibers. Each discretized fiber may have different geometrical and material properties. Although the method is flexible in terms of the material constituting the cross-section, the most general case is a homogenous cross-section. Each fiber is assigned an integration point at its geometrical center as depicted by Figure 8. Figure 8 also depicts the axis system convention. The strains of each fiber will be evaluated at the integration points. From the strains, the stresses, for each fiber, will be calculated. From the calculated stresses of each fiber, the global internal forces will be integrated. Special attention must be addressed to the cross-section discretization. For the results to be precise, the cross-section must be divided in an adequate number of fibers. This has a direct consequence on the time of calculation of the plastic capacity of the cross-section, mostly if the full interaction diagrams are required. The influence of the meshing density on the precision of the results will be studied in the next chapter.

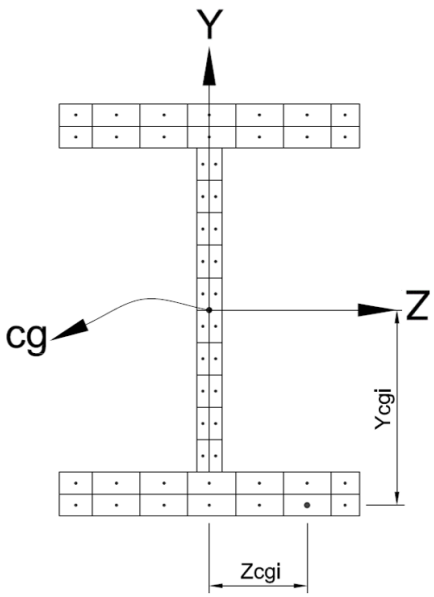

Figure 8 – Cross-section meshing. integration points and reference axes convention

As the cross-section is divided into fibers, the method does not require any pre-defined knowledge of the general cross-section geometry to calculate the axial stresses distribution. The axial strains and stresses distribution only require the geometrical properties of each

individual fibers. Contrarily, the shear stress distribution calculations require the geometrical properties of the whole cross-section.

Using the integration points, the global cross-section properties are numerically integrated. The numerical integration considers the effect of each individual fiber on various key properties, such as the total area and the moments of inertia about the Y-axis and Z-axis of the cross-section.

The cross-section total area *A* is defined by:

$$A = \sum_{i=1}^{n} A_i \tag{15}$$

where *n* is the total number of fibers comprised within the cross-section and A_i the area of each fiber.

The moment of inertia about the Y-axis and Z-axis are calculated using the Parallel Axis Theorem (Craig JR., 2011). The major-axis and minor-axis moments of inertia are defined by the inertia of each individual fibers plus the product of the fiber area and the squared distance of the fiber to the centroid.

$$I_{zz} = \sum_{i=1}^{n} I_i + {y_i}^2 A_i \tag{16}$$

$$I_{yy} = \sum_{i=1}^{n} I_i + {z_i}^2 A_i \tag{17}$$

where I_{zz} and I_{yy} are respectively the major-axis and minor-axis moments of inertia, I_i the fiber individual moment of inertia and y_i and z_i the distances of the fiber to a given reference point.

Although the method has been developed to be general, no reference regarding the consideration of shear stresses were found in the literature. The shear stresses have been added considering an understanding of the cross-section behavior under such loads. Further details will be provided in later sections.

2.1.2 – Numerical integration of the cross-section filets

Basically, two fabrication processes for steel members can be found in practice, namely the hot-rolled and welded fabrication processes. For welded cross-sections, the weld area is small and can be neglected. Neglecting the weld and considering only the plates in the plastic analysis does not produce significant errors.

However, the radiuses of filets of hot-rolled cross-sections do affect positively the plastic resistance. The radiuses have been modeled using the fiber method by dividing horizontally and vertically their area. Again, the numerical integration of the fibers is performed by considering only 1 integration point for each fiber. Although it follows the same resolution methodology, the radiuses were not considered in the description of the tangent stiffness method in (Santathadaporn & Chen, 1971).

2.1.3 – Generalized normal stresses and strains

Within the elastic range of a fiber, Hooke's law dictates the relation between the axial stresses and the axial strains by the modulus of elasticity *E*.

$$\sigma_{xi} = E\ \varepsilon_{xi} \tag{18}$$

where σ_{xi} and ε_{xi} are respectively the axial stress and strain of a fiber.

The forces that produce axial stresses over the cross-section plane are the axial load, the biaxial bending moments and the warping bi-moment. As mentioned in the previous chapter, it is assumed that plane sections remain plane. These forces may be numerically integrated using the equations below.

$$N = \sum_{i=1}^{n} \sigma_{xi}\, A_i \tag{19}$$

$$M_y = \sum_{i=1}^{n} \sigma_{xi}\, z_i\, A_i \tag{20}$$

$$M_z = \sum_{i=1}^{n} \sigma_{xi}\, y_i\, A_i \tag{21}$$

$$B_w = \sum_{i=1}^{n} \sigma_{xi}\, \omega_i\, A_i \tag{22}$$

where N is the internal axial force, M_y and M_z are respectively the internal bending moments around the Y-axis and Z-axis, B_w the warping bi-moment, ω_i the warping function and n the number of fibers composing the cross-section. More information on how to calculate the warping function may be found in (Kindmann, 2011). Although the warping bi-moment has been programmed within R_{pl}, no further tests validation tests have been performed on that internal force. Also, a warping bi-moment invalidates the hypothesis that plane sections remain plane.

To determine the total axial stress σ_{xi} of each fiber, the total axial deformation ε_{xi} must be known.

$$\varepsilon_{xi} = \varepsilon_{xi-1} + \Delta\varepsilon_{xi} \tag{23}$$

where ε_{xi-1} is the cumulated axial strain and $\Delta\varepsilon_{xi}$ is the calculated iterative incremental axial strain of the fiber. The incremental deformation of each fiber is related to the generalized strains on the cross-sectional level as given by equation (24).

$$\Delta\varepsilon_{xi} = \Delta\varepsilon_o + \Delta\varphi_y * z_i + \Delta\varphi_z * y_i \tag{24}$$

where $\Delta\varepsilon_o$ is the global incremental axial strain and $\Delta\varphi_y$ and $\Delta\varphi_z$ are the incremental curvature of the Y-axis and Z-axis respectively. A curvature defines a plane of axial deformation of a given cross-section as shown in Figure 9. Thus, the axial deformation of any given fiber of the cross-section, caused by a bending moment M, is calculated by the linear relationship of the curvature φ and the geometrical location of the fiber.

When a cross-section is under pure bending, the resultant of the axial stresses for all fibers must be equal to zero. For a fully elastic cross-section, the equilibrium between compressive and tension stresses is calculated according to the elastic neutral axis (E.N.A.). The E.N.A.

is an axis where the strains and stresses are zero. For a cross-section that is fully elastic and isotropic, the E.N.A. is located at the center of gravity of the cross-section.

For a partially yielded cross-section under pure bending, the equilibrium of the axial stresses is determined by the plastic neutral axis (P.N.A.). For isotropic and symmetrical cross-sections, the P.N.A. and the E.N.A. share the same position and divides the cross-section into two equal areas. For cross-sections that are either made of multiple materials or unsymmetrical, at the onset of yield, the P.N.A. position does not correspond to the E.N.A. position. During the elastoplastic state, where the cross-section is partially elastic and partially yielded, the P.N.A. shifts gradually toward its fully plastic position. The integration of the compressive and tension axial stresses, if calculated according to the E.N.A., would not fulfill the zero axial stress resultant requirement. Therefore, the P.N.A. divides the cross-section into two equal axial forces (tension and compression) resultants.

For cases where the cross-section is under a combination of axial and bending loads, the axial force resultant over the cross-section must be equal to the axial external load.

When all the fibers are in their elastic domain, the 3 components of equation (24) are uncoupled and have no interaction. Thus, the axial deformations caused by the axial load and the bending moments can be calculated separately and the stress resultants are calculated according to the E.N.A. As the cross-section progressively yields, the P.N.A. position becomes unknown, and those components become coupled. The problem must be resolved using non-linear iteration techniques to find the deformations at which the internal loads are in equilibrium.

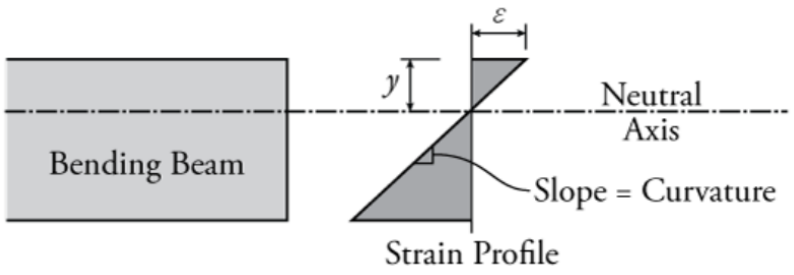

Figure 9 – Axial deformation of a cross-section caused by the major-axis curvature (https://learnaboutstructures.com/Bernoulli-Euler-Beam-Theory)

The stresses in each fiber are determined according to the material stress-strain curve and the calculated strains at every iteration according to equation (23) and (24).

$$\sigma_{xi} = f(\varepsilon + \Delta\varepsilon_i) \tag{25}$$

where σ_{xi} is the axial stress of a fiber calculated at the integration point and $f(\varepsilon + \Delta\varepsilon_i)$ the piecewise stress-strain function which gives the axial stress value of a fiber for a given value of strain.

2.1.4 – Material stress-strain curves

The stress-strain curve of a material represents the evolution of the stresses as the material deforms. Each type of material behaves differently, requiring various stress-strain curves to represent each material accurately. In the context of this study, material laws specifically for steel will be described.

In general, the plastic capacity of steel cross-sections is calculated using a perfectly elasto-plastic material law without strain hardening as depicted in Figure 10. Therefore, the stresses cannot go beyond the yield stress f_y. Any beneficial strain hardening effects on the plastic capacity are thus neglected.

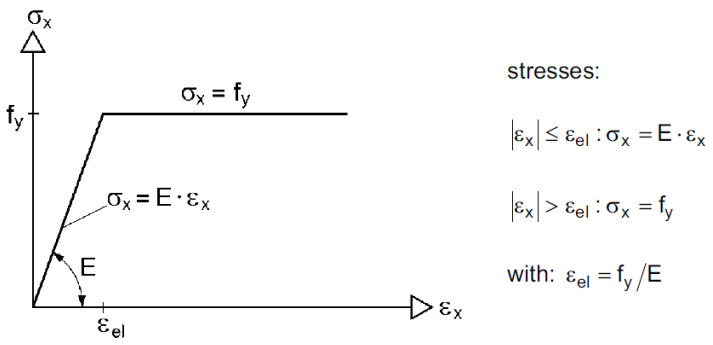

Figure 10 – Perfectly plastic stress-strain curve (Kindmann, 2011)

Even though calculations usually omit the strain hardening effects on the plastic capacity of cross-sections, strain hardening can be found in mild steel and may have a major effect on the plastic resistance of the cross-section. Material laws considering this effect will be programmed.

The strain hardening effect may be approximated as a linear increase of the stresses beyond the yield stress f_y as depicted in Figure 11. As the stresses go beyond the yield stress f_y, the strain hardening effect is considered using an appropriate Young modulus E_p for the yielded the fibers.

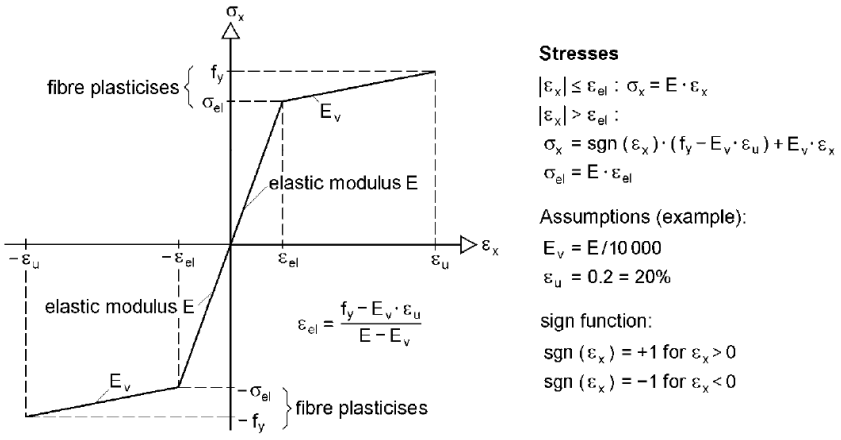

Figure 11 – Stress-Strain curve with linear strain hardening (Kindmann, 2011)

Also, such type of material stress-strain curve may avoid numerical instabilities. The cross-section tangent stiffness method uses the tangent Young modulus E_t to calculate the tangent stiffness matrix. The tangent Young modulus E_t is extracted from the material stress-strain curve. The tangent Young modulus E_t is the slope of the stress-strain curve at a given

deformation. For the material law depicted in Figure 10, the material Young modulus beyond f_y is null. This translates to fibers with no rigidities. At high deformations, this may cause an overall loss in rigidity of the cross-section and the tangent stiffness matrix may become unstable and the solution will diverge. To address this issue, a material model, such as Figure 11, with linear strain hardening can be used to mitigate those numerical issues while maintaining f_y as the yield stress in each fiber. If this stress-strain curve is only used to avoid numerical issues, the plastic Young modulus E_p may be defined as approximately 0.1% of the elastic Young modulus of the material. The slope being very shallow, the stress increase compared to f_y is negligible.

If more precision is needed when considering the strain hardening, refined stress-strain laws, such as Ramberg-Osgood, can be used. The goal is to represent as best as possible the behavior of the corresponding type of steel used in the calculations.

2.1.5 – Non-linear resolution techniques

The following section briefly explains the non-linear control method used. Contrarily to a static analysis, where the full loading is applied all at once, a non-linear analysis uses the principle of load steps. A load step is basically a fraction of the total external loading applied to the structure. Within the load step, the out-of-balance forces are computed using iterations until convergence of the external and internal loads is obtained, as shown in Figure 12.

The Full Newton-Raphson (F.N.R.) iterative technique has been implemented in the context of this work. The F.N.R. computes the tangent stiffness matrix every iteration in comparison to the Modified Newton-Raphson (M.N.R.) technique, where the stiffness matrix is only computed at every load step. As the tangent stiffness matrix is calculated at every iteration, the F.N.R. usually converges in less iterations than the M.N.R. Although the number of iterations required in the F.N.R. may be less than the M.N.R., the mathematical operations on the stiffness matrix may render the iterations process slower. The stiffness matrix size is a key variable on the time consumption.

The reasoning behind the decision to use the F.N.R. is that (i) the dimension of the stiffness matrix is small and (ii) it converges in less iterations. The dimension of the stiffness matrix being small, resolution time should not be an issue. Numerical tests will be performed to confirm the performance of the F.N.R. for this application.

The M.N.R. algorithm could eventually be implemented for this application but the F.N.R. does not require much more computing time, thus limiting the beneficial effects of the M.N.R. technique. Figure 12 shows the basic principle of the F.N.R. procedure, which is to recalculate the stiffness tangent matrix at every iteration within a load step to predict the estimated incremental displacements at every iteration. How rapidly convergence is achieved within a load step is governed by the scaling of the variation of the load and the non-linearity of the problem to be solved.

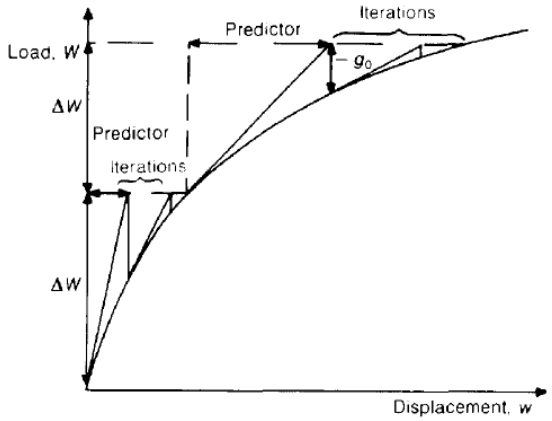

Figure 12 – Full Newton-Raphson iterative procedure (Crisfield, 1991)

Of all the various non-linear control methods, such as the displacement or arc-length method, the load control formulation is the most straightforward non-linear resolution procedure to implement and, also, the most limited convergence wise. The load control formulation may only reach the first limit point. A limit point is a point where the behavior of the problem may change as a result of the solution becoming unstable. The general principle of this method is to divide the total external applied load into multiple load steps. Using the F.N.R. procedure, convergence is obtained using iterations within a load step. Inside the load step, the load factor parameter λ, does not vary. Convergence within the iterations signifies a stable solution and the analysis may proceed to the next load step.

The downfall of the load control method comes from the inability to converge past limit points. This behavior is explained by the inability to reduce the load after a limit point is reached. For the plastic capacity of cross-sections, this method is sufficient as only the first limit point is required and thus does not require the additional complexity of other methods.

2.1.6 – Cross-section tangent stiffness matrix

As described in the previous section, the F.N.R. procedure is separated into two main blocks; the load step increments and the iterations within the load steps. Within the iteration block, the tangent stiffness matrix is used in the non-linear iteration scheme as a predictor of the cross-section deformations. The tangent stiffness matrix provides the relationship between the incremental strains, for a given iteration, and the unbalanced force vector. The relationship is as follows:

$$\{R\} = [K_{cs}]\{\Delta\varepsilon\} \tag{26}$$

where $\{R\}$ is the unbalanced force vector, $[K_{cs}]$ the tangent stiffness matrix and $\{\Delta\varepsilon\}$ the vector of incremental strains. The incremental strain vector $\{\Delta\varepsilon\}$ represents the incremental strains $\Delta\varepsilon_o$, $\Delta\varphi_y$ and $\Delta\varphi_z$. To determine the incremental strains, the stiffness matrix is inverted and equation (27) is used.

$$\{\Delta\varepsilon\} = [K_{cs}]^{-1}\{R\} \tag{27}$$

where $[K_{cs}]^{-1}$ is the inverted tangent stiffness matrix of the cross-section.

The fiber's tangent Young modulus is the key parameter related to the stiffness of the cross-section and will be used to build the tangent stiffness matrix. The tangent Young modulus E_t is evaluated for each individual fiber as the planes of deformation will create a variation of deformations intensity over the cross-section, thus a variation of the material properties. The cross-section tangent stiffness matrix is calculated as follows:

$$[K_{cs}] = \begin{bmatrix} \sum_{i=1}^{n} E_{t\_i}\, A_i & \sum_{i=1}^{n} E_{t\_i}\, z_i A_i & \sum_{i=1}^{n} E_{t\_i}\, y_i A_i \\ \sum_{i=1}^{n} E_{t\_i}\, z_i A_i & \sum_{i=1}^{n} E_{t\_i}\, {z_i}^2 A_i & \sum_{i=1}^{n} E_{t\_i}\, y_i z_i A_i \\ \sum_{i=1}^{n} E_{t\_i}\, y_i A_i & \sum_{i=1}^{n} E_{t\_i}\, y_i z_i A_i & \sum_{i=1}^{n} E_{t\_i}\, {y_i}^2 A_i \end{bmatrix} \tag{28}$$

With the equations shown in this section, the general analysis procedure will be detailed in the next section.

2.1.7 – General procedure of the tangent stiffness method

As defined previously, the non-linearity of the problem and the coupling of the variables require a linearization of the system of equations. Linear variations of the stresses and

deformations are used to do such linearization. The material behavior of the fibers is determined by linear segments dependant of the stresses and strains where the slopes are the tangent modulus E_t. Using linearized material laws, the yielded tangent modulus E_t of the fibers may be determined for any state of axial strain calculated with equation (23).

The F.N.R. technique is used to obtain convergence of the internal forces to the external forces. The system of equations is defined by 3 unknowns governing the problem. The variables have been described in (24) and correspond to $\Delta\varepsilon_o$, $\Delta\varphi_y$ and $\Delta\varphi_z$. The linearization of the problem is performed by defining the stress-strain relationship in terms of variations of theses unknowns. The incremental strains can be written in vector form as such:

$$\{\Delta\varepsilon\} = \begin{bmatrix}\Delta\varepsilon_o & \Delta\varphi_y & \Delta\varphi_z\end{bmatrix}^T \tag{29}$$

where $\Delta\varepsilon$ is the vector of incremental strains containing the variation of the axial strain $\Delta\varepsilon_o$ and the bending curvatures $\Delta\varphi_y$ and $\Delta\varphi_z$. These incremental strain values are used in conjunction with equation (24) to determine the incremental axial deformation of each fiber.

From the incremental axial strains, the vector of total strains is calculated as follows.

$$\{\varepsilon\} = \{\varepsilon\} + \{\Delta\varepsilon\} \tag{30}$$

As defined by equation (27), the incremental strains are calculated using the tangent stiffness matrix and the out-of-balance force vector. The out-of-balance force vector is obtained by the relationship between the applied external forces and the internal forces carried by the cross-section. This vector is defined by the difference between the external and internal load vectors and is recalculated within the iteration procedures.

$$\{R\} = \{F_{ext}\} - \{F_{int}\} \tag{31}$$

where $\{R\}$ is the out-of-balance force vector commonly known as the residual vector, $\{F_{ext}\}$ is the external force vector and $\{F_{int}\}$ is the internal force vector. The iterative scheme is set to converge toward an equilibrium of the internal forces stored in the cross-section fibers and the external forces.

As mentioned above, the external loads are applied incrementally. The external force vector $\{F_{ext}\}$ corresponds the load applied to the cross-section for the current load step. The load

step increment corresponds to the additional fraction of the total external load λ that needs to be converged to.

$$\{F_{ext}\} = \lambda * \{F_{tot}\} \tag{32}$$

where $\{F_{ext}\}$is the external load applied to the cross-section at the current load step, λ the fraction of the total load at the current load step and $\{F_{tot}\}$ the total load to be applied on the cross-section. The external load vector $\{F_{ext}\}$ represents, in order, the external loads N, M_y and M_z.

The loads increase proportionally until the maximum load is reached, meaning they increase according to the same load ratio. The load path eventually reaches the failure surface such as shown in Figure 13. The failure surface delimits the maximal resistance capacity of the cross-section for combined loading.

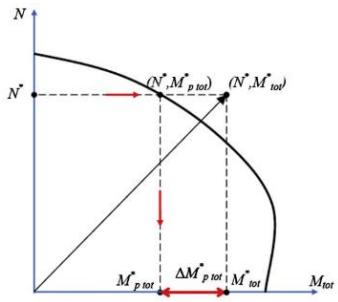

Figure 13 – Radial loading path to the failure envelope (Chiorean, 2013)

The internal force vector $\{F_{int}\}$ is calculated by integrating the stresses of each fiber. The stresses are calculated using the total axial deformation and the stress-strain curve of the fiber using the equation (25). In vector form, the numerically integrated internal forces, calculated using equations (19), (21) and (20), are denoted as such:

$$\{F_{int}\} = \begin{Bmatrix} N \\ M_y \\ M_z \end{Bmatrix} \tag{33}$$

Convergence of the iterations, for a given load step, is obtained when the residual vector converges toward zero, within a given tolerance. When convergence is achieved, the load step is incremented to reach higher levels of external loading. The plastic capacity of the cross-section is found when a stop criterion is triggered. The stop criterions are (i) when a

fiber reaches the maximum allowable strain or (ii) when the non-linear solution diverges. The maximum allowable strain is defined as an input in the program. The value of the maximum allowable strain must be chosen wisely so that (i) most of the cross-section yields and (ii) it should not lead to an over-estimation of the plastic capacity of the cross-section when considering a material with strain hardening. When either of the stop criterions are reached, the factor λ is the plastic capacity of the cross-section. It defines the load multiplier of the initial loading to which the cross-section can no longer sustain increased loads. The load increments are constant throughout the analysis. The divergence of the non-linear resolution technique may be caused by (i) the rigidity of the cross-section becomes null as all fibers have yielded (ii) a limit point has been reached. At that point, all the cells have yielded, or the remaining elastic cells produce near zero rigidity in comparison to the amount of load applied.

Reaching the full plasticity of the cross-section is very seldom achieved as it requires very large axial deformations at the extremities of the cross-section for the cells near the plastic neutral axis P.N.A. to yield. For example, the fibers closest to the P.N.A., under a major-axis moment, are likely to remain elastic. For a given curvature, their distance to the P.N.A. is very small and the added rigidity of those fibers to the global rigidity of the cross-section is consequently very small. Figure 14 presents the R_{pl} program flowchart.

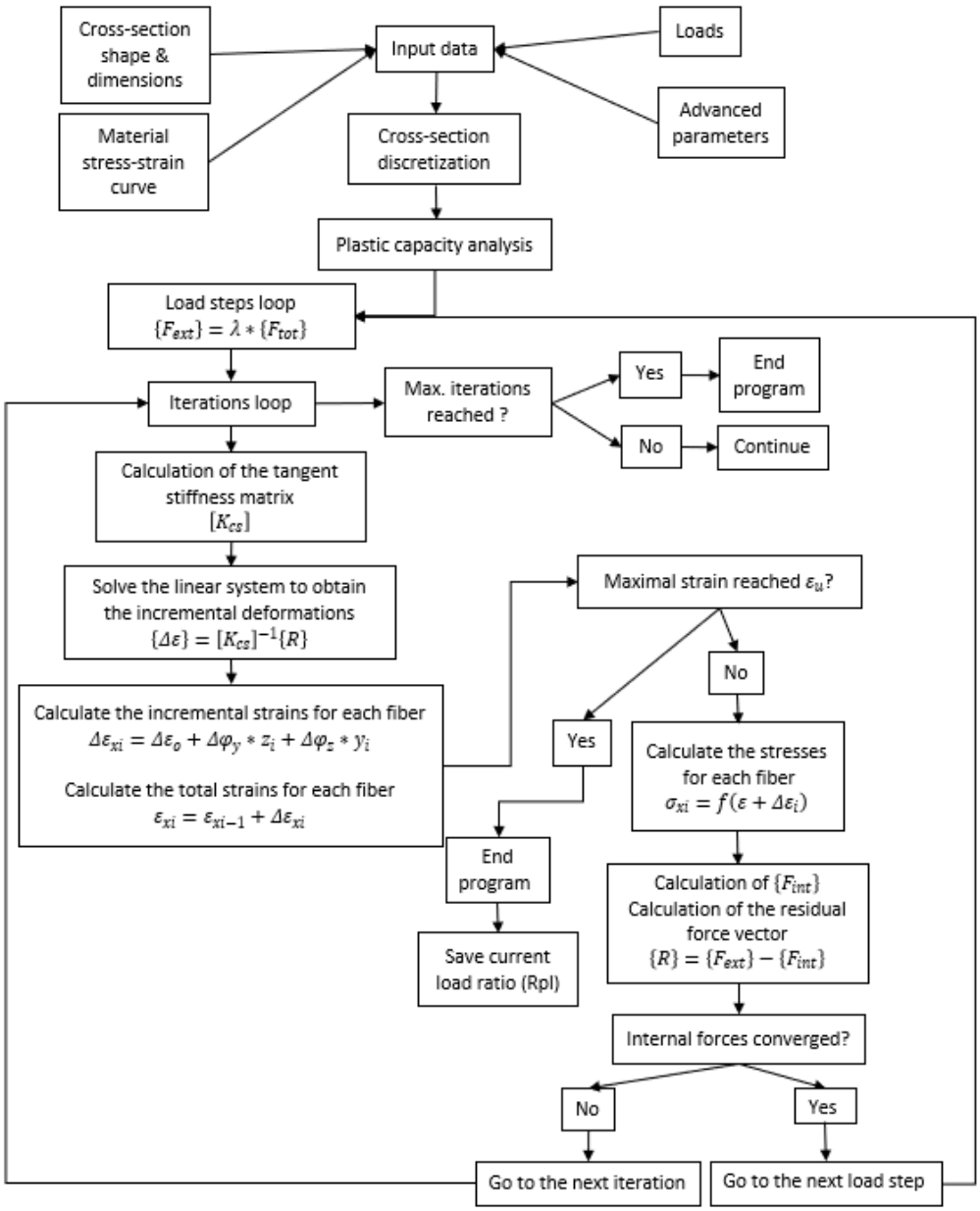

Figure 14 – R_{pl} program flowchart

2.2 – Shear stresses

Part of this project is to calculate the plastic capacity of cross-sections under shear loads. For cases where the loads are being applied within the span of the member, the interaction between shear and bending efforts is of prime importance. To implement the effect of shear on the plastic capacity of cross-sections, the following sections will review the theory of pure shear and shear stresses in beams. The implementation of those stresses within the program R_{pl} will also be explained.

2.2.1 – Shear stress in thin-walled beams

Unlike the case of pure bending, where the assumption that plane sections remain plane is valid, transverse shear stress distorts the section. Although it violates Bernoulli's hypothesis, the effects of the distortions on the axial behavior of the cross-section have negligible influence. Therefore, an assumption is made that the deformations caused by shear do not influence the axial stress distribution over the cross-section. Thus, the hypothesis that plane sections remain plane, for the predictions of axial stresses, is still valid. A shear stress is defined by a force acting tangentially over a surface as depicted in Figure 15 b).

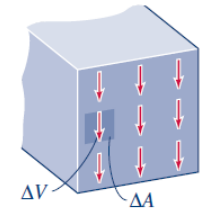

(*a*) The distribution of shear force on a sectioning plane.

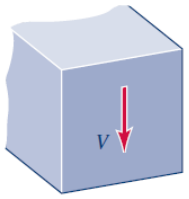

(*b*) The resultant shear force on the sectioning plane.

Figure 15 – a) Shear load over a surface b) Infinitesimal distribution the shear load over the surface (Craig JR., 2011)

The applied shear load may be distributed and represented by acting over infinitesimal portions of the surface. Therefore, the resultant shear force is calculated by integrating the shear stresses over the cross-section surface according to equation (34) and shown in Figure 15 b).

$$V = \int \tau \, dA = \sum_{i=1}^{n} \tau_i \, A_i \tag{34}$$

First, the case of pure shear over a deformable body and secondly, the shear stress theory for thin-walled beams will be examined. The application of shear stresses over a deformable body requires the satisfaction of equilibrium requirements. An infinitesimal volume within

the deformable body will be used to demonstrate the required force equilibrium as shown in Figure 16. To ensure the force equilibrium of the free-body diagram of the infinitesimal volume, equivalent forces in opposite directions must be found on all faces of the element.

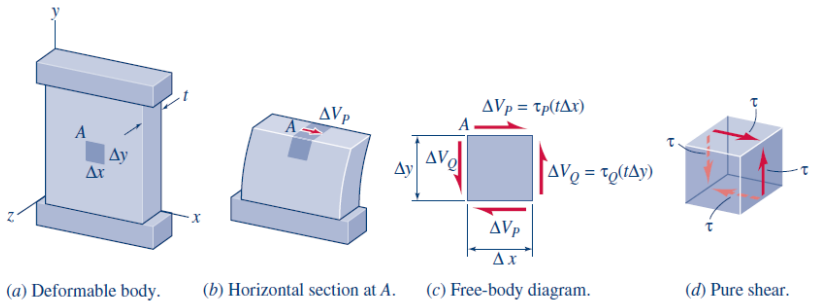

Figure 16 – Shear stress equilibrium over a deformable body (Craig JR., 2011)

While the shear stresses are in equilibrium over the faces of the infinitesimal element, the shear strain γ is defined as the angle of deformation of the element as shown in Figure 17. The concept of shear strain is important and will be the basis of implementing the shear stresses in the plastic capacity tool developed.

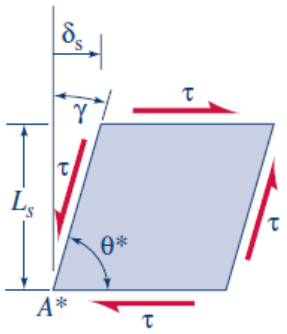

Figure 17 – Shear strain over an infinitesimal element (Craig JR., 2011)

While the basic equilibrium requirements and the shear strain have been explained, the shear stress distribution over a cross-section still need to be defined. To do so, a brief summary of the shear stress theory for beams will be presented below. The explanation will consider the simple case of a beam under major-axis bending where the moment *M(x)* varies along its length. The elastic normal stress distribution over the cross-section is known and must be in equilibrium such that the axial force resultant must be zero. At every level *y* of the cross-section, longitudinal shear stress must be present, as shown in Figure 18, to balance the axial

stresses. Knowing from the shear stress reciprocity that $\tau_{xy}=\tau_{yx}$, the vertical shear stress of an infinitesimal element of the cross-section must be of equal magnitude with the longitudinal shear stress. It is interesting to note that there is no longitudinal shear stress at both ends of the cross-section because the normal stresses equilibrium is met. This results in no vertical shear stress at those positions.

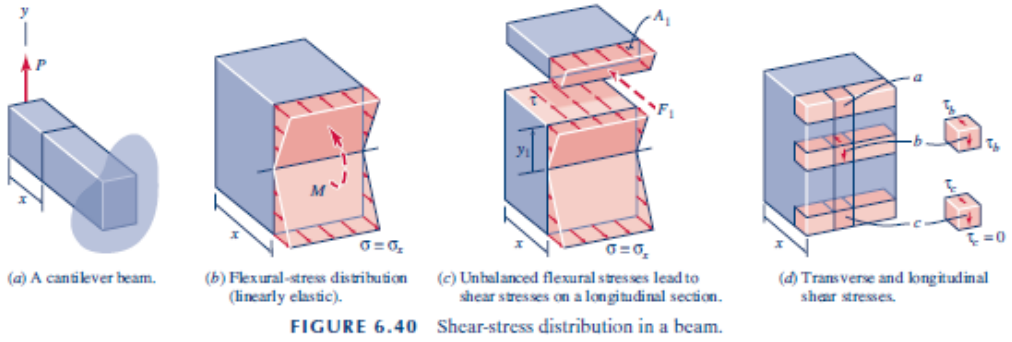

Figure 18 – Longitudinal shear stresses caused by unbalanced flexure stresses (Craig JR., 2011)

Next, the theory of shear flow will be explored. As the moment *M(x)* varies along the beam, the axial resultant must be zero at every position of the beam. Therefore, for a position *x* and *x+Δx*, a longitudinal shear stress must balance the axial force resultants if *M(x)* is not equal to *M(x+Δx)* and *V(x)>0* as shown in Figure 19.

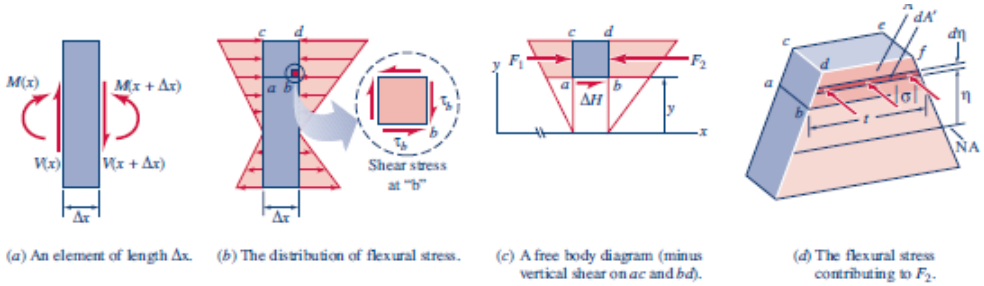

Figure 19 – Flexural and shear resultants of a beam under bending and shear loads (Craig JR., 2011)

The shear flow is the additional shear stress caused by the unequilibrated normal stresses divided by the infinitesimal segment *Δx*. Therefore, the shear flow is the shear force per unit length *Δx* and is given by:

$$q = \frac{V * Q}{I} \tag{35}$$

where q is the shear flow, V the shear load, Q the first moment of inertia and I the second moment of inertia. By dividing the shear force by the area where it acts (tributary area of the shear flow), this gives the average shear stress at a specific level of the cross-section.

$$\tau_{(x,y)} = \frac{V(x) * Q(x,y)}{I(x) * t(x,y)} \tag{36}$$

where $V(x)$ is the shear force at the position x along the beam, $Q(x,y)$ is the first moment of inertia with respect to the neutral axis of the area above y, $I(x)$ is the moment inertia of the cross-section at position x along the beam and t is the thickness of the cross-section at the level y.

The shear theory presented above is only valid for beams having a height about 2 times their width. The shapes used in the steel construction industry can be categorised as thin-walled sections, either open or closed. The shear flow can be evaluated for their constitutive plates at their centerlines. As the plates are generally thin, the shear stress calculated is an average shear stress over the thickness of the plate at a certain level y. Also, the shear stresses are considered as tangent to the plate centerline. For further mathematical developments, refer to (Craig JR., 2011).

2.2.2 – Shear stresses in R_{pl} 2.0

Shear stresses have been included in the plastic cross-section analysis in R_{pl} 2.0. The shear stresses considered are the major-axis and minor-axis shear. The shear stresses have been implemented for mono-symmetric and doubly-symmetric I-sections. Therefore, any fiber of the cross-section may be solicited by three stresses: an axial stress σ_x, a major-axis shear stress τ_{xz} and a minor-axis shear stress τ_{xy}. Shear stresses induced by torsion have not yet been implemented in the program. As the R_{pl} tool only considers equilibrium of the stresses at a specific cross-section, the use of the thin-walled beam shear flow and shear stress distributions can be implemented.

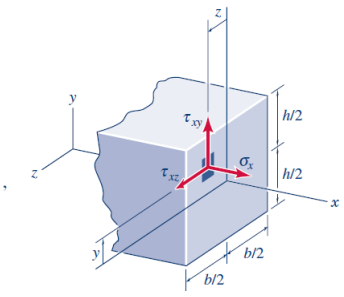

Figure 20 – Axial and shear stresses acting on the cross-section fibers (Craig JR., 2011)

The major-axis and minor-axis shear force resultants are calculated by numerically integrating the shear stresses acting on the fibers over the surface of the cross-section. The equilibrium equations for those internal forces are as follows:

$$V_z = \int \tau_{xz}\, dA = \sum_{i=1}^{n} \tau_{xz\_i}\, A_i \tag{37}$$

$$V_y = \int \tau_{xy}\, dA = \sum_{i=1}^{n} \tau_{xy\_i}\, A_i \tag{38}$$

In the elastic range, the shear stresses τ are related to the shear strains γ by the shear modulus G. Elastic shear stresses follow an analogous relationship to the normal stresses. The shear stresses are defined by:

$$\tau_i = G * \gamma_i \tag{39}$$

where τ_i is the shear stress along either the Z-axis or Y-axis of a fiber, G is the shear modulus and γ_i the shear strain of a fiber.

In the same logic as the axial stresses non-linear algorithm and procedures, the program applies increasing shear strains to each fiber according to the elastic shear stress distribution for the specific cross-section. Within a load step, the priority is given to the axial stress equilibrium. This procedure induces a limitation when consider axial and shear loads. In the plastic domain, the path to which a fiber deforms is important. Therefore, the procedure is only valid when a fiber is still within the ultimate plastic resistance curve envelope shown in Figure 13. A perfectly elastic-plastic material law must be used so that the post yield behavior of a fiber is not altered by the step-wise path of the axial and shear stresses algorithm. When

the internal and external axial loads are in equilibrium, the shear strains are increased to obtain the internal and external shear loads equilibrium.

As the shear loads increase, some of the fibers may attain their plastic state. Therefore, the stresses required to obtain the corresponding elastic shear stress distribution cannot be reached. Although the stresses are limited to the yield limit of the fibers, the shear strains can still be increased according to the elastic shear stress distribution. The fibers reach their maximum capacities, and the integration of the stresses does not equal the applied shear loads. As the plasticity spreads and the stresses reach a plateau, the shear strains need to be increased until equilibrium is reached between the internal and external forces. To obtain this equilibrium, a Newton-Raphson algorithm is used to increase the strains until the applied shear stress is fully carried. This process is done for all the external shear loads. At this point, every fiber of the cross-section carries the normal and shear strains required for cross-section equilibrium. The fibers plastic capacity is determined using the von Mises criterion.

Simplifications have been introduced to the major-axis shear stress distribution of such cross-sections. According to (Beyer, 2018), numerical simulations demonstrated that the plasticity does not spread into the filets. Therefore, they should not be included in the shear resistance area. Also, a choice has been made to neglect the flange accompanying horizontal shear stresses. Such a simplification has also been made in the P.I.F. method. According to (Craig JR., 2011), the web carries most of the shear force and therefore, the flange shear stresses may be neglected. In that case, the Newton-Raphson algorithm equilibrates the external and internal loads and the shear stress carried by the flanges are redistributed into the web. That could lead to safer results as yielding of the web may happen sooner as the stresses are slightly higher. The web area considered is the height of the web at the centerline of the flanges. A representation of the plastic shear stress distribution in the major-axis direction of an I-section is shown in Figure 21.

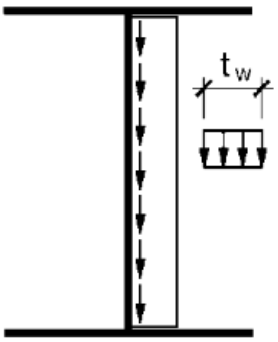

Figure 21 – Major-axis plastic shear stress distribution (Kindmann, 2011)

The minor-axis shear stress distribution is straight forward as the shear area considered is the area of both flanges. For doubly-symmetric cross-section, the shear load is separated in 2 equivalent concentrated loads acting on the top and bottom flange. For mono-symmetric cross-sections, an assumption is made that the total shear load is distributed as a ratio of the areas of both flanges. A representation of the plastic shear stress distribution in the minor-axis direction of an I-section is shown in Figure 22.

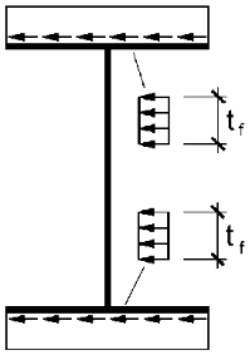

Figure 22– Minor-axis plastic shear stress distribution (Kindmann, 2011)

This section described how the shear efforts were transferred into the cross-section fibers. With axial and shear stresses within the fibers, a plasticity criterion must be used to determine the equivalent yield stress of the fibers. The von Mises yield criterion will be described in the next section.

2.2.3 – von Mises yield criterion

The fibers equivalent yield stress is calculated using the von Mises criterion. As the strains increase, the stresses are calculated according to the material stress-strain curve of the

material. For shear, an elastic-perfectly plastic shear strain law is used. The shear yielding limit is defined as:

$$\tau_{pl} = \frac{f_y}{\sqrt{3}} \tag{40}$$

where τ_{pl} is the shear yield stress. As described in (Chen & Han, 1989), the von Mises criterion is based on the principle that the yielding of a ductile material is related to the second deviatoric stress invariant. The formulation used in the scope of this work is the von Mises equivalent tensile stress calculated with the Cauchy stress tensor. Therefore, only the tensile yield strength of the material used (steel) is required to define the plastic capacity of the fibers under tensile and shear stresses. The von Mises criterion is based on the physical interpretation that yielding of pressure independent materials begins when the octahedral shearing stress reach the critical value *k* as shown in equation (41).

$$\tau_{oct} = \sqrt{\frac{2}{3}J_2} = \sqrt{\frac{2}{3}}k \tag{41}$$

where τ_{oct} is the octahedral shear stress, J_2 the second invariant of the stress deviator tensor and *k* is the yield stress in pure shear of the material. Equation (41) may be rearranged to a simpler form such as:

$$J_2 = k^2 \tag{42}$$

The yield stress in pure shear of a pressure independent material is given by:

$$k = \frac{\sigma_y}{\sqrt{3}} \tag{43}$$

The second invariant of the stress deviator tensor is given by:

$$J_2 = \frac{1}{6}\left[\left(\sigma_x - \sigma_y\right)^2 - \left(\sigma_y - \sigma_z\right)^2 - (\sigma_z - \sigma_x)^2\right] + {\tau_{xy}}^2 + {\tau_{yz}}^2 + {\tau_{zx}}^2 \tag{44}$$

By combining equations (42), (43) and (44), the von Mises yield criterion, in terms of the Cauchy stress tensor components is given by:

$$\sigma_{VM} = \sqrt{\frac{1}{2}\left[\left(\sigma_x - \sigma_y\right)^2 + \left(\sigma_y - \sigma_z\right)^2 + (\sigma_z - \sigma_x)^2\right] + 3\left[{\tau_{xy}}^2 + {\tau_{yz}}^2 + {\tau_{zx}}^2\right]} \tag{45}$$

For the purposes of R_{pl}, equation (45) may be simplified. The equilibirium requires that (τ_{zx}= τ_{xz}) and only axial stresses σ_x are applied to the cross-section.

$$\sigma_{VM} = \sqrt{{\sigma_x}^2 + 3\left[{\tau_{xy}}^2 + {\tau_{xz}}^2\right]} \tag{46}$$

As mentioned in previous sections, the R_{pl} program has a stop criterion based on a maximum allowable strain ε_u. The total strain formulation, which is related to the von Mises criterion and the second invariant of the deviatoric strain tensor, will be used to calculate the equivalent axial strain of a fiber under axial and shear strains (Mendelson, 1968).

$$\varepsilon_p = \frac{\sqrt{2}}{3}\sqrt{\left(\left[\left(\varepsilon_x - \varepsilon_y\right)^2 - \left(\varepsilon_y - \varepsilon_z\right)^2 - (\varepsilon_z - \varepsilon_x)^2\right] + 6({\gamma_{xy}}^2 + {\gamma_{yz}}^2 + {\gamma_{zx}}^2)\right)} \tag{47}$$

where ε_p is the total equivalent strain. For the purposes of R_{pl}, equation (47) may be simplified, using ($\gamma_{zx} = \gamma_{xz}$), to:

$$\varepsilon_p = \frac{2}{3}\sqrt{\left({\varepsilon_x}^2 + \frac{3}{4}({\gamma_{xy}}^2 + {\gamma_{xz}}^2)\right)} \tag{48}$$

For each fiber, the equivalent strains are calculated using equation (48). The calculated strains are then verified against the maximum allowable strain ε_u defined as the plastic capacity analysis stop criterion.

The theory and implementation methods, for the program R_{pl}, have been detailed in this chapter. The next chapter will validate the accuracy and effectiveness of the R_{pl} program. This study will compare the plastic capacity results obtained using R_{pl} to results obtained using shell finite element models.

Chapter 3 – Validation study of the R_{pl} *2.0* program

The previous chapter detailed the theory and the general flow of operations of the R_{pl} *2.0* program. With R_{pl} *2.0* programmed and ready to be used, meshing density and validation tests will be performed. Before launching large-scale numerical studies, these tests will establish guidelines to ensure results accuracy. To properly validate the results provided by R_{pl} *2.0*, the general finite elements analysis program *ABAQUS* will be used as a reference tool. In *ABAQUS*, shell models will be used to accurately compute the plastic capacities of cross-sections.

To validate R_{pl} *2.0* and the shell models, different sections in terms of size and fabrication process will be studied. One hot-rolled and one welded doubly-symmetric I-beam and one welded singly-symmetric I-beam have been used for the mesh density and validations tests. The cross-sections are a hot-rolled W360x33, a welded doubly-symmetric WWF2000x732 and a singly-symmetric welded WRF1800x543. The bottom flange to top flange ratio (b_{fb} / b_{ft}) of the WRF1800x543 section is 1.83. As the bottom flange width is nearly twice as much as the top flange width, this section is well suited to study the effects of mono-symmetry on the results. The shell model length sensibility study has been conducted using a WWF500x456 cross-section. The length sensibility study will determine the required member lengths to use in the shell model to produce reasonably accurate plastic capacity results. These sections have been selected from the *Handbook of Steel Construction* (Canadian Institute of Steel Construction, 2010). The dimensions of these cross-sections are provided in Table 2.

Table 2 - Selected cross-sections and dimensions

Dimensions [mm]	W360x33	WWF2000x732	WWF500x456	WRF1800x543
h	349	2000	500	1800
b_{ft}	127	550	500	300
t_{ft}	8.5	50	50	45
b_{fb}	127	550	500	550
t_{fb}	8.5	50	50	45
w	5.8	20	20	18
r	16.5	-	-	-

Before comparing the plastic capacity results of R_{pl} *2.0* to *ABAQUS*, validation tests will be performed on the *ABAQUS* models to ensure (i) the suitability of the modeling techniques and (ii) reasonable meshing density of the three-dimensional shell models. The shell model results will be compared to analytical values to validate the accuracy of the numerical simulations. A notable difficulty arises from the fact that *ABAQUS* models are in three-dimensions, but the plastic capacity of a cross-section is fundamentally a two-dimensional problem. This indicates that instead of working only with a cross-section, the *ABAQUS* shell models will consider members with a defined length. Therefore, specific attention has been devoted to the modeling of the *ABAQUS* shell models and the interpretation of the calculated plastic capacities of the cross-section. Further details and specificities of the *ABAQUS* shell models are provided in the next sections.

Mesh density tests will also be performed for the R_{pl} program. The tests will determine the required number of divisions along the width and thickness of the constituting cross-section plates. As mentioned in earlier sections, the divisions in R_{pl} are represented by fibers with a single integration point at their center. The mesh density study will determine the required number of fibers to obtain results with a reasonable accuracy.

Finally, the results from R_{pl} *2.0* will be compared to the material non-linear analysis (M.N.A) results obtained using shell models in *ABAQUS*.

3.1 – *ABAQUS* shell model

Automated modeling tools have been developed specifically to generate the required input data to *ABAQUS*. This facilitates and increases the number of simulations performed by automating the process and launching multiple analyses with batch files. The shell element used for the purpose of this research is the "S4R" element in the *ABAQUS* library of elements. The M.N.A calculations have been performed using the Newton-Raphson algorithm with the arc-length resolution method. Automatic arc-length incrementation has been used throughout the tests.

3.1.1 – Material law used in *ABAQUS*

Although the R_{pl} *2.0* program possibly handles material strain hardening effects, as shown in Figure 11, an elastic-perfectly plastic material law has been used for the tests as shown in Figure 10. This decision has been made to simplify the comparison of the results obtained using numerical methods to the general formulas available in catalogues. Generally, the design standards interaction formulas do not consider strain hardening effects, therefore, for comparison purposes, no strain hardening is considered. The steel grade used is a 350W with a Young's modulus E of 200 GPa and a yield stress f_y of 350 MPa.

3.1.2 – Radiuses of hot-rolled cross-sections in *ABAQUS*

The radiuses of hot-rolled cross-sections have a non-negligible influence on the plastic capacities of the cross-section. The position of the radiuses, relatively to the neutral axis of the section, and their non-negligeable areas contribute to their beneficial effects on the plastic capacity of the section. Therefore, modeling of the radiuses cannot be omitted. Because the modeling is done with shell elements, a special technique has been used to introduce the radiuses and their effects in the model.

First, the web-to-flange zone of hot-rolled sections has been receiving a specific treatment, as shown in Figure 23. Within shell modeling, this region indeed suffers from (i) an overlap of material and from (ii) the disregarding of so-called "flange radius" areas. Both imprecisions may have a direct impact on the calculated plastic capacity of the section. The material overlap may cause an over-estimation of the plastic capacities. The omission of the radiuses may cause an under-estimation of the plastic capacities.

In order to fix thoses issues and to get closer to the real characteristics of such steel sections, an additional node has been placed within the web height, at the exact vertical position of the centroid of the radius zone. In addition to being linked with the shell elements of the web, this node bears an additional beam element, oriented in the member longitudinal direction, whose cross-section area is equal to that of the radius zones minus the overlapped area. Moreover, the section of this additional element is chosen to be a square hollow section, with height and thickness carefully adjusted so as to provide nearly-exact cross-sectional properties of the shell element in comparison to analytical ones, in particular with respect to the torsional inertia. It is also given the same constitutive law as the plate elements.

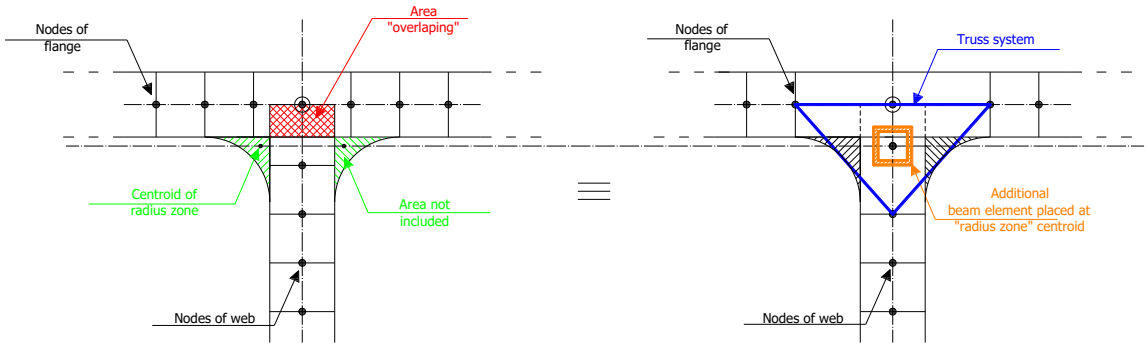

Figure 23 – Modelling principles of web-to-flange area

Another improvement is brought by the introduction of additional truss elements to maintain the area influenced by the flange radius more rigid, i.e. restrain local buckling at the web-to-flange junction. This truss system is composed of three elements with increased stiffness, making a rigid triangle. It implies the placement of adequate nodes at the foot of the radiuses in both the web and flanges, thus the non-equally spaced nodes observed in some of the figures. Such truss systems are also visible in Figure 24.

This particularly influences the torsional response of the section as recomposed by shell elements by limiting the local buckling of the section. Although, for M.N.A computations, the torsional response of the section is not of importance as local and global geometrical non-linearities are not considered. This modeling technique is implemented so the model may be used to consider the buckling effects as per the O.I.C. method.

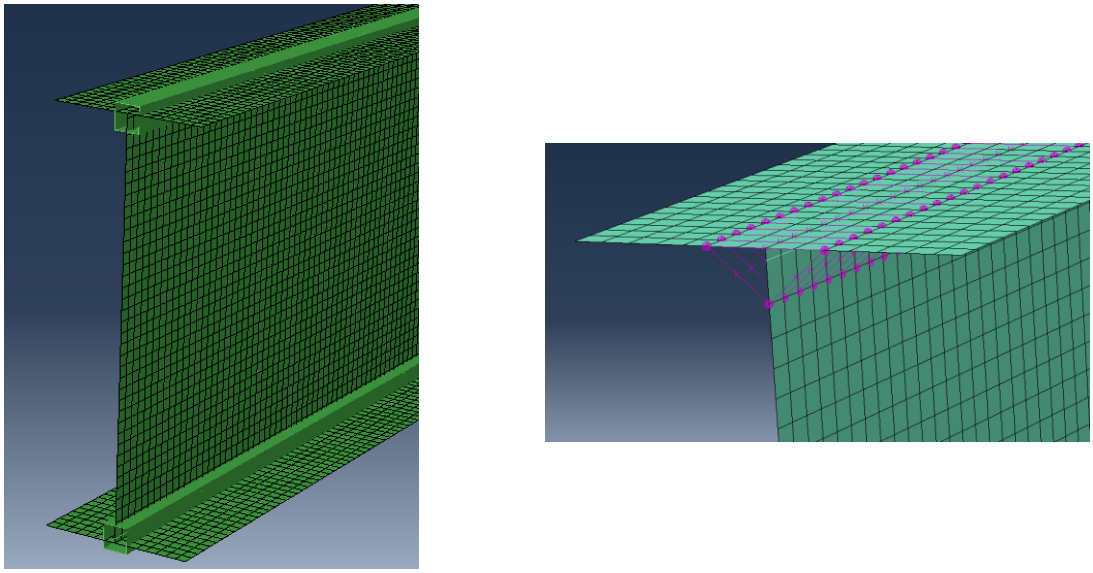

Figure 24 – Examples of F.E. modelling of web-to-flange area

As for welded sections, no such modelling refinements have been considered, since the influence of the weld is much smaller and has therefore been deemed negligible.

3.1.3 – Support conditions & loading

To respect Bernoulli's hypothesis that plane sections remain plane, special attention have been paid to support conditions at the extremities of the member. A common method to support the extremities of a member is the rigid end plate method. The rigid plate method generates a relatively thick plate at both extremities of the member. The rigid plate method simulates fixed support conditions at both extremities. Although the rigid end plate method is commonly used and simple to incorporate into a model, it has not been selected as this method restricts the warping of the member. The warping is restricted as the rigid plates restrict the flanges from moving along the x-direction of the member. Instead, fork support conditions have been used throughout the following studies. Figure 25 a) represents the boundary conditions applied at the end extremities of the beam. Vertical supports are applied at the flanges and lateral supports are applied at the web nodes to prevent local instability. A longitudinal support condition is applied at the centroid node of the member.

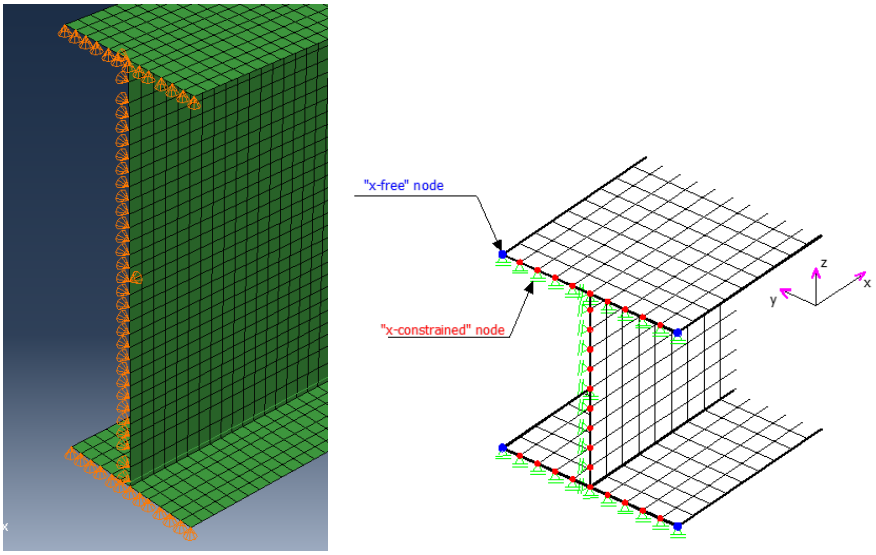

Figure 25- a) Fork support conditions b) Linear constraints

The tangent stiffness method presented earlier is based on the hypothesis that plane sections remain plane. Therefore, this hypothesis must also be respected in the shell models. Linear constraints, applied at the member extremities, have been used in the shell model to respect that hypothesis. Also, the linear constraints allow the warping of the section. Two linear constraints have been studied, the kinematic coupling constraints and the equation based linear constraints. Both methods are based on the principle of master nodes that control slave nodes.

The kinematic coupling constraints requires the selection of the degrees of freedom of the master node to enforce to the slave nodes. The degrees of freedom of the slave nodes are then eliminated in the global matrix assembly. Therefore, no other boundary conditions or constraints can be applied to the slave nodes.

The equation constraints do not remove degrees of freedom of the solution but instead links displacements of the slave nodes to the master nodes by the means of a linear equations. To replicate beam mechanics behavior in a shell model for open cross-section shapes, four global cross-section movements must be included such as: the axial displacement, the major-axis and minor-axis curvature and warping of the extremities. The master nodes are free to move in the longitudinal direction of the member and the slave nodes move according to the master nodes as described in Figure 25 b). Because of the good performance and behavior of the

equation constraints modeling technique, this method has been selected and implemented in the shell models.

As the constrained nodes move in the x-direction according to the plane created by the four free nodes, the loading has been applied to the free nodes by means of concentrated loads. To generate an axial load to the beam, equivalent concentrated loads, oriented in the same direction, are applied to the free nodes of the cross-section, thus creating the axial plane deformation as shown in Figure 26 a). The principle to generate a major-axis or minor-axis bending moment, respectively shown in Figure 26 b) and Figure 26 c), is similar. The method, described in Figure 26, generates constant bending moments along the length of the member. Depending on the desired curvature, concentrated loads of opposite directions are applied at the free nodes of the cross-section.

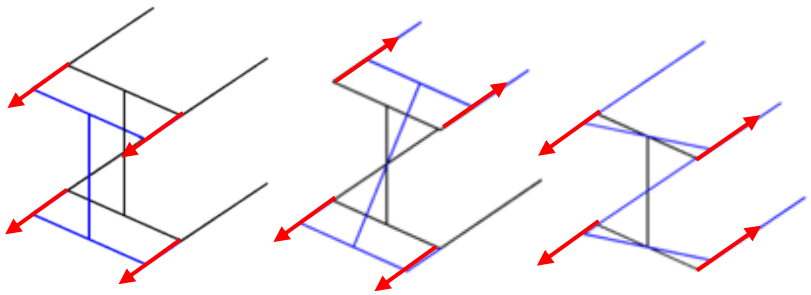

Figure 26- a) Axial deformation plane b) Major-axis curvature c) Minor-axis curvature

Generally, vertical shear loads in beams are applied by means of transverse loads along the beam. Thus, the transverse loading creates an accompanying bending moment. It is then difficult to determine the pure shear plastic capacity of a cross-section. A work around is to apply the shear loads to the web as if the web was an isolated plate, see Figure 27. Shear stresses, applied using concentrated loads, must be equal for each edge of the web. The concentrated loads are applied at nodes and are applied according to the shear stress pattern shown in Figure 27 a).

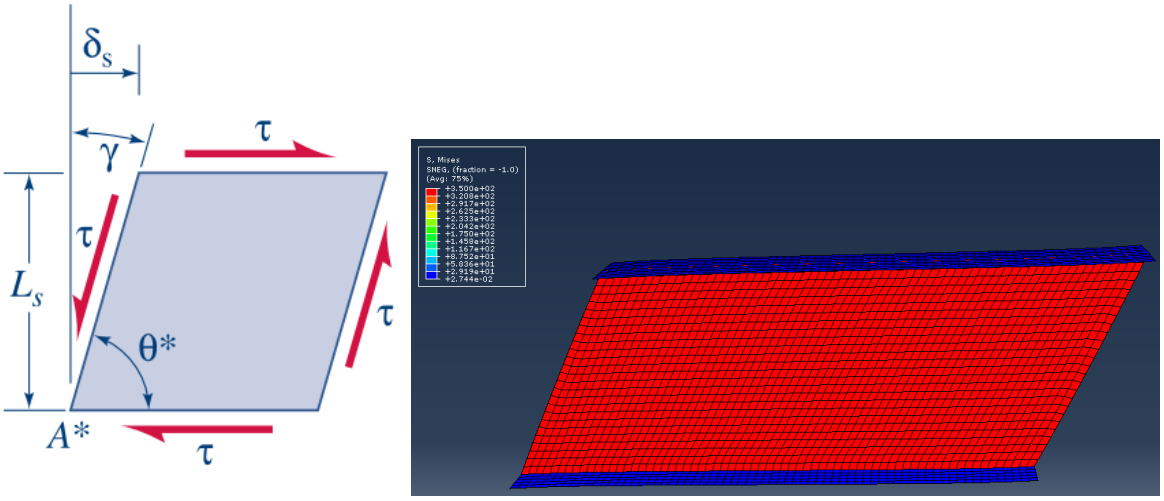

Figure 27 – a) Single plate shear stress (Craig JR., 2011) *b) Shear stress distribution on a beam in ABAQUS*

3.1.4 – Cross-section plastic capacity results of the shell models

The previous sections explained the details and techniques used to build the shell models. With the shell models built, M.N.A computations are ready to be launched. As mentioned earlier in this text, shell models are three-dimensional problems, although the plastic capacity of a cross-section is a two-dimensionnal problem. Therefore, the plastic capacity of a cross-section is not readily available. The cross-section plastic capacities will require an interpretation of the basic finite element results, such as the load proportionality factor and the nodal displacements. This section describes the techniques used to interpret the results and properly define the plastic capacities of the cross-section, from the three-dimensional shell model.

R_{pl} 2.0 and *ABAQUS* models are very different in nature. The R_{pl} tool is strictly limited to the cross-section behavior and therefore greatly simplifies the interpretation of the results. A maximum strain limit, for any given fiber, can be defined as the analysis stop criterion. Because full yielding is needed, a strain limit of 2% has been defined for all tests, which corresponds to approximately 1000% of the elastic strain limit of steel. The elastic strain limit of steel is 0.175%.

In the shell model, such parameter was not automated, and the interpretation of the results is slightly more complicated. Therefore, specific attention has been paid to extract and interpret key numerical data. As the concept of cross-section is non-existent in shell modeling, the

model must have a definite length. The task is to determine the plastic capacities of the beam cross-section with the beam modeled with shell elements.

The main difficulty is, for any kind of loading, to define a method to properly calculate the plastic load factor of the model. For loads inducing axial deformation, the method chosen consists of monitoring the displacements of one of the beam extremities. The displacements are extracted at the four master nodes used earlier to apply the loading to the beam. From the nodal displacements, the strains are calculated knowing the length of the beam and using the basic material mechanicals equation (49).

$$\varepsilon_x = \frac{\Delta L}{L} \tag{49}$$

The strains, calculated using equation (48), are calculated for each load step of the non-linear analysis. When the strain limit of 2% is reached, the load proportionality factor corresponding to the load step corresponds to the plastic capacity factor.

As this study comprises axial and shear loads, the cross-section extremities will undergo axial and shear deformations. Therefore, a von Mises like criterion, based on the deformations, has been used. From the shell model results, the axial deformation ε and the shear strain γ must be isolated and calculated. The plastic load factor is reached when the von Mises equivalent strain of 2% is reached at a given load step.

For a beam undergoing axial deformation only, either from simple or combined loading, the calculation of strains is straight forward as displacements at the nodes are readily available. For a beam under pure vertical shear, the nodes at the web-flange interfaces are used to extract the displacements and to determine the shear strain angle γ. The shear strain angle is calculated using the relative displacement of the nodes at the web/flange interface of a face. For combined major-axis bending moment and vertical shear, the interpretation of the results becomes more difficult as the movement of the end extremities are a combination of both types of loading. For each load step, the axial deformations ε and the shear strains γ are individually calculated by monitoring the relative displacements of both extremities of the beam.

Now that the plastic capacity of cross-section can be calculated from three-dimensional shell models, for various types of loading; the next sections will perform the shell model validation studies.

3.1.5 – Effect of beam length on the results

A study specifically aimed at determining the effect of the length of the beam on the results is presented in this section. The shell finite element analyses are performed without considering non-linear geometrical effects, thus only considering material non-linearities. It is then of interest to verify the influence of the length of the member on the plastic capacity results. To ensure the validity of the following numerical tests, the mesh along the plates of the cross-section will be very fine. By doing so, only the length of the beam may have an influence on the plastic capacities. The tests will be conducted according to ratios of the cross-section height L / h, ranging from 0.5 to 7 times the height of the cross-section. A WWF 500x456 cross-section is considered and tested for axial, major-axis and minor-axis bending moments as well as vertical shear loads. The tested lengths for that cross-section are shown in Table 3.

Table 3 - Tested lengths for cross-section WWF 500x456

L / h [–]	0.5	1	1.5	2	2.5	3	4	5	6	7
L [mm]	250	500	750	1000	1250	1500	2000	2500	3000	3500

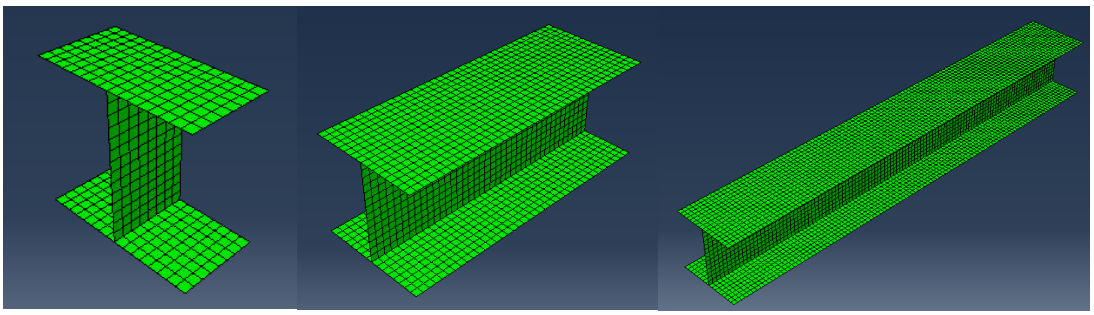

Figure 28 - Beam with L/h ratios of a) 0.5 b) 2.5 and c) 7

The first series of tests, to determine the effect of the member length on the plastic capacity of the cross-section, were conducted for a major-axis bending moment. The results show that numerical issues occurred when the beam is very stocky. For ratios of L / h under 2, the cross-section could not reach the plastic strain criterion of 2% and the phenomenon of load reversal

occurred. Simply, the non-linear algorithm could not converge toward a solution and bifurcated to an alternate solution where the direction of the loading is reversed. For ratios of L / h greater than 2, the non-linear material analysis was stable and the plastic capacity results were very similar. Indeed, the maximum difference observed on the results was 0.01%.

The second series of tests were conducted for a minor-axis bending moment loading type. Similar to the first series of tests, beams with ratios L / h under 2 could not reach the plastic strain criterion of 2%. For ratios of L / h greater than 2, the maximum difference observed on the results was 0.27%.

The third series of tests were conducted for a vertical shear load. Contrarily to previous tests, the ratio L / h did not have a considerable effect on the stability and accuracy of the results. Yet, it has been observed that the plastic capacity results were more precise with larger values of L / h. Lower values of L / h tended to overestimate the cross-section vertical shear plastic capacity by not much than 0.73%. As a cause, the boundary conditions effects on the results increase as the member gets shorter.

In conclusion, too short of a member does not give accurate results. When the member is shorter than twice the height of the cross-section, the gathered results had not reached the stop criterion of 2% strain. Not only the deformation criterion has not been reached, but the overall convergence of the model is also not deemed proper. Load reversal and divergence of the model is observed for overly stocky members. Therefore, a conclusion can be made that member length, for the numerical simulations, must be greater than twice the height of the cross-section. With the guidelines on the required member length determined, the next section will perform the validation of the three-dimensional shell models and mesh density tests.

3.1.6 – Shell meshing density study & *ABAQUS* models validation

The previous section studied the effect of the length of the beam on the plastic capacity results of the shell models. The following sections will apply the recommendations on the minimal member length to ensure proper results. As mentioned previously, beam behavior modeled with shell models requires a three-dimensional approach. Therefore, the number of divisions along each plate and along the length of the beam will be studied.

Using analytical reference values on the plastic capacities of a beam, both the mesh density and the modeling techniques of the *ABAQUS* models will be validated in this section. The models to be tested will consist in hot-rolled and welded cross-sections. Because of the various loading possibilities, the mesh density study will be conducted for various single load cases. The mesh density may have an influence depending on the direction where the stresses, generated by the loading, vary. The loading cases that will be studied are axial, major-axis and minor-axis bending moments and vertical shear loads.

The user-interface modeling tools in *ABAQUS* have not been used for this study. Instead, a custom program developed in *Excel* has been used to generate the shell models and their specific modeling features. Therefore, the meshing of the shell model can be fully controlled. Although it might have proven useful to have separate plate discretization parameters for the flanges and the web, to simplify the user's input, the cross-section plates discretization is controlled by only one parameter. Therefore, the plates of the cross-section all have the same number of divisions, according to the input of divisions by the user. This may cause an overly dense meshing along the flanges if the web height is much larger than the flanges width. Generally, quadrilateral shell elements perform better when they are not distorted. Because the mesh generation tool targets an aspect ratio of the shell element close to 1.0 (square elements), the divisions along the length of the beam are governed by the plates shell elements sizes. Therefore, the main variable is the number of divisions along the flanges of the cross-section. The number of divisions along the web depends on the number of divisions of the flanges and is calculated to obtain square elements along the length of the member.

Contrarily to the tangent stiffness approach, plate thicknesses, in shell models, are not explicitly modeled. Shell elements are geometrically plane elements with a given thickness. Instead of having multiple fibers along the thickness of plates, shell elements have integration points along their thickness to capture the gradual yielding under flexure. Mesh density will influence the precision of the plastic distribution of stresses and displacements within the finite elements.

Results with a very densely meshed shell model will be compared to those analytical values. This comparison is aimed toward validating the *ABAQUS* shell modeling techniques used.

Then, the cross-sections will be divided into various meshes, varying from coarse to dense meshing. The numerical tests will be conducted on a W360x33 hot-rolled cross-section.

The initial step is to calculate the plastic capacities analytical values. The *Handbook of Steel Construction* (*HSC*) (Canadian Institute of Steel Construction, 2010) directly provides the axial, major-axis and minor-axis bending and vertical shear plastic properties of the W360x33 cross-section, with respectively A_g = 4170 mm^2, Z_z = 542x10^3 mm^3, Z_y = 71.8x10^3 mm^3 and A_v = 2024.2 mm^2. Although readily available, the calculations of those properties are not explicitly detailed in the *HSC*. To ensure the validity and accuracy of the properties extracted from the *HSC*, alternative equations found in (ArcelorMittal, 2009) have been used to calculate the plastic section modulus for both bending axes and the plastic vertical shear area as shown by equations (50), (51), (52) and (53).

$$A_g = 2t_f b + \left(h - 2t_f\right)t_w + (4 - \pi)r^2 \tag{50}$$

$$Z_z = \frac{t_w h^2}{4} + (b - t_w)\left(h - t_f\right)t_f + \left(\frac{4 - \pi}{2}\right)r^2\left(h - 2t_f\right) + \left(\frac{3\pi - 10}{3}\right)r^3 \tag{51}$$

$$Z_y = \frac{b^2 t_f}{2} + \frac{h - 2t_f}{4}{t_w}^2 + r^3\left(\frac{10}{3} - \pi\right) + (2 - \frac{\pi}{2})t_w r^2 \tag{52}$$

$$A_v = A_g - 2bt_f + (t_w + 2r)t_f \tag{53}$$

The properties calculated using these equations are respectively A_g = 4318.3 mm^2, Z_z = 565x10^3 mm^3, Z_y = 72.8x10^3 mm^3 and A_v = 2489.1 mm^2. Table 4 presents the calculated plastic capacities from both the *HSC* and equations (50) to (53) for the various types of loading.

Table 4 – Analytical plastic capacities of a W360x33 cross-section

W360x33				
	N_p [kN]	M_{zp} [kN*m]	M_{yp} [kN*m]	V_{yp} [kN]
(*HSC*)	1459.5	189.7	25.1	409.0
Eq.(50)-(53)	1511.4	197.8	25.5	503.0
Variation [%]	-3.6	-4.3	-1.5	-23.0

A first observation from the table above is that the plastic capacity values from equations (50) to (53) are higher than the values from the *HSC*. The variations between the *HSC* and equations (51) and (52) values of Z_z and Z_y are respectively 4.3% and 1.5%. These variations may be attributed to the proper calculation of the radiuses effect on the cross-section geometrical properties. Because the radiuses exact dimensions are not directly provided in the *HSC*, the W360x33 cross-section plastic capacities will be calculated without the radiuses using equations (50) to (53).

Table 5 – Effect of radiuses on the analytical plastic capacities of a W360x33 cross-section

W360x33				
	N_p [kN]	M_{zp} [kN*m]	M_{yp} [kN*m]	V_{yp} [kN]
Eq.(50)-(53) (r=0.0)	1429.6	184.6	25.0	399.1
Eq.(50)-(53) (r=16.5)	1511.4	197.9	25.5	503.0
Variation [%]	-5.7	-7.2	-2.0	-26.0

From the results of Table 5, it is therefore evident that for hot-rolled cross-sections, the radiuses influence is not negligible on the plastic capacities results and that they must be included in the model as to not underestimate the plastic capacity of the cross-section. The radiuses affect mainly the axial, major-axis bending and major-axis shear plastic capacities with respective variations of -5.7%, -7.2% and -26.0%. The minor-axis bending plastic capacity is less affected by the omission of the radiuses as the radiuses areas are very close to the neutral axis of the cross-section, thus not participating less to the bending resistance.

The major difference from both references is the vertical shear plastic capacity. As shown in equation (53), the radiuses are taken into consideration for the calculation of the shear area whereas the *HSC* method only considers, for hot-rolled cross-sections, the web area extended into the flanges. Therefore, it can be observed that the flanges, in equation (53), contribute in a larger extent to the total shear area than in the *HSC*, hence the larger shear plastic resistance.

As mentioned earlier in Section 2.2.2, an assumption has been made that radius do not influence the vertical shear capacity of beams. From that hypothesis, the reference vertical shear value will be the one from the *HSC*. The axial and bending moment plastic capacities reference values selected are from equations (50) to (52), as the radius may withstand axial stresses and therefore participate in the axial and bending resistances.

With the reference plastic capacities defined, the mesh density study for the W360x33 may be performed. Figure 32 displays the error percentage of the calculated plastic capacities, for various mesh densities, compared to the analytical results. Figure 29, Figure 30 and Figure 31 represent various meshing densities tested, ranging from a coarse mesh density to a very fine mesh density.

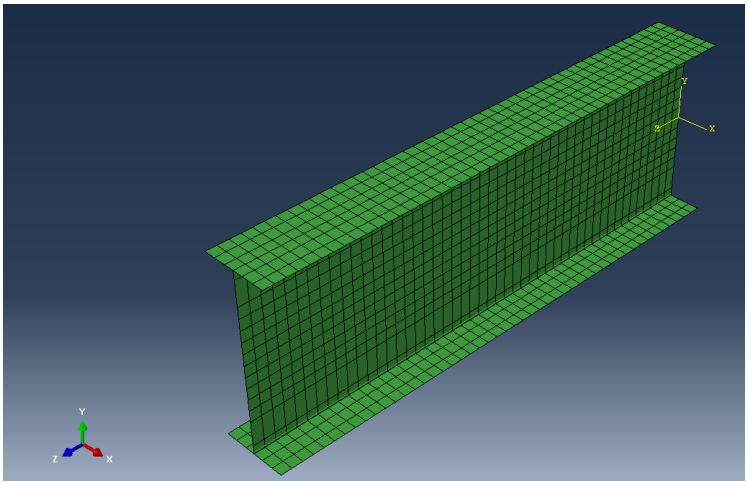

Figure 29 – Coarse mesh density (6 divisions)

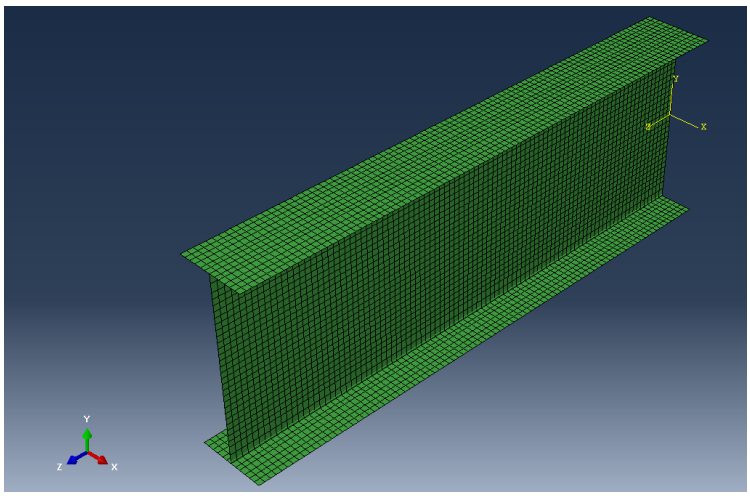

Figure 30 – Fine mesh density (12 divisions)

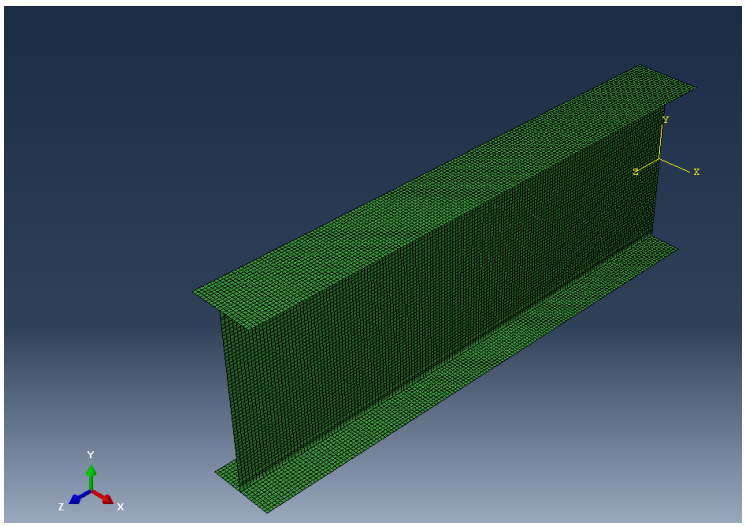

Figure 31 – Very fine mesh density (20 divisions)

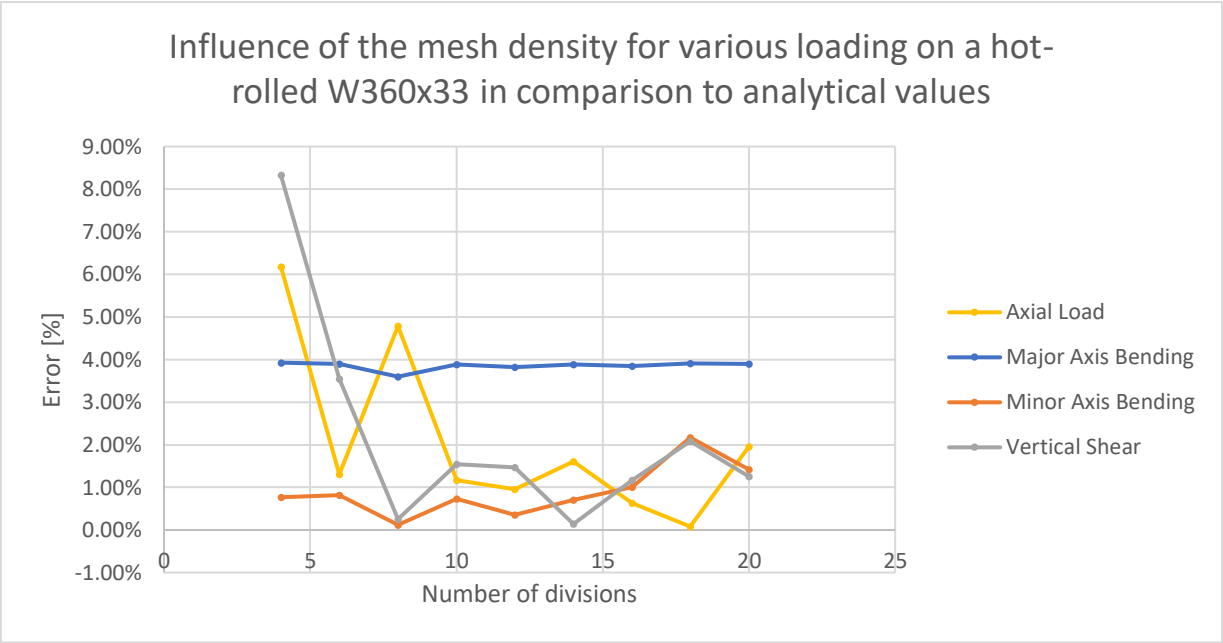

Figure 32 – Mesh density results for various loading for a W360x33

A first observation from Figure 32 is that the mesh density does have a non-negligeable influence for the axial loading. A coarse mesh (ten divisions and less) produces an unacceptable error of 6.17%. As the number of divisions increases, the error on the axial plastic capacity oscillates between 0.08 to 1.95%. The major-axis bending results are not sensible to the mesh density as much as the other types of loads. The maximum variation of the error percentages is only 0.33% for all mesh densities. The minor-axis bending results show more variations, with a maximum difference of the error percentages of 2.05%. The error percentage, for the minor-axis bending, is acceptable for coarse and finer meshes. The mesh density does have a considerable influence on the vertical shear results. The difference on the error percentages is 8.18%. From this observation, mesh densities below eight divisions along the plates do not provide accurate results. Also, it can be seen that a very high number of divisions along the plates do not necessarily translate to more precise results as shown by the minor-axis bending and vertical shear results. For that reason, the shell model may not need to be finely meshed to attain proper convergence. Combined with the fact that more divisions require more computing time to solve the numerical simulation, a number of ten to sixteen divisions along the plates is deemed reasonable.

From the conclusions of this mesh density study, the shell model numerical results will be compared to the analytical values. From this comparison, the modeling of the shell model will be verified. The numerical plastic capacities chosen will be an average of the numerical values obtained from the shell model with divisions along the plates of ten to sixteen.

Table 6 – Shell model plastic capacities of a W360x33 cross-section

W360x33				
	N_p [kN]	M_{zp} [kN*m]	M_{yp} [kN*m]	V_{yp} [kN]
Eq.(50)-(53)	1511.4	197.9	25.5	409.0
Shell model	1535.7	205.4	25.4	410.0
Variation [%]	-1.6	-3.8	0.6	-0.2

While the mesh density study above has provided conclusive results for doubly-symmetric cross-sections, verifications will be conducted for singly-symmetric cross-sections. The plastic capacities of a WRF1800x543 will be numerically calculated, using fourteen divisions, and verified against analytical values.

Table 7 - Shell model plastic capacities of a WRF1800x543 cross-section

WRF1800x543				
	N_p [kN]	M_{zp} [kN*m]	M_{yp} [kN*m]	V_{yp} [kN]
HSC	24 220.0	15 737.8	1593.9	6219.8
Shell model	24397.00	15 680.70	1586.77	6379.01
Variation [%]	-0.7	0.4	0.5	-2.6

Table 7 presents the plastic capacities results of the shell model for a mono-symmetric I-beam. The error percentages are well into acceptable limits, with the vertical shear having an error of 2.56% compared to the analytical value. These tests validate the shell modeling techniques for mono-symmetric cross-sections.

In summary, it has been determined that the length of the finite element shell model does have an influence on the results. To ensure an accurate behavior of the model and proper results, a length of at least twice the cross-section height is required. From the mesh density

tests, the number of divisions along the plates of the cross-section is also an important parameter to obtain accurate plastic capacities. Ten to sixteen divisions along the plates are required. For the remainder of the study, the number of divisions along the plates chosen is fourteen as it is a good compromise between precision and computing times. Finally, a mono-symmetric cross-section has been analysed using shell models to confirm that the shell modeling techniques are also valid for mono-symmetric cross-sections. Indeed, the modeling techniques are valid for both doubly and mono-symmetric cross-sections.

3.2 – *R_{pl} 2.0* mesh density study & model validation

A mesh density study in *ABAQUS* has been conducted, for various type of loading, to determine the required number of divisions along the plates of the cross-section to obtain satisfying precision on the results. To ensure adequate comparisons between R_{pl} and *ABAQUS* numerical simulations, a mesh density study has also been conducted for the R_{pl} tool.

As opposed to the *ABAQUS* model, where the plates are only discretized along their length, the cross-section plates in R_{pl} are discretized along their width and along their thickness by fibers. The meshing in R_{pl} consists of dividing each plate of the cross-section in $m_x n$ elements as illustrated in Figure 33.

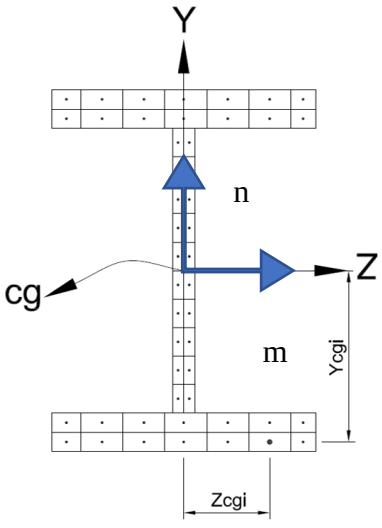

Figure 33 - Cross-section plate discretization

This discretization method allows for faster computing times for known types of loading. Different loadings will require different configurations of the meshing. For example, a major-

axis bending moment will require a finer meshing along the thickness of the flanges and along the height of the web to capture the yielding of the extreme fibers as opposed to a minor-axis bending moment, where the fibers at the tips of the flanges will yield first. From that logic, a major-axis bending moment would require a high number of divisions in the *n* direction and a minor-axis bending moment would require a high number of divisions in the *m* direction. In the case of a major-axis bending moment, reducing the number of elements along the width of the flanges may provide faster computing times while maintaining adequate results accuracy. For vertical shear loads, the distribution of the shear stresses would require the web of the cross-section to be densely meshed along the heigh of the web *n*. Further details will be given for the mesh density requirements for vertical shear loads.

The notions above demonstrate, generally, the importance of having adequate divisions along the direction of loading. Although simple for single load cases, the cross-section mesh density study must also consider combined load cases. Therefore, the goal of the mesh density study is to determine a general meshing configuration that provides accurate results, whatever the the load case, while still maintaining a reasonable time efficiency of the program.

Other factors such as the non-linear load step factor, which controls convergence and precision, are considered being precise enough to have very little influence on the results compared to the meshing quality.

To determine an appropriate meshing for most sections, the study will be conducted with a large section. A large section has been selected to demonstrate that the meshing density is relative. The meshing requirements here will apply in general to other sections. The section selected is a welded WWF2000x732 cross-section.

The analytical values for the WWF2000x732 are calculated using the same equations as in section 3.1.3. The plastic properties from the *HSC* are respectively $A_g = 93200$ mm^2, $Z_z = 71800\text{x}10^3$ mm^3, $Z_y = 7750\text{x}10^3$ mm^3 and $A_v = 38000$ mm^2. The plastic properties calculated using equations (50) to (53) are respectively $A_g = 93000$ mm^2, $Z_z = 71675\text{x}10^3$ mm^3, $Z_y = 7752\text{x}10^3$ mm^3 and $A_v = 39000$ mm^2.

Table 8 - Analytical plastic capacities of a WWF2000x732 cross-section

WWF2000x732				
	N_p [kN]	M_{zp} [kN*m]	M_{yp} [kN*m]	V_{yp} [kN]
HSC	32 620.0	25 130.0	2712.5	7678.8
Eq.(50)-(53)	32 550.0	25 086.3	2713.4	7880.8
Variation [%]	0.2	0.2	-0.0	-2.6

In R_{pl}, for a purely axial load, the number of divisions of each plate is less important. The reason is that there is no variation of stresses in the cross-section. An axial load stress is constant over the area of the section. Therefore, the analysis of any section under axial load should be done with a minimum of elements to optimize the computation time.

In R_{pl}, for major-axis bending, divisions along the width *m* of the section will remain constant. For this type of loading, the important divisions are along the height *n*, where there is a variation in stresses and thus in deformations. For minor-axis bending, the divisions along the height *n* of the section will remain constant and the divisions along the width *m* will vary. Figure 34 shows the error percentage trends with various meshing densities for the welded WWF2000x732 section shape. Welds are neglected.

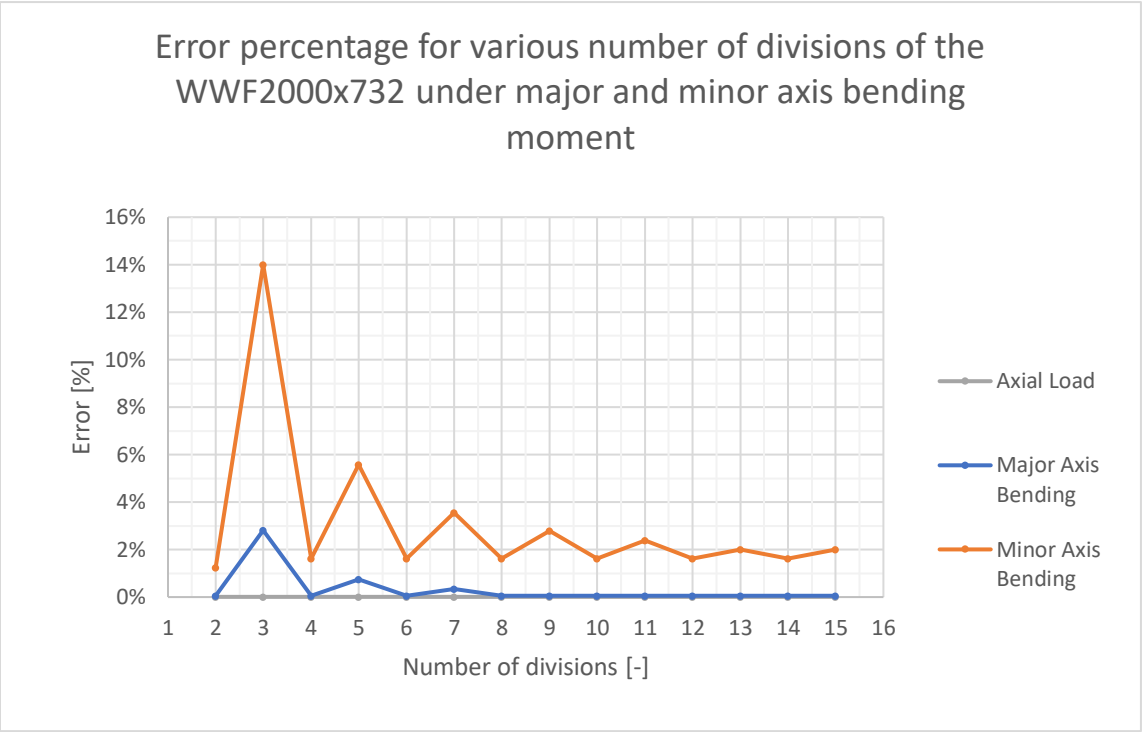

Figure 34 - Mesh density tests for a WWF2000x732

Before discussing the results displayed in Figure 34, the method to calculate the error percentages will be described. The plastic capacities calculated using R_{pl} are compared to the plastic capacities calculated using equations (50) to (53). The error percentage is calculated according to equation (54).

$$Error\ \% = abs\left(\frac{M_{Rpl} - M_{zp}}{M_{Rpl}}\right) * 100 \tag{54}$$

For major-axis bending, the maximum error is in the order of 2.8% compared to the analytical values from equations (50) to (53). The calculated major-axis plastic bending moment in R_{pl} is 24400.0 kN-m compared to 25086.3 kN-m. The average plastic bending moment, for a mesh density of 8 divisions and higher, is 25100 kN-m. The average error percentage stabilizes at around 0.05% when the cross-section is divided by more than 8 divisions *n*.

For minor-axis bending, the maximum error is in the order of 14.0% compared to the analytical values from equations (50) to (53). The calculated major-axis plastic bending moment in R_{pl} is 2380.0 kN-m compared to 2714.4 kN-m. The average plastic bending

moment, for a mesh density of 8 divisions and higher, is 2661.3 kN-m. The average error percentage stabilizes at around 1.9% when the cross-section is divided by more than 8 divisions *m*.

The axial plastic capacities are not influenced by the meshing density and the error percentage is near 0%.

For both the major-axis and minor-axis bending, a meshing density of less than 4 divisions is inadequate. Although reasonable even with a coarse mesh (4 to 6 divisions), the more divisions, the more constant the results become. Figure 34 clearly shows a pattern that even divisions generate less errors than uneven divisions. Theses variations are caused by the numerical integration technique where only one integration point at the center of a fiber is used. Therefore, the position of the center of each element relative to the plastic neutral axis of the cross-section influences the results. For even number of elements within each plate, the center of gravity of the elements do not land directly on the neutral axis of the section. This enables each plate and its tributary area to fully contribute to withstand the applied bending moment. Otherwise, the lever arm of the element is zero and do not receive any stresses as the stresses are zero at the neutral axis of the section. For major-axis bending moments, the areas where divisions matter the most are i) at the extreme position of the flanges, near the maximal stresses and strains of the cross-section and ii) in the web, near the center of gravity of the cross-section. The divisions at the extreme position of the flanges are crucial to capture the initial yielding of the cross-section. The divisions in the web are important to capture the final stage of yielding of the cross-section, near the plastic neutral axis. From Figure 34, the error percentage become very consistent when there are more than 8 divisions for all loading types. Because computing times are not significant, even at 15 divisions, this value of *n or m* divisions is recommended and will be used for the rest of this study.

For vertical shear loading, the divisions along the width *m* and along the length *n* of the plates will be incremented simultaneously. For this type of loading, the most important divisions are along the height *n*, where there is a variation in shear stresses and thus in shear strains. The vertical shear area determined in R_{pl} has been determined using a centerline shear

distribution model, as shown in Figure 35. Therefore, the web shear area is extended up to the flange and web centerline intersections.

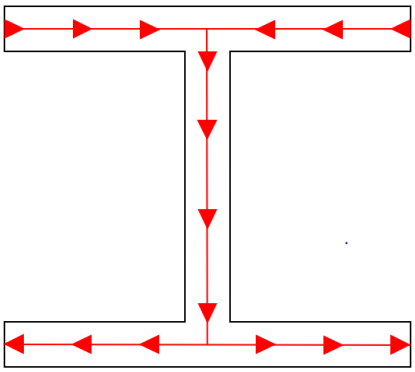

Figure 35 - Centerline shear distribution

Using the center of gravity of the fibers, a verification is performed to determine if a fiber is comprised within that area. It is important for the fibers to be properly discretized along the width of the plate so that the total area of the fibers flagged inside the shear area zone corresponds to the actual shear area, as illustrated in Figure 36. Figure 37 displays a fiber that is not considered in the shear area as the c.g of the fiber is outside the shear area. Therefore, the *m* divisions along the width have an influence on the results.

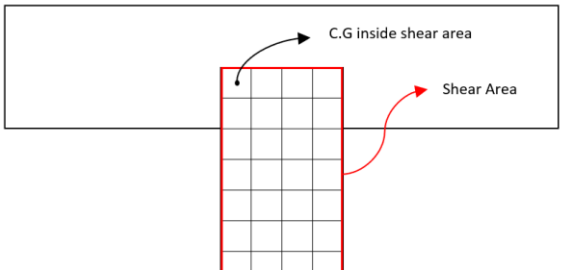

Figure 36 – Center of gravity of a fiber within the shear area

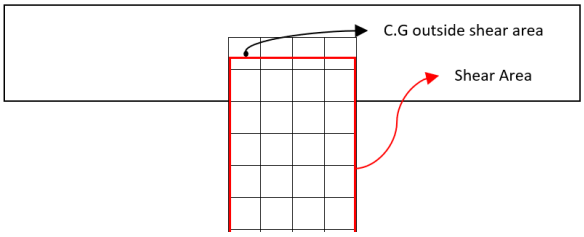

Figure 37 - Center of gravity of a fiber outside the shear area

Figure 38 shows the error percentage trend for the welded WWF2000x732 under vertical shear loading.

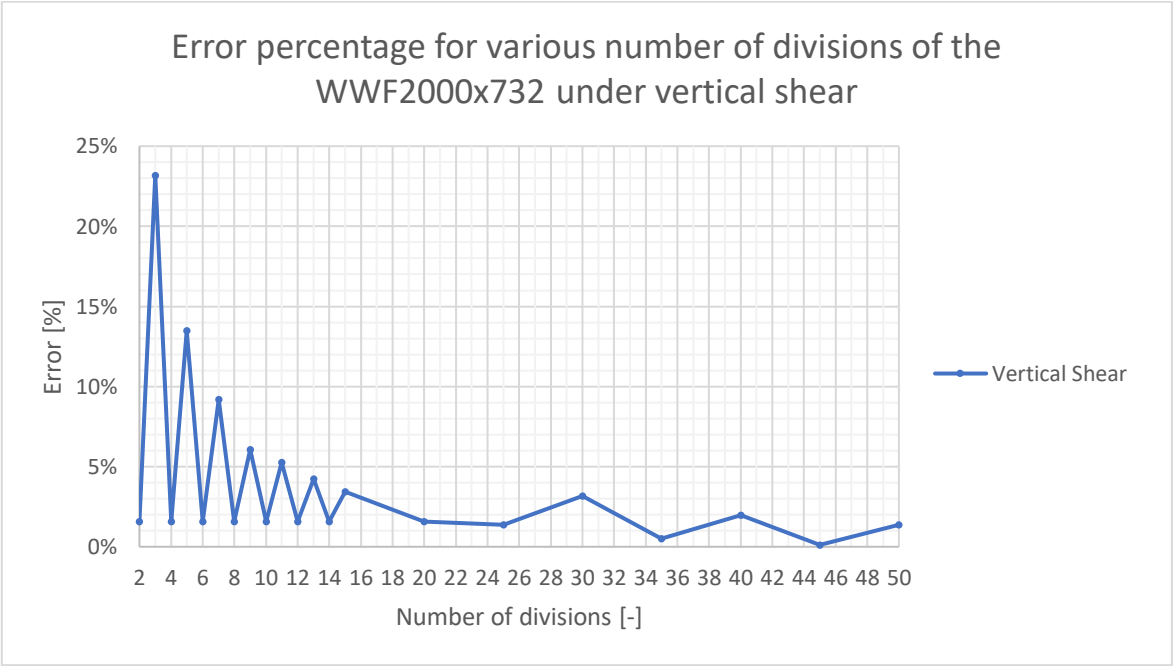

Figure 38 - Mesh density tests for a WWF2000x732 under vertical shear

As expected, the mesh density, for vertical shear loading, has a drastic importance on the accuracy of the results. The maximum error is in the order of 23.0% compared to the

analytical values from equations (50) to (53). The major variations, for low number of divisions, are caused by an over-estimation of the shear area due to the flange fibers. For uneven divisions, the center of gravities of the middle row fibers are technically in the shear area zone, altough spreading much beyond the expected shear area. Using more divisions, the shear area considered by the program becomes more precise. To obtain results with an error consistently less than 5%, 12 divisions along *m* and *n* are required. From the conclusions of the major-axis and minor-axis mesh density study, 15 divisions will produce reasonnably accurate results for major-axis shear load cases.

Contrarily to doubly-symmetric cross-sections, the plastic neutral axis of singly-symmetric cross-sections does not coincide with the geometrical center of gravity of the cross-section as the fibers progressively yield. Figure 39 illustrates the fully elastic and fully plastic state of the cross-section. As shown in Figure 39, the plastic neutral axis has shifted away from the elastic neutral axis. Such shift of the plastic neutral axis motivates the following mesh density study on a singly-symmetric cross-section. The tests have been performed using a WRF1800x543 mono-symmetric welded section.

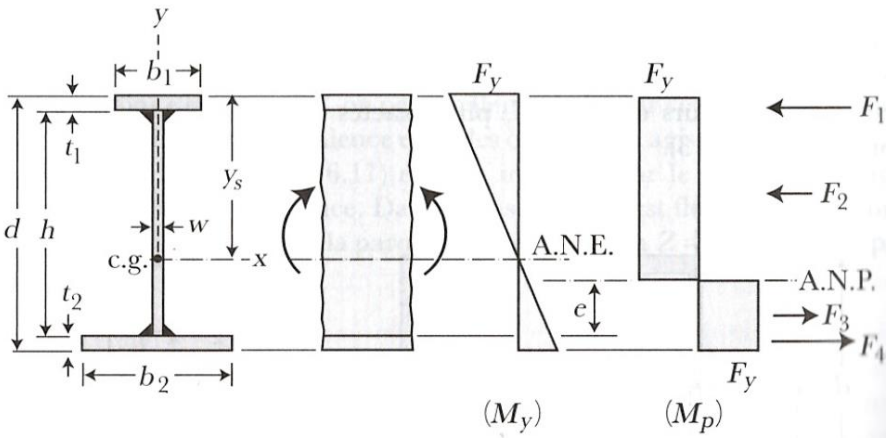

Figure 39 – Elastic and Plastic neutral axis of a mono-symmetric cross-section (Beaulieu, Tremblay, & Grondin, 2005)

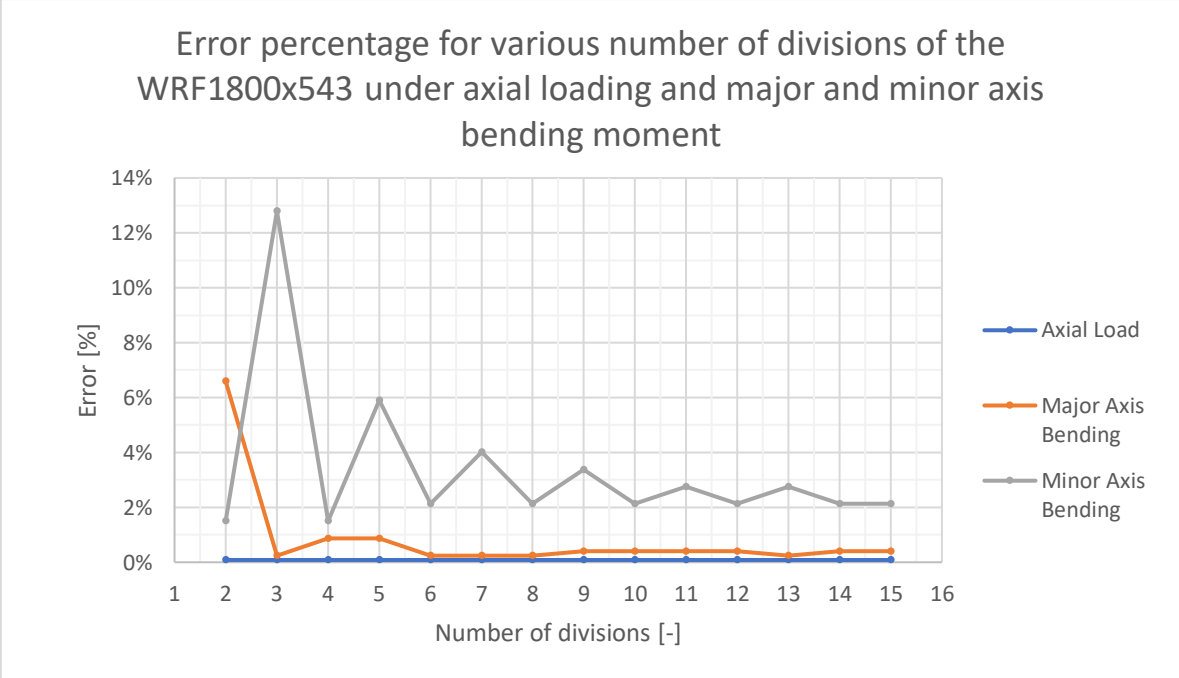

Figure 40 - Mesh density tests for a WRF1800x543

Figure 40 demonstrates that coarse meshing is not adequate for mono-symmetric cross-sections. It also shows that the number of divisions required (*n=3)* for a major-axis bending moment, to obtain resonnable results, is slightly lower than for doubly-symmetric sections (*n=4)*. Although, for the mono-symmetric cross-section, a coarse meshing produces an error higher (6.59%) than the doubly-symmetric cross-section (2.81%). Contrarily to doubly-symmetric sections, the plastic neutral axis does not correspond, in the elastoplastic phase, to the center of gravity of the cross-section. It is therefore the reason a finer meshing is

required, to better represent the spread of plasticity in the web. The position of the plastic neutral axis governs the equilibrium of the stresses in the cross-section. The finer meshing improves the position accuracy, thus improving the stresses equilibrium calculations.

The minor-axis of a mono-symmetric cross-section being symmetric, Figure 40 demonstrates that the mesh density under a minor-axis bending moment displays the same pattern as a doubly-symmetric cross-section. Consistent results are obtained for ten and higher divisions.

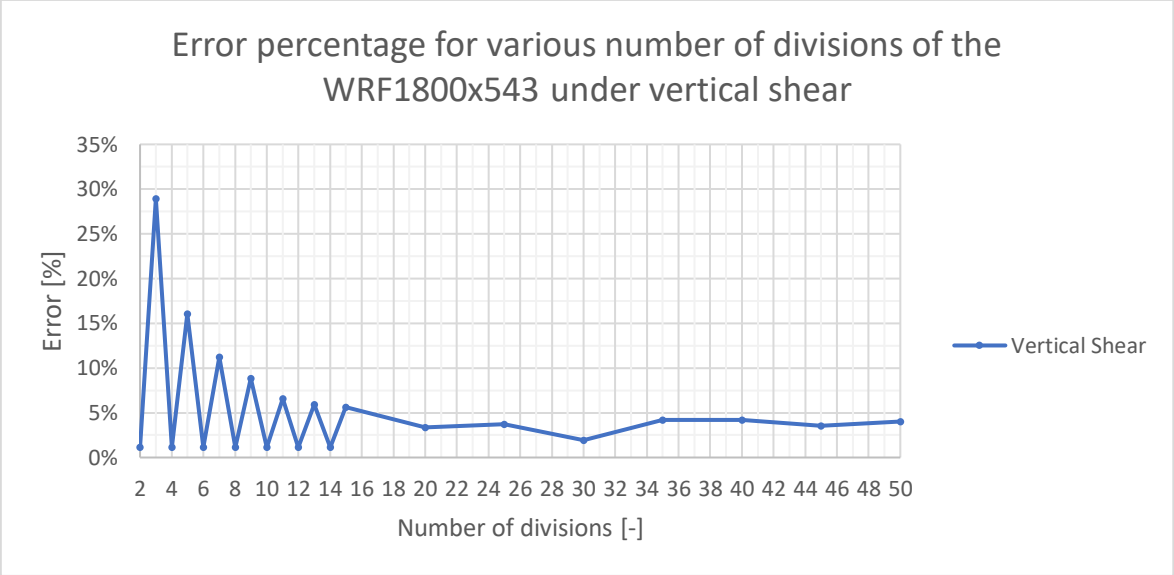

Figure 41 - Mesh density tests for a WRF1800x543 under vertical shear

Figure 41 displays the mesh density results for the mono-symmetric WRF1800x543 cross-section. The high error percentage is directly linked to an over-estimation of the shear area caused by the coarse meshing. For the mono-symmetric cross-section, the error stabilizes under 5% when the divisions (*m* and *n*) are greater than fifteen.

For the WRF1800x543, Table 9 compares the plastic capacities calculated with R_{pl} and the analytical values. Because equations (50)-(53) apply only to doubly-symmetric sections, the analytical values from the *HSC* are taken.

Table 9 - R_{pl} plastic capacities of a WRF1800x543 cross-section

WRF1800x543				
	N_p [kN]	M_{zp} [kN*m]	M_{yp} [kN*m]	V_{yp} [kN]
HSC	24 220.0	15 737.8	1593.9	6219.8
R_{pl}	24 170.0	15 720.0	1560.0	6470.0
Variation [%]	0.2	0.1	2.1	4.0

As a continuity of the shell model study from the previous section, the plastic capacities for a W360x33 will be calculated using R_{pl} and compared against the analytical values.

Table 10 - R_{pl} plastic capacities of a W360x33 cross-section

W360x33				
	N_p [kN]	M_{zp} [kN*m]	M_{yp} [kN*m]	V_{yp} [kN]
Eq.(50)-(53)	1511.4	197.9	25.5	409.0
R_{pl}	1507.0	198.0	25.4	410.0
Variation [%]	0.3	0.1	0.6	0.2

Table 10 clearly indicates that R_{pl} provides very accurate results while being much simpler to use than full three-dimensional shell models. Finally, plastic capacities from R_{pl} and the shell models are compared in Table 11.

Table 11 - Plastic capacities comparison of R_{pl} *and the shell models*

	N_p [kN]	M_{zp} [kN*m]	M_{yp} [kN*m]	V_{yp} [kN]
W360x33				
Shell model	1535.7	205.4	25.4	409.9
R_{pl}	1507.0	198.0	25.4	410.0
Variation [%]	1.9	3.6	0.0	0.0
WRF1800x543				
Shell model	24 397.0	15 680.7	1586.8	6379.0
R_{pl}	24 170.0	15 720.0	1560.0	6470.0
Variation [%]	0.9	0.3	1.7	-1.4

Table 11 confirms that R_{pl} provides accurate results for the load cases studied in this chapter. From that confirmation, plastic capacities studies with combined loadings will be performed in the next chapter.

In summary, this chapter aimed at describing and validating the finite element shell modeling techniques. Length and mesh density studies have been conducted for various shell models. Also, mesh density studies have been conducted for R_{pl}. Plastic capacities, for both tools, have been compared to analytical plastic capacity values. With both tools validated for simple load cases, combined load cases will be studied in the next chapter. Using the shell models as a reference, interaction diagrams will be built and verified using interaction diagrams to validate the accuracy of R_{pl} *2.0* for combined loading cases.

Chapter 4 – Plastic capacity of cross-sections under combined loading

The previous section validated the modeling techniques used for the shell FE models and R_{pl} *2.0*. Also, several numerical simulations validated the R_{pl} *2.0* plastic capacities calculations for single load cases. To reach the objectives of this thesis, the R_{pl} *2.0* program must also be validated for combined load cases. The combined loading must also include the effects of shear loads on the plastic capacity of cross-sections. The inclusion of the shear loads on the plastic capacity of cross-sections will be required to conduct the study of members under bending and axial loads using transversal loads. Therefore, this chapter will validate the accuracy and reliability of R_{pl} *2.0* for combined loadings.

Interaction diagrams will be generated using R_{pl} *2.0* and shell finite elements models. The interaction diagrams obtained using these tools will be compared. Also, approximate analytical equations will be considered to generate interaction diagrams, thus providing additional confirmations of the results validity. Note however that the analytical equations are limited in their applicability and will may only be used for illustration purposes on specific cases.

4.1 – Parametric study parameters

To cover multiple cross-sections and loading scenarios, the studied cross-sections will be either doubly-symmetric or singly-symmetric I-beams. Also, numerical tests will be conducted on hot-rolled and welded cross-sections. The steel grade used for the numerical simulations has a Young's modulus E of 200 GPa and a yield strength f_y of 350 MPa. The material law, used in R_{pl} 2.0 and the FE shell models, is perfectly plastic, as shown in Figure 10. In R_{pl} 2.0, the ultimate strain ε_u has been set to 2%. Recall that the elastic strain limit of steel is 0.175%, which is much smaller than 2%.

Table 12 displays the studied cross-section geometries of this chapter.

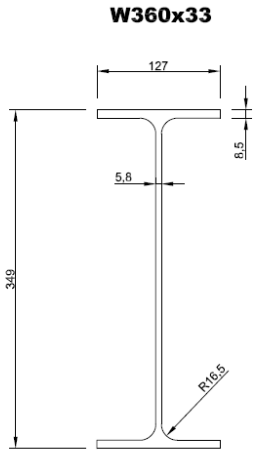

Figure 42: Hot-rolled W360x33

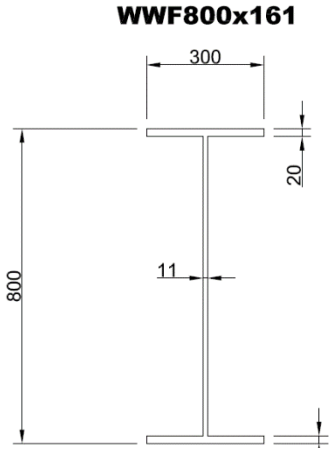

Figure 43: Welded WWF 800x161

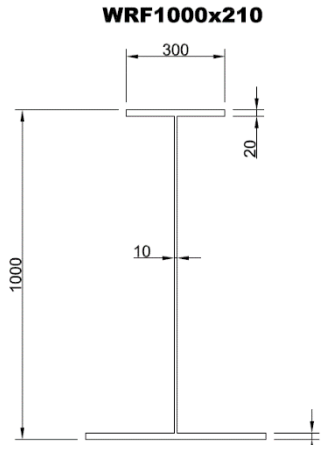

Figure 44: Welded WRF 1000x210

Table 12 – Studied doubly and singly-symmetric cross-sections dimensions

Dimensions [mm]	W360x33	WWF800x161	WRF1000x210
h	349	800	1000
b_{ft}	127	300	300
t_{ft}	8.5	20	20
b_{fb}	127	300	550
t_{fb}	8.5	20	20
w	5.8	11	10
r	16.5	-	-

Also, a variety of load combinations will be studied. The interaction diagrams will be calculated for the following load combinations:

- Axial load and major-axis bending moment ($N + M_z$);
- Major-axis and minor-axis bending moments ($M_z + M_y$);
- Axial load, major-axis and minor-axis bending moments ($N + M_z + M_y$);
- Major-axis shear load and major-axis bending moment ($V_y + M_z$).

In *R_{pl} 2.0*, the first three load combinations produce axial stresses only and the fourth produces a combination of axial and shear stresses on the cross-section fibers. For each interaction diagrams, the loading proportions will be varied to cover all the interaction spectrum.

When possible, the results will be compared to analytical equations provided by either the standards or by (Beaulieu et al., 2005). These analytical equations have been mostly developed for doubly-symmetric I-beams and a perfectly plastic material law.

4.1.1 – Plastic capacities of the studied cross-sections

The individual plastic capacities calculated using various methods will be compared to characterize the expected results variations. The plastic capacities will be calculated according to the catalog properties, the FE shell models and *R_{pl} 2.0*. Table 13 presents the calculated plastic capacities for a WWF800x161 and a WRF1000x210 cross-sections. The plastic capacities of the W360x33 have been detailed in the previous chapter and are recalled again here. The plastic capacities displayed in Table 13 will be used to calculate the

interaction diagrams. Each point of an interaction diagram represents a load combination, combining two or more internal forces.

Table 13 - WWF800x161 and WRF1000x210 plastic capacities

WWF800x161 (Welded)				
	N_p [kN]	M_{zp} [kN*m]	M_{yp} [kN*m]	V_{yp} [kN]
HSC	7175.0	2212.0	323.4	1733.8
Shell model	7153.7	2222.6	320.4	1706.0
Variation (*Shell - HSC)* [%]	-0.3	0.5	-0.9	-1.6
R_{pl}	7130.0	2192.5	316.5	1755.6
Variation (R_{pl} - *Shell)* [%]	-0.3	-1.4	-1.2	2.8
WRF1000x210 (Welded)				
HSC	9345.0	3503.2	695.3	1980.3
Shell model	9650.1	3545.8	689.5	2048.4
Variation (*Shell - HSC)* [%]	3.3	-1.2	-0.8	3.3
R_{pl}	9317.7	3507.4	692.9	1990.0
Variation (R_{pl} - *Shell)* [%]	-3.6	-1.1	0.5	-2.9
W360x33 (Hot-Rolled)				
Eq.(50)-(53)	1511.4	197.9	25.5	409.0
Shell model	1535.7	205.4	25.4	410.0
Variation (*Shell – Eq.)* [%]	-1.6	-3.8	0.6	-0.2
R_{pl}	1507.0	198.0	25.4	410.0
Variation (R_{pl} - *Shell)* [%]	1.9	3.6	0.0	0.0

4.2 – Axial load and major-axis bending moment ($N + M_z$)

The following plastic interaction diagrams present the interaction between axial load and major-axis bending moment. The axial load may be applied as a compression or tension load as both give similar results in the plastic capacity calculations of doubly-symmetric cross-sections. For mono-symmetric cross-sections, the axial load direction does have an influence on the results. Figure 45 presents the interaction diagrams obtained for a W800x161 cross-section.

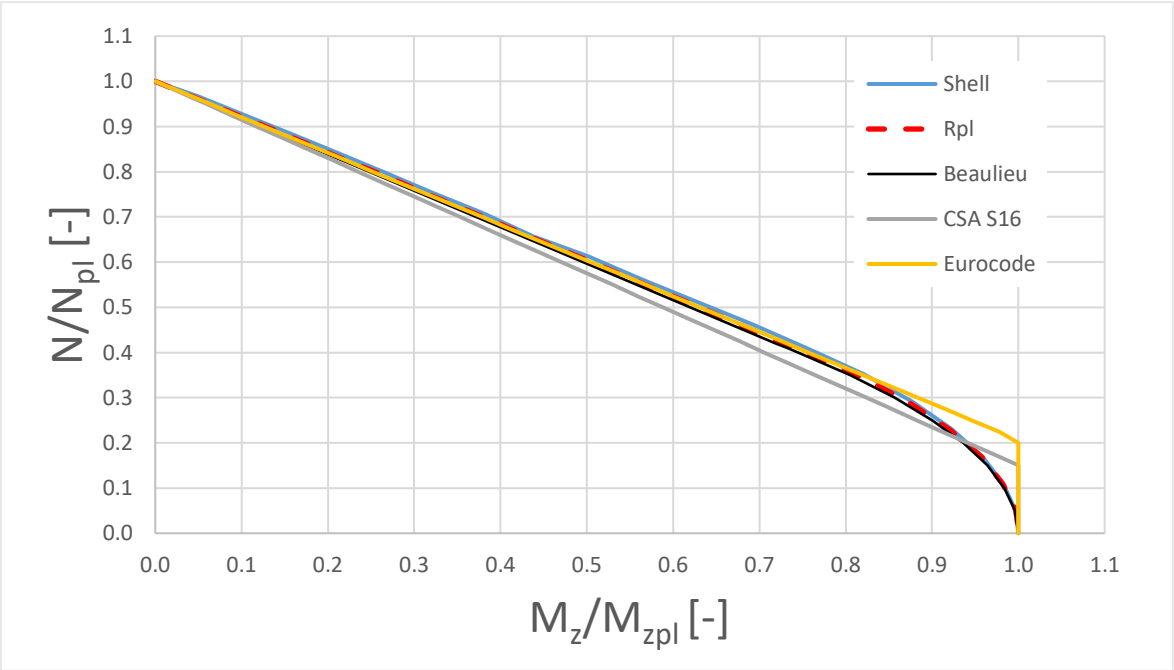

Figure 45 - N +M_z interaction diagrams for a W800x161 cross-section

Figure 45 shows a strong correlation of the plastic capacities obtained with all methods. Contrarily to the formulation proposed in (Beaulieu et al., 2005), the interaction formulas proposed in the CSA and Eurocode standards use a linear interaction formula. Figure 45 also shows that for both the CSA and Eurocode standards, the plastic major-axis bending capacity is not reduced by the axial loading until the axial loading reaches respectively 15% and 20% of the axial loadplastic capacity of the cross-section. Although, the interaction curves obtained using R_{pl}, FE shell models and other references clearly show that the interaction between the axial loading and the bending moments occurs much sooner. The standards interaction curves, for high bending moments load ratios, over-estimates the cross-section plastic capacity. For a bending moment load ratio of 0.98, the axial load ratio using R_{pl} is 0.11 comparatively to 0.17 for the CSA and 0.22 for the Eurocode standards. The axial load ratio from the CSA standard is approximately 54% higher than R_{pl} and the axial load ratio from the Eurocode standard is approximately 100% higher than R_{pl}. Apart from the high bending moment ratio region, the CSA interaction curve provides safe sided results. Figure 46 presents the interaction diagrams obtained for the W360x33 cross-section showing a strong concordance of the plastic capacities results obtained with all methods.

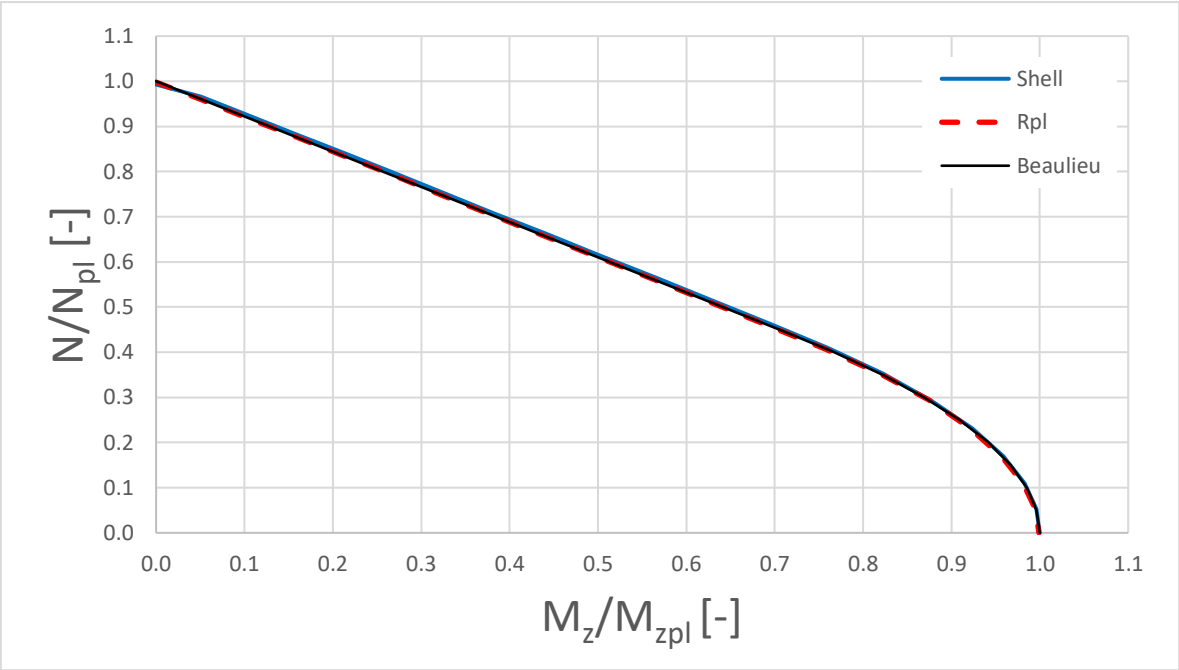

Figure 46 - N + M_z interaction diagrams for a W360x33 cross-section

For the general case of mono-symmetric cross-sections under pure major-axis bending, the plastic capacity remains identical for either a positive or negative bending moment. However, for mono-symmetric cross-sections under axial and bending loads, the axial loads influence the plastic bending capacities. For a mono-symmetric I-beam, the different sizes of the top and bottom flanges influence the plastic bending capacities. A smaller flange signifies a smaller capacity to store stresses and that capacity may be exhausted faster than the larger flange. As the cross-section extremities gradually yield, the plastic neutral axis shifts toward the larger flange, as shown in Figure 47. Figure 47 presents the von Mises stresses of the cross-section.

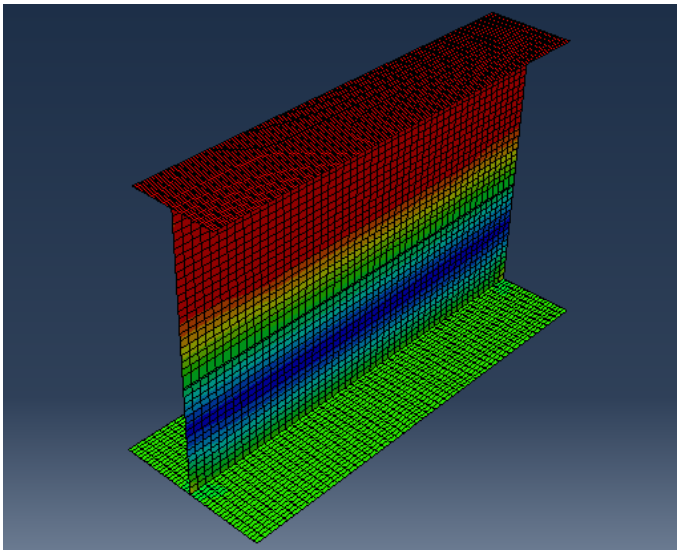

Figure 47 - Shift of the plastic neutral axis toward the larger flange

As the cross-section yields and the stresses reach their plastic limit f_y, the shift of the neutral axis is required to keep the global axial load equilibrium. The application of an external axial load may increase or decrease the axial stresses on the smaller flange, thus either increasing or decreasing the axial stresses on that flange. Therefore, the axial loading may have a beneficial or detrimental effect on the plastic capacities, depending on the direction of internal axial stresses and strains of each fiber. Although, the beneficial effects are limited and may only be observed for high bending moment ratios and low axial load ratios. Otherwise, the addition of axial load is detrimental to the plastic bending capacities of cross-sections. The direction or sign of the stresses and strains depends on the direction of application of the axial or bending loads. The following interaction diagrams will be computed for a tension load and positive and negative bending moments. Figure 48 presents the interaction diagrams obtained for the singly-symmetric welded cross-section WRF1000x210 for positive and negative bending loads.

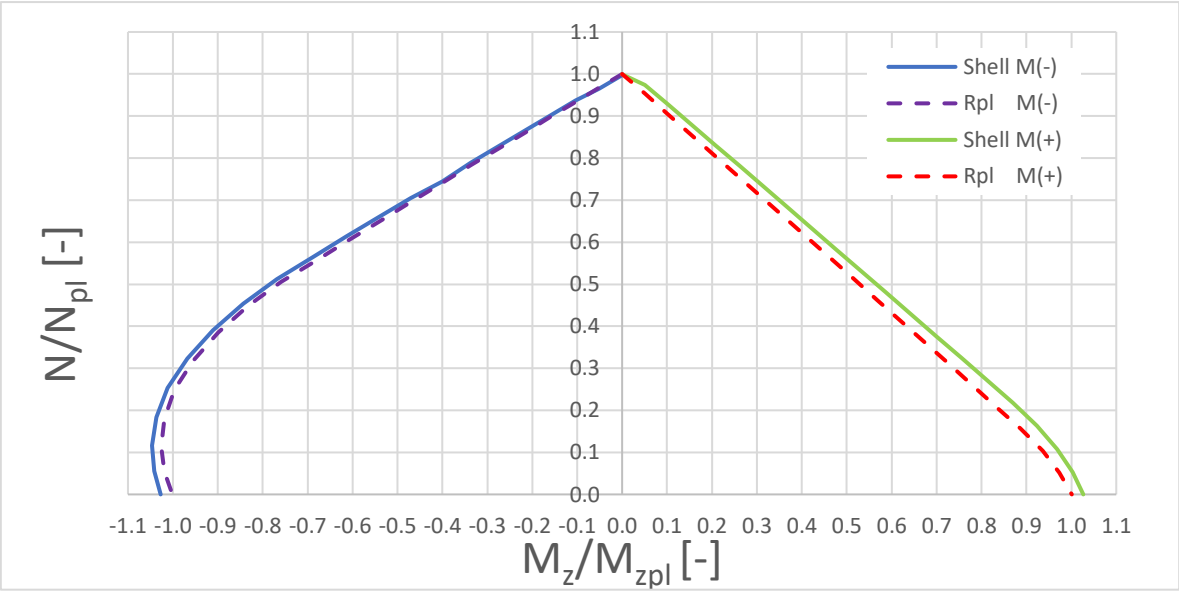

Figure 48 - N +M_z interaction diagrams for a WRF1000x210 cross-section

Figure 48 displays the effect of an axial load on the plastic interaction diagrams of a mono-symmetric cross-section for positive and negative bending moments. The axial load produces positives strains and stresses (tension). The positive bending moment generates compression in the bottom flange and tension in the top flange. The negative bending moment generates tension in the bottom flange and compression in the top flange. The bottom flange is the largest flange, as shown in Figure 44.

Figure 47 shows that the interaction curves, for positive and negative bending moments, are not symmetric. The negative bending moment interaction diagram shows that, until a certain level, the tension load allows to exceed the pure plastic bending moment capacity of the cross-section(Villette, 2004). The cross-section being mono-symmetric, the strains and stresses along the cross-section height are non-symmetric. The positive strains and stresses, generated by the tension load, counteracts the negative stress and stresses (compression) of the cross-section top flange. The yielding of the top flange is delayed and, by extension, delays the shift of the plastic neutral axis.

Figure 48 demonstrates that plastic capacities, computed using the shell finite elements, are slightly over-evaluated. The shell models being represented in three-dimensions, plasticity spreads along the member length. Therefore, the shell elements do not yield simultaneously,

and the remaining elastic shells bring additional rigidity to the model. Hence, the calculated resistances are slightly higher.

4.3 – Major-axis and minor-axis bending moments (M_z + M_y)

Figure 49 presents the interaction diagrams between major-axis and minor-axis bending obtained for a W800x161 cross-section.

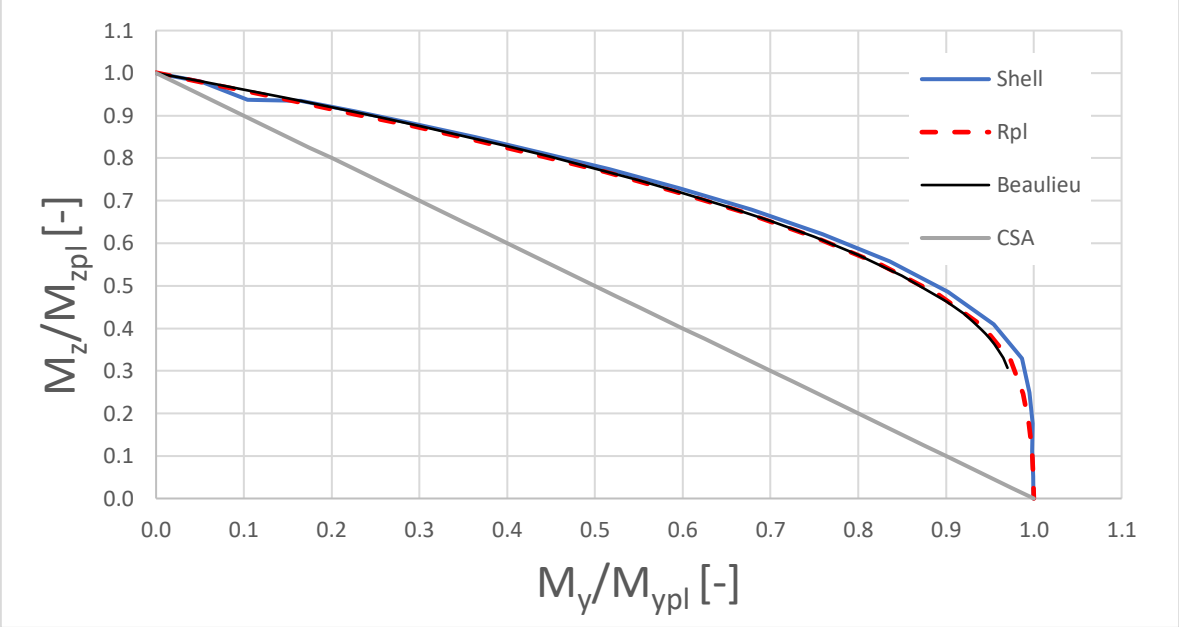

Figure 49 – M_z +M_y interaction diagrams for a W800x161 cross-section

Figure 49 shows a strong concordance of the shell model results, the R_{pl} results and the results obtained in (Beaulieu et al., 2005). Figure 49 also displays a limitation in the analytical equations provided by (Beaulieu et al., 2005). The equations have been constructed to calculate a reduced major-axis bending moment plastic capacity caused by a minor-axis bending moment. Hence, the equations do not cover interaction points where minor-axis bending governs and are thus limited in their use. In addition to the equations provided by (Beaulieu et al., 2005), the plastic capacity of a cross-section may be calculated using static plastic distribution theorems.

The equations provided by the standards are safe-sided approximations. The CSA linear interaction may be considered overly-conservartive. For a major-axis bending moment load ratio of 0.5, the minor-axis bending moment load ratio using R_{pl} is 0.89 comparatively to 0.5 for the CSA standard. The minor-axis bending moment load ratio from the CSA standard is

almost half the ratio calculated using R_{pl} and the FE shell models. Figure 50 presents the interaction diagrams obtained for a W360x33 cross-section.

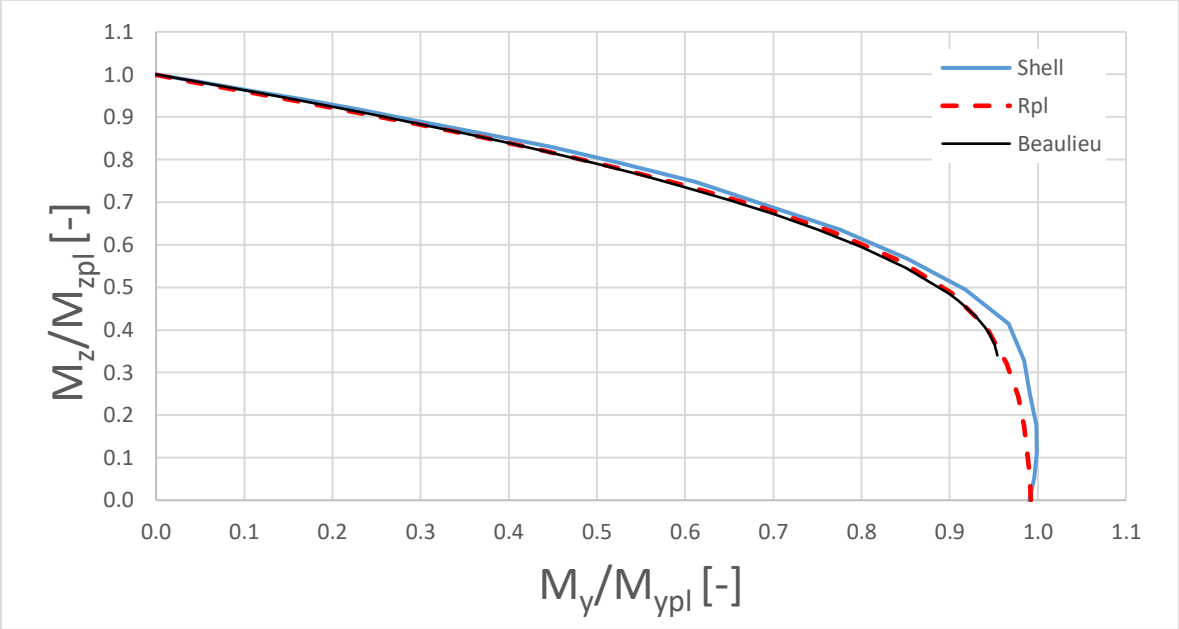

Figure 50 - M_z +M_y interaction diagrams for a W360x33 cross-section

Figure 50 presents the interaction diagrams obtained for a W360x33 cross-section and shows a fairly good agreement of the results. The shell element results tend to slightly overestimate the cross-section plastic capacities for load combinations where minor-axis bending is dominant. Although, the interaction diagram obtained using (Beaulieu et al. 2005) follows very well the interaction diagram obtained using R_{pl}.

Figure 51 presents the interaction diagrams obtained for a WRF1000x210 cross-section. For biaxial bending without any axial load, the sign of the bending moments does not influence the results, therefore only one interaction diagram is displayed.

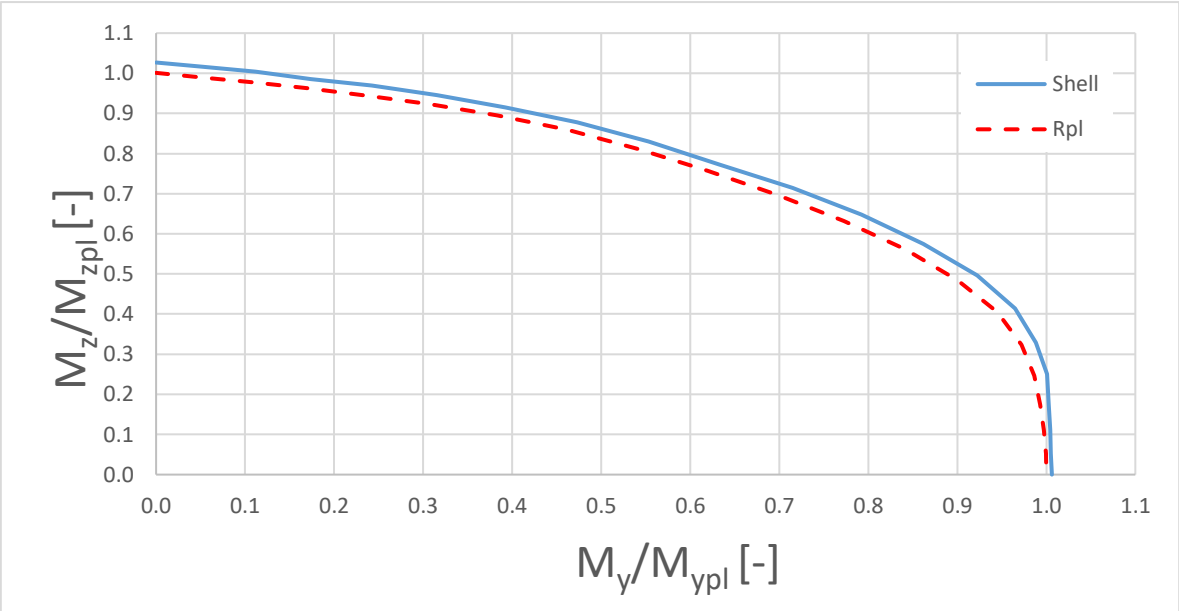

Figure 51 - M_z +M_y interaction diagrams for a WRF1000x210 cross-section

Again, Figure 51 shows that the shell element results tend to slightly overestimate the plastic capacities of the cross-section. Analytical equations considered here do not cover mono-symmetric cross-sections.

4.4 – Axial load, major-axis and minor-axis bending moments ($N + M_z + M_y$)

In this section, interaction diagrams will be generated for axial, major-axis and minor-axis bending moments. $N + M_z + M_y$ interaction diagrams are three-dimensionnal, where the vertical axis represents the axial load ratios and both other axes represent the major-axis and minor-axis bending moment ratios. Generating full three-dimensionnal interaction diagrams is quite a complex. For that reason, two-dimensionnal interaction diagrams will be presented. The interaction curves will display the interaction results for various ratios of the major-axis and minor-axis bending moments for a given initial axial load intensity (0.2, 0.5 or 0.8 the axial plastic capacity of the cross-section).

To properly generate $N + M_z + M_y$ interaction diagrams with R_{pl} and FE shell models, an iterative method must be implemented. The objective is to calculate the plastic capacity multiplier for a constant axial load intensity. The R_{pl} program has included such an iterative method. Because the load multipler in R_{pl} increments the internal loads radially, the initial axial load applied to the cross-section multiplied by the final plastic load capacity mutiplier

R_{pl} may not correspond to the desired final load intensities of either 0.2, 0.5 or 0.8 the axial plastic capacity of the cross-section. Therefore, an iterative process compares the desired axial load intensity to the calculated axial load carried by the cross-section and ajusts the initial axial load ratio if convergence is not reached. Because of the iterative process, the final axial load intensity is within a small tolerance of the desired constant axial load intensities of 0.2, 0.5 or 0.8 the axial load plastic capacity. Although, this iterative process could not be implemented within the *ABAQUS* procedure and performing the iterations manually would be a time-consuming and imprecise process. Instead, the following interaction diagrams will be calculated using a simplified method.

The simplified method consists of applying simultaneously the $N + M_z + M_y$ loads. Their intensity will be increased radially by the R_{pl} and the FE shell models until the plastic capacity multiplier is found. This simplified method will provide radial plastic capacity values, where the final axial load carried by the cross-section may not correspond to the desired axial load intensities of 0.2, 0.5 or 0.8 the axial plastic capacity of the cross-section. For each axial load intensities of 0.2, 0.5 or 0.8, the major-axis and minor-axis bending moments are varied.

Figure 52 presents the interaction diagrams obtained for a W800x161 cross-section and shows a relatively good concordance of the results obtained with the shell model plastic capacities.

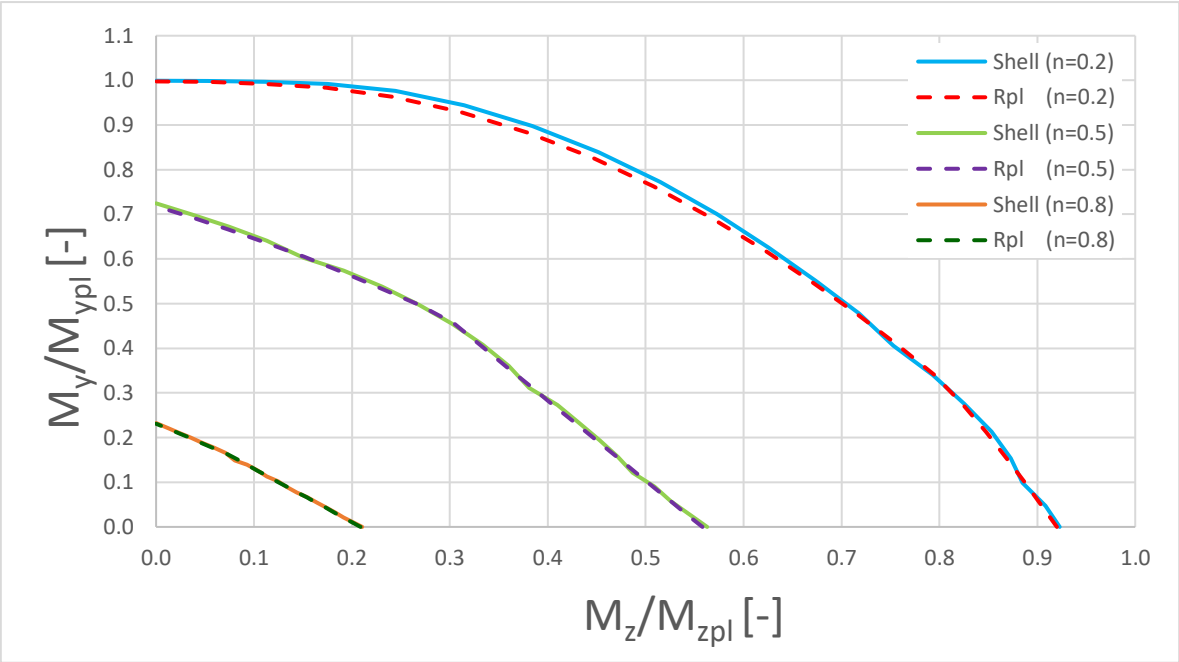

Figure 52 - N + M_z +M_y interaction diagrams for various axial load intensities for a W800x161 cross-section

However, R_{pl} tends to slightly underestimate the plastic resistances for axial load ratios of ($n = 0.2$). Yet again, the FE shell model plastic capacities may be over-estimated because of the spread of plasticity along the member length. Also, an interesting fact may be noted. The axial load ($n = 0.2$) inhibits the cross-section to reach the full plastic major-axis bending moment, contrarily to the minor-axis bending resistance. For ($n = 0.2$), the major-axis bending moment reaches approximately 90% of the full cross-section major-axis bending capacity. Figure 53 presents the interaction diagrams obtained for a W360x33 cross-section.

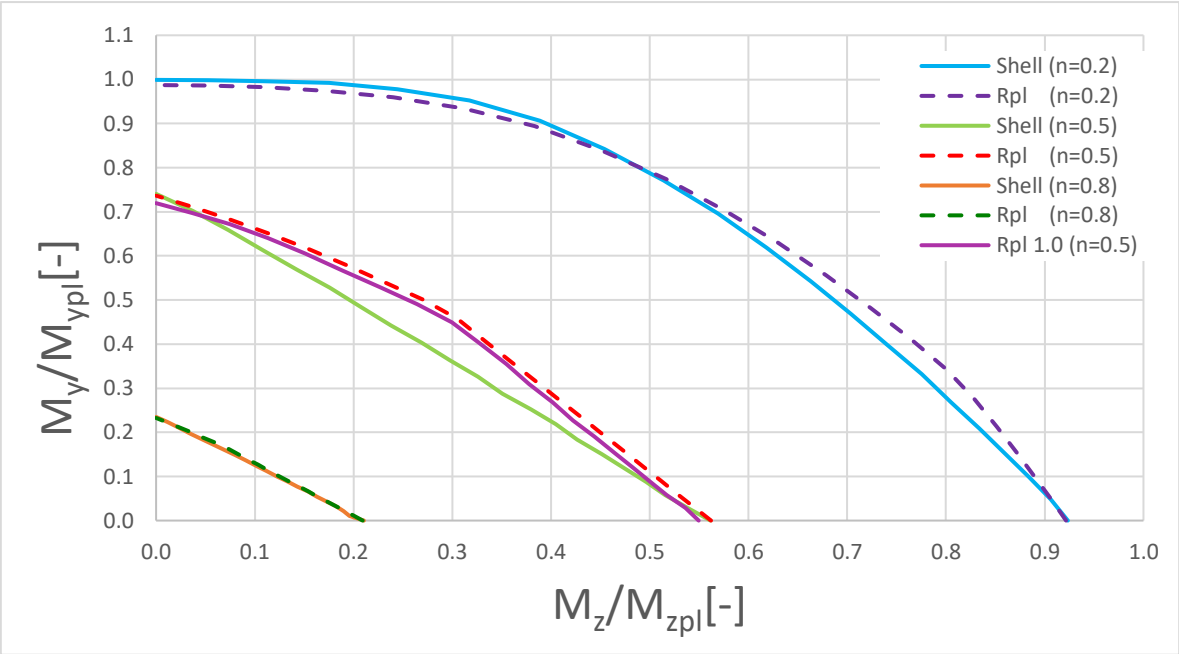

Figure 53 - N + M_z +M_y interaction diagrams for various axial load intensities for a W360x33 cross-section

Figure 53 shows a good concordance of the results obtained for axial load ratios of (*n = 0.2*) and (*n = 0.8*). For (*n = 0.2*), R_{pl} plastic capacity values for high major-axis bending moment ratios are higher than the FE shell models and the plastic capacity values for high minor-axis bending moment ratios are slightly lower than the FE shell models.

However, the interaction diagrams of R_{pl} and the FE shell models for (*n = 0.5*) do not coincide. The interaction curve from the FE shell models is linear and provides lower plastic capacity results than R_{pl}. For that reason, an additionnal interaction curve has been calculated using the initial version of R_{pl} 1.0. The calculated interaction curve using R_{pl} 1.0 shows a good concordance and a similar pattern with the interaction curve calculated using R_{pl} 2.0, thus validating the interaction curve calculated using R_{pl} 2.0. Further investigations of this particular FE shell model should be considered to explain the differences between the interaction curves.

Figure 54 presents the interaction diagrams obtained for a WRF1000x210. Because the cross-section is mono-symmetric, the interaction diagrams have been generated for both positive and negative bending moments.

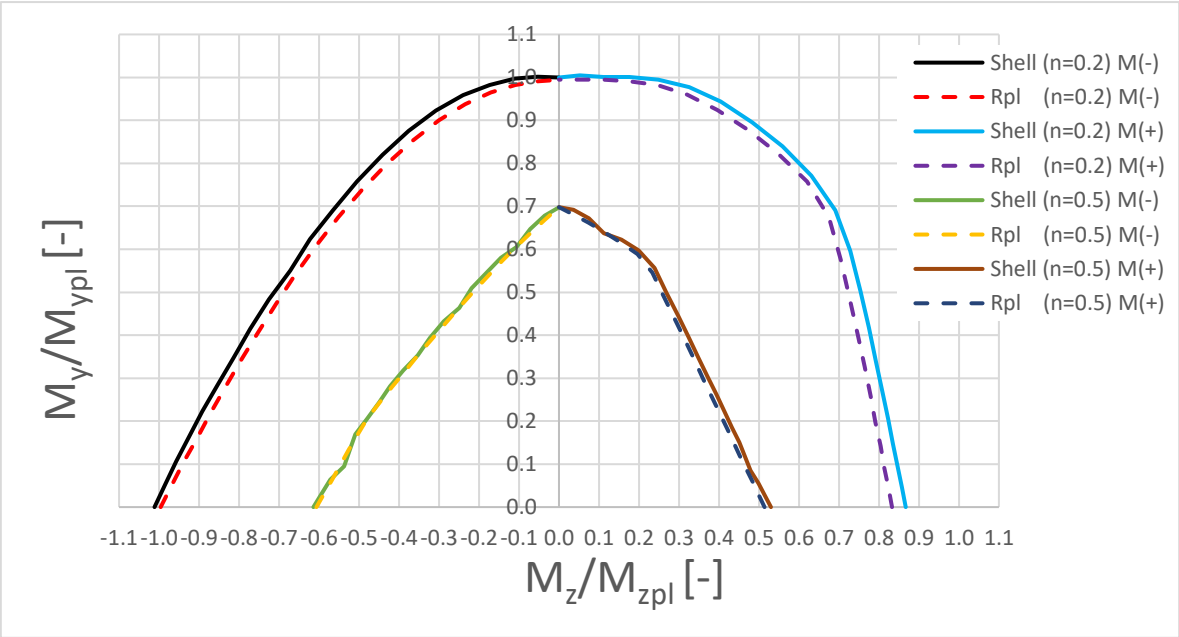

Figure 54 - N + M_z +M_y interaction diagrams for various axial load intensities for a WRF1000x210 cross-section

The axial ratio of (*n = 0.8*) has been disregarded as the biaxial bedning interaction influence is less significant. Figure 54 shows the unsymmetric behavior of the cross-section, depending on the bending moment loading direction. For (*n = 0.2*), the FE shell model results tend to over-estimate the plastic capacities of the cross-section, compared to R_{pl}. Figure 54 also displays that the full plastic major-axis and minor-axis bending capacities are reached for the axial load ratio of (*n = 0.2*) and a negative major-axis bending moment. For that specific case, the axial load does not seem to influence the plastic capacity of the cross-section as both bending moments reached their ultimate plastic capacities. For (*n = 0.2*) and a positive major-axis bending moment, the cross-section is limited to approximately 80% of the pure plastic bending capacity of the cross-section.

For (*n = 0.5*), either for a positive or negative bending moment, the biaxial bending plastic capacities are reduced by the axial loading. The minor-axis bending plastic capacity is limited to approximately 70% and the major-axis bending plastic capacities to approximately 50% for a positive bending moment and approximately 60% for a negative bending moment.

4.5 – Major-axis shear load and major-axis bending moment (V_y + M_z)

The interaction diagrams in this section have been calculated for the vertical shear and major-axis bending moment. In addition to the interaction diagrams calculated using shell models,

CSA and Eurocode interaction diagrams will be presented. Figure 55 presents the interaction diagrams obtained for a W800x161 cross-section.

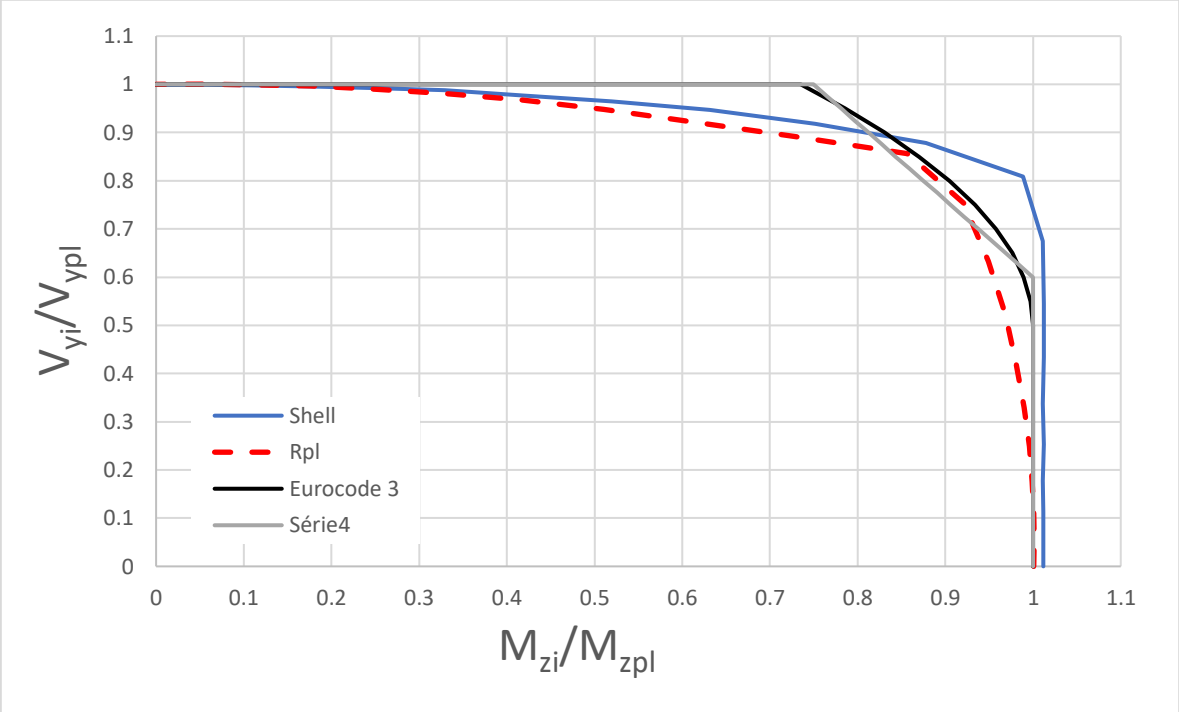

Figure 55 - Mz +Vy interaction diagrams for a W800x161 cross-section

Figure 55 shows a good agreement between the shell simulations, R_{pl} and the Eurocode. Although, some key differences can be observed. As previously stated, Eurocode 3 neglects any bending moment resistance reduction before the shear load is greater than 50% of the shear plastic capacity of the cross-section. The CSA standard neglects any interaction before a shear load that is greater than 60% of the shear plastic capacity of the cross-section. Results from the R_{pl} tool show that the interaction between major-axis bending and shear begins before the prescribed limit of the CSA and Eurocode standards, around a shear load of 20% of the shear plastic capacity of the cross-section. Conversely, the interaction diagram from the FE shell model is seen to begin only at around 70% of the plastic shear capacity of the cross-section.

Figure 55 shows that the shear plastic resistance defined by the Eurocode and CSA equations is not reduced until the bending moment is greater than 75% of the plastic bending capacity. Both the CSA and Euroce interation curves are similar although the CSA standard consider a simplified linear interaction. Both R_{pl} and the shell model show an interaction for bending

moment ratios under 75%. For a shear load ratio of 60%, the R_{pl} moment resistance is reduced by approximatively 4% compared to the Eurocode at the limit point and 5% compared to the CSA standard. For a major-axis bending load ratio of 75%, the R_{pl} shear resistance is reduced by approximatively 12% compared to the CSA standard.

For predominant shear loads, both the R_{pl} tool and the finite element simulations converge toward the plastic limit defined from the Eurocode standard. Figure 56 presents the interaction diagrams obtained for a W360x33 cross-section.

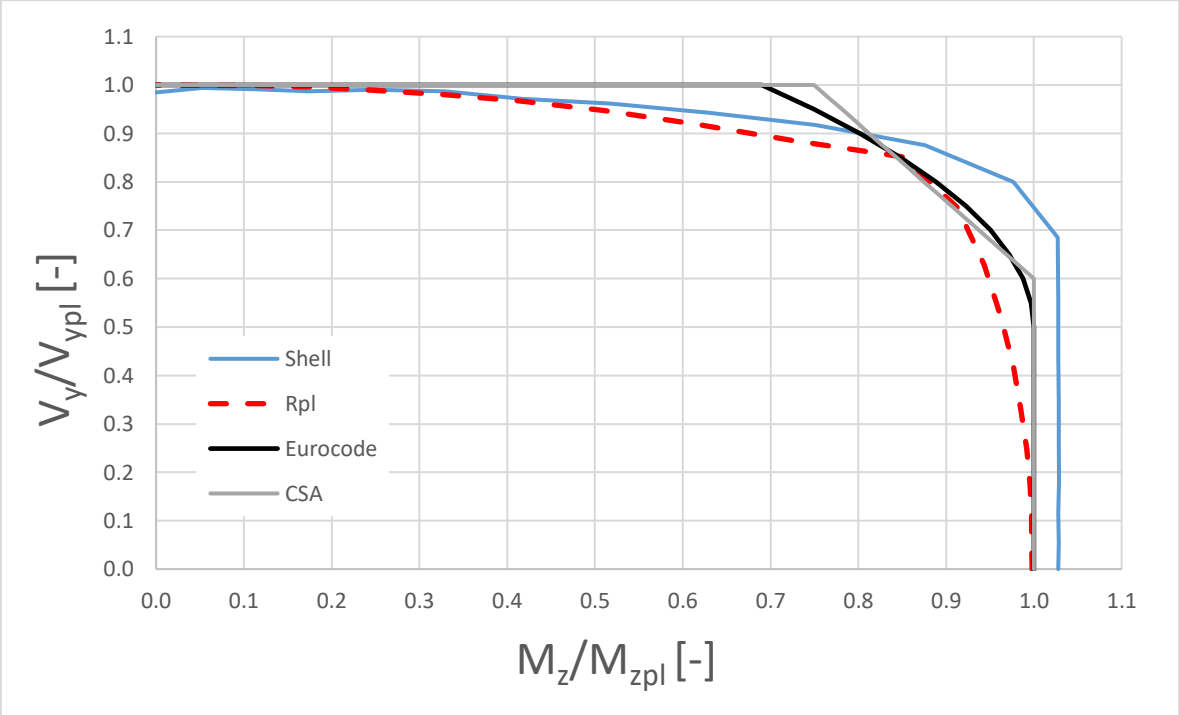

Figure 56 - Mz +Vy interaction diagrams for a W360x33 cross-section

Results displayed in Figure 56 follows the same pattern as the W800x161 cross-section. Although, the shear capacity for the Eurocode is reduced when 70% of the major-axis bending load ratio is reached, compared to approximately 75% in Figure 55.

The Eurocode provisions for mono-symmetric sections use a different approach than for doubly-symmetric I-sections. The yield limit f_y is reduced in proportion of the shear loading. Similar to previous provisions, interaction between bending and shear loading is only considered when the shear load is greater than 50% of the shear plastic capacity of the cross-

section. Figure 57 presents the interaction diagrams obtained for a WRF1000x210 cross-section.

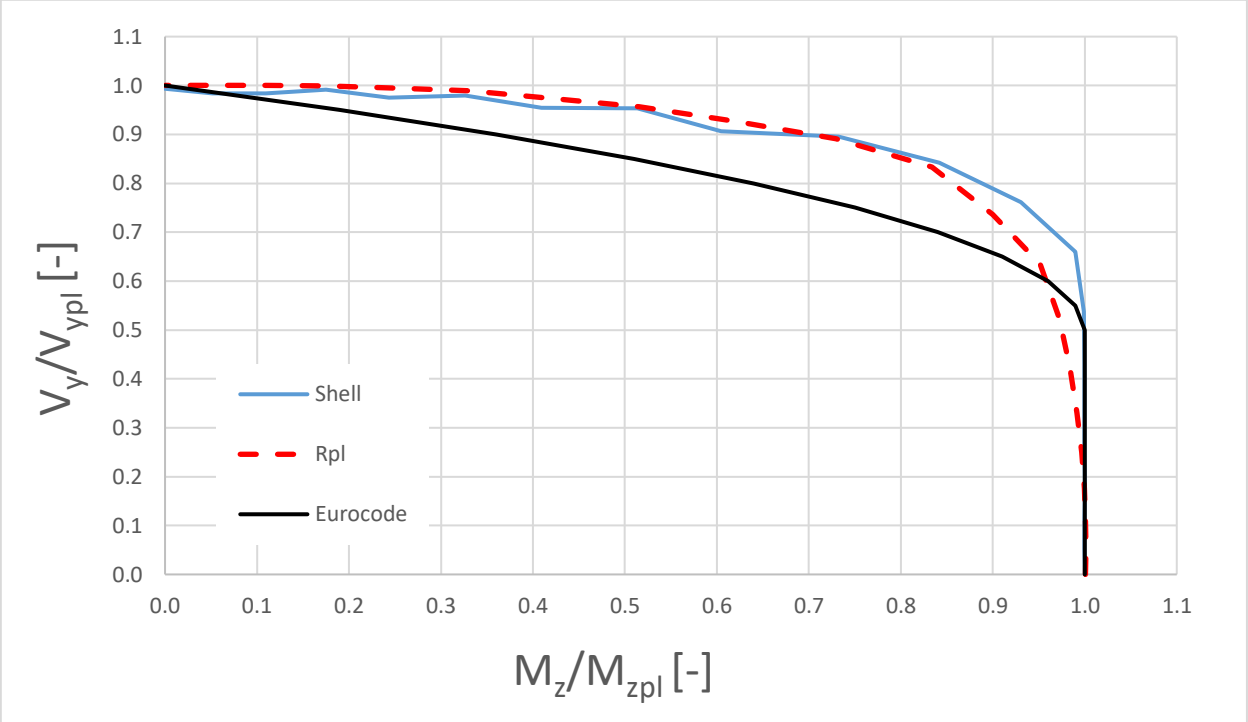

Figure 57 - Mz +Vy interaction diagrams for a WRF1000x210 cross-section

The R_{pl} and the shell model interaction curves are in good agreement. Yet, Figure 57 shows non-negligeable differences between the interaction diagram results. The R_{pl} and the shell model interaction curves provide higher estimations of the plastic capacities compared to the Eurocode results. Because the following chapter will work on doubly-symmetric cross-sections, the variation in the results will not be studied in detail. Also, further investigations could address the lack of smoothness of the FE shell model interaction curve.

In conclusion, the interaction diagrams presented throughout this chapter validate the accuracy of R_{pl} *2.0* for combined load cases. In general, a good agreement of the results from the analytical, the FE shell model and the R_{pl} results can be observed. Also, the interaction curves for the W800x161 and W360x33 cross-sections validated the use of R_{pl} for combined loading including shear loads. With R_{pl} *2.0* validated, the study on the effect of transversal shear forces on the overall resistance of members in tension and bending will follow.

Chapter 5 – Study of members in bending and tension

The previous chapters were mainly focused on validating the R_{pl} *2.0* program for the plastic analysis of cross-sections under single and combined loading cases. Therefore, previous chapters were only focused on the resistance of members at the cross-section level. This section will now be considering the global resistance of members, thus expanding the scope of this study. Specifically, the global resistance of members under bending and tension will be studied. Such loading case may arise for members in tension, such as bracings, with eccentric connections. The connection eccentricities may generate bending moments at both member extremities. From the interaction diagrams presented in previous chapters, it is known that an axial load has a detrimental effect on the plastic capacity of a member in bending. In rare cases, where the cross-section is mono-symmetric and the axial load ratio is small, the plastic bending capacity of the cross-section is slightly increased. Although, for slender members, a tension load may have a beneficial effect on the lateral torsional buckling resistance of the member as it may delay the buckling of the compression flange.

The subject of the resistance and stability of members in bending and tension has been studied in two previous master theses by João Tomás Mello e Silva (Silva, 2013) and Vincent Epiney (Epiney, 2015). The studies considered various parameters such as multiple cross-sections, member lengths, steel grades, bending moment distributions, tensile force intensities and load application positions. The work of Silva, with approximately 2000 numerical results, confirmed the beneficial effect of tension forces on the global bending resistances of slender members. The bending moments were applied by concentrated moments at the member ends.

Epiney (2015) studied, with a similar number of numerical tests, the beneficial effect of tensile forces, although, the bending internal forces were induced by transversal loads. Epiney also reprocessed Silva (2013) results strictly in accordance with the O.I.C. concept. As mentioned in chapter 1, the O.I.C. concept generates resistance curves using i) the lambda factor λ, which represents the slenderness of the element and ii) the khi factor χ, which defines the relation between the plastic resistance and the element ultimate failure. By applying the bending forces with transversal loads, shear internal forces are induced in the member, most notably near the supports. Those shear internal forces were not considered in the plastic cross-section capacity calculations in previous studies due to a lack of tools. The tools available at

the time could not calculate the plastic capacity of the complex axial load, major-axis bending and major-axis shear load interaction.

This limitation is now removed with the R_{pl} *2.0* tool. R_{pl} *2.0* handles, in addition of axial and bending loads, major-axis and minor-axis shear loads in the plastic capacity calculations. The objective will be to determine the effect of that simplification on the results and to recalculate the member resistances, under the O.I.C. format, of each numerical simulation. Therefore, this study aims at completing and correcting the results obtained in those previous theses. Further details on how this study will improve and correct the results will be given later. The next section will briefly describe the models and resistance equations used for the numerical simulations.

5.1 – Models description and resistance equations

The first thesis, done by Silva (2013), studied a simply supported beam with concentrated bending moments at the member ends. The tension loading was applied by concentrated axial forces also applied at the member ends. Figure 58 depicts the general representation of the studied system. As described in the introduction of this chapter, the end bending moments may represent the bending moments generated by the connection eccentricities and the tension in the member.

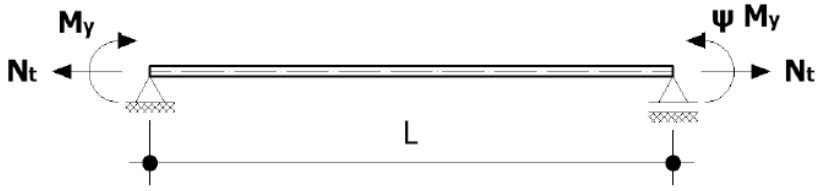

Figure 58 - Beam in tension and bending with concentrated bending moments (Silva, 2013)

From the general model shown above, five different bending moment distributions were studied. The distributions were characterized by the factor Ψ, as depicted in Figure 59. The Ψ factor is the ratio of the bending moment intensities of both extremities.

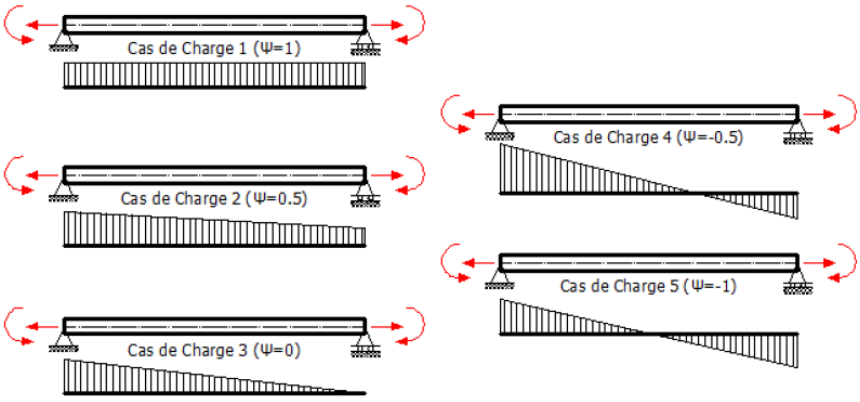

Figure 59 – Bending moment distributions for various factor ψ (Epiney, 2015)

The main objective of both theses was to generate buckling curves representing the overall resistance of members subjected to bending and tension. Although, the generation of the buckling curves were done slightly differently. Equations (55) and (56) present the method used by Silva (2013) to calculate the member λ_{LT} and χ_{LT}.

$$\lambda_{LT} = \sqrt{\frac{M_{pl,Rk}}{M_{cr}}} \tag{55}$$

$$\chi_{LT} = \frac{M_u}{M_{pl,Rk}} \tag{56}$$

where $M_{pl,rk}$ is the cross-section plastic capacity under pure major-axis bending, M_u the ultimate member capacity calculated using 3D shell elements models and M_{cr} the critical bending moment capacity. Silva (2013) developed analytical equations to calculate the critical bending moments under tension forces that were virtually exact. Although, it can be observed, from the equations above, that the tension forces were omitted in the calculations of the plastic bending moments $M_{pl.Rk}$. Because of that, this formulation cannot be applied to general loading cases as the plastic cross-section resistance $M_{pl,Rk}$ is calculated for pure bending only. Because the work of Silva (2013) was focused on members where instabilities usually governed the overall resistance of the members, this formulation did not interfere in large extent with the validity of the results. Although, it limited his study solely on the instability portion of the resistance curve. Therefore, the plastic cross-section resistance had little to no influence on the results, hence the λ_{LT} and χ_{LT} notation.

The second thesis, elaborated by Epiney (2015), used the same general model except that the bending moments were applied using transversal loads, as shown in Figure 60. The vertically distributed loads are constant along the length of the members. In total, five load cases were studied, each having some particularities. Load cases 1 to 3 are almost identical, except that the uniform loading is applied at various position along the cross-section height. For load case 1 to 3, the uniform load is applied respectively at the top, at the middle and at the bottom of the cross-section. The load application position has a direct influence on the member stability, thus the global resistance of the member. Loads applied higher than the cross-section center of gravity favors the lateral torsional buckling of the member. Loads applied lower than the center of gravity generally helps the stability of the member. Those cases are aimed at evaluating the beneficial or detrimental effect of the load application point on the ultimate and critical resistance. For load cases 4 and 5, additional concentrated bending moments are applied to the members ends. Also, for load case 4, the uniform load is applied at the top of the cross-section and for load case 5, at the middle.

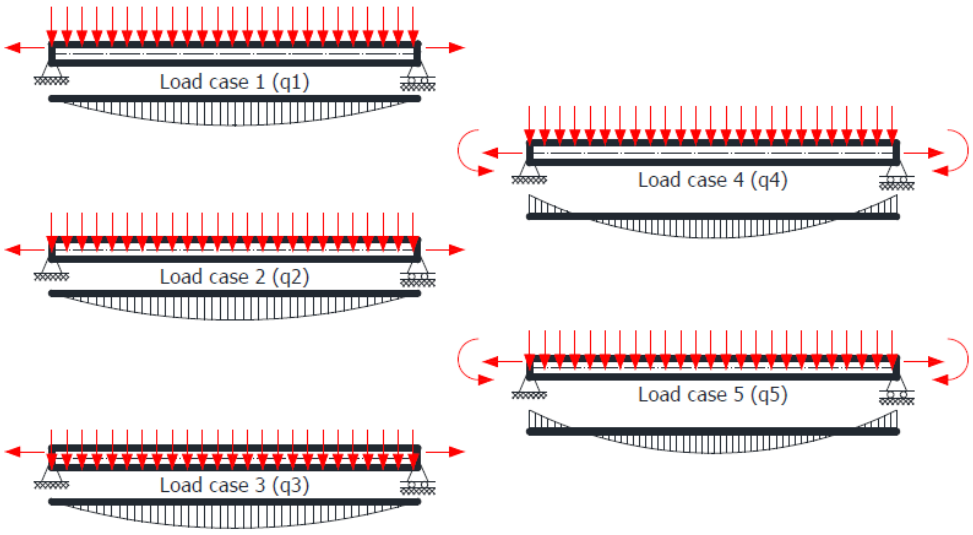

Figure 60 - Bending moment distributions for various load cases (Epiney, 2015)

Epiney (2015) generalized the formulation used to calculate the ultimate resistance of members under bending and tension. By adapting the equations presented above according to the O.I.C. concept, cases with low slenderness, characterized by the pure cross-section resistance, may be covered. The new formulation could treat the ultimate resistance of the member due to instabilities and the ultimate resistance of the member governed by the cross-

section capacities by considering the axial and bending loads effects on the member plastic capacities. By doing so, the formulation, as shown in equations (57) and (58), was conform to the O.I.C. concept.

$$\lambda_{MB} = \sqrt{\frac{M_{pl,N,Rk}}{M_{cr}}} \tag{57}$$

$$\chi_{MB} = \frac{M_u}{M_{pl,N,Rk}} \tag{58}$$

From the equations above, it can be observed that the axial force is now considered in the plastic bending moment $M_{pl.N,Rk}$ calculations. With this addition, the resistance curves may accurately represent the entire response of the member behavior. By calculating the values of M_u using 3D finite element models, the effect of the transversal loads on the ultimate resistance are directly captured. Therefore, M_u values capture the effect of axial, bending and shear loads while $M_{pl.N,Rk}$ values only capture the effect of axial and bending loads. Although improved, equations (57) and (58) remain incomplete because the shear loads are not included in plastic capacity calculations and that creates a mismatch in the equation parameters. This problem will be addressed, and further details will be given later in this chapter.

As Silva (2013) loading methods generally did not apply extensive shear loads, and that the work of Epiney (2015) is readily inline with the O.I.C. concept, the work of this study will be based on the thesis of Epiney.

As mentioned above, the internal bending forces were mainly applied by uniform transverse loads. The uniform transverse loads produce flexure and vertical shear internal forces. A large quantity of results, in Epiney (2015), were challenging. Figure 61 displays the results obtained, for load cases q1 to q5. That figure shows many numerical results below the general pattern of the buckling curves (see ellipse). The omission of the shear loads, in the plastic capacity analysis of the cross-sections, may be the cause of the discrepancies.

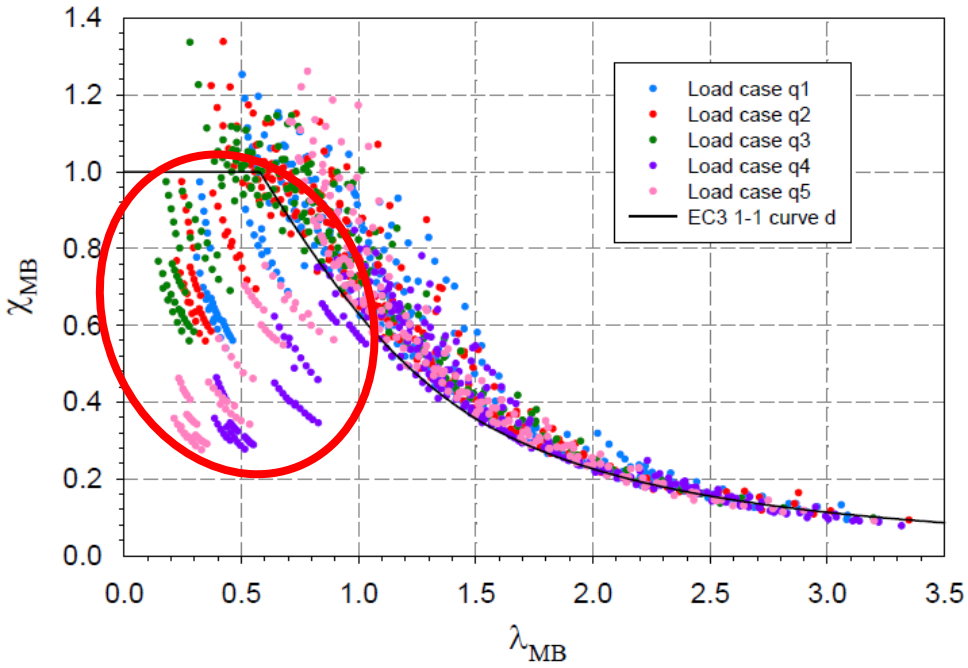

Figure 61 – Buckling curves obtained by Epiney (2015) *for load cases q1 to q5*

With the problematic described above, this work will study and verify the influence of the shear internal force on the buckling curves of members under transversal loads. Using the developed R_{pl} *2.0* tool, the cross-section plastic capacities under combined loads will be calculated for members undergoing bending, shear and tension forces.

Before launching numerous numerical calculations, the details of the parametric study are described, and the underlying causes of the results situated below the curve will be explored. Also, a new formulation for equations (57) and (58) will be suggested to correct the challenging results. Then, the new set of results will be presented and discussed. The results will be studied to confirm or deny the effect of the transverse shear on the results.

5.2 – O.I.C. resistance curve formulation including shear loads

As mentioned previously, a new formulation is required to calculate the resistance curves of members with shear internal forces. As explained in section 1.4, the ultimate resistance of a member may be governed by global or local instabilities, ultimate global resistance, or a combination of both as shown in equations (57) and (58). Although conform to the O.I.C. philosophy, these equations will be generalized to properly consider all internal forces. The generality of the O.I.C. formulation easily allows the shear internal force effects to be included in the resistance curves formulation as shown in equations (59) and (60).

$$\lambda_G = \sqrt{\frac{R_{pl(N,M,V)}}{R_{cr(N,M,V)}}} \tag{59}$$

$$\chi_G = \frac{R_{u(N,M,V)}}{R_{pl(N,M,V)}} \tag{60}$$

where $R_{pl(N,M,V)}$ is the cross-section plastic capacity load multiplier for axial, bending and shear loads, $R_{u(N,M,V)}$ the global ultimate resistance capacity load multiplier from FE shell calculations and $R_{cr(N,M,V)}$ the critical instability load multiplier. In this context, N represent the tension force (N_t), M the major-axis bending (M_z) and V the major-axis shear force (V_y). Comparatively to previous formulations, equations (59) and (60) are presented in terms of load multipliers instead of specific load resistances or capacities. Therefore, this formulation is particularly well suited to treat combined load cases. Although, the tools used to calculate each load multipliers must similarly incorporate all types of loads in the load combinations. Because no cross-section local instabilities are considered in this study, the λ_G and χ_G notation will be used, as per Figure 2.

5.2.1 – Calculation of the critical stability load multipliers (R_{cr})

The critical bending stability load multipliers R_{cr} were calculated in previous thesis Epiney (2015). The tool LTBeamN was used. The LTBeamN tool has the capability of calculating the critical member stability factor R_{cr} for load combinations that include axial and bending loads. The bending loads can be applied as transversal loads, as required by this study. Also, the tool allows to modify the load application point of the transversal loads, as required by cases q1, q3 and q4. Although the values obtained in previous thesis Epiney (2015) are valid, they were not in the load multiplier format as required by equation (59). The exported values, from LTBeamN, were the critical bending moments M_{cr}. Therefore, slight adaptations of those results have been made to calculate the original overall critical load factors R_{cr}. Epiney (2015) conducted a validation study on the critical bending moments calculated using LTBeamN. Therefore, this study will consider the results as verified and valid. Further details on this subject can be found in Epiney (2015).

5.2.2 – Calculation of the ultimate global resistance load multipliers (R_u)

The ultimate capacity load multipliers $R_{u(N,M,V)}$ have been calculated in previous studies and properly incorporated the effect of shear loads. The calculations were performed using the finite element analysis FINELg. The ultimate member resistance results, calculated using shell elements, are already in the proper load multiplier format R_u. The shell finite elements may withstand axial and shear stresses. Therefore, the ultimate load multipliers already included the axial, bending and shear loads influence. Although not all simulations provided valid results. Some simulations did not converge properly, and some were invalidated by some "cable effect" phenomenon. These results were carefully discarded from this study. The modeling and analysis details are provided in the thesis of Vincent Epiney and will not be detailed furthermore here.

5.2.3 – Calculation of the cross-section plastic capacity load multipliers (R_{pl})

The plastic capacity load multipliers will be calculated using R_{pl} 2.0. The cross-section plastic capacity calculations, when considering shear loads, are not as straightforward as for member under bending and axial loads only. Bending and shear internal forces diagrams, for cases q1 to q3 are shown in Figure 62. Because the bending and shear internal forces reach their maximum at different positions along the member, it is difficulty to determine which internal force governs the plastic resistance of the member. For constant transverse loading, the maximum bending moment is positioned at the middle of the member and varies, until it reaches zero at the member ends, parabolically. Contrarily to the bending distribution, the maximum shear internal force is positioned at the member supports. The shear forces vary linearly along the member length, reaching a value of zero at the middle of the member. Thus, multiple calculation points must be considered to determine the critical cross-section position under shear and bending loads. Cross-section plastic capacities were calculated at evenly spaced sections along half of the member (from L=0 to L=L/2). The internal forces symmetry permitted to verify only half of the member length. With the calculated cross-section plastic capacities, the most critical plastic capacity factor R_{pl} was chosen.

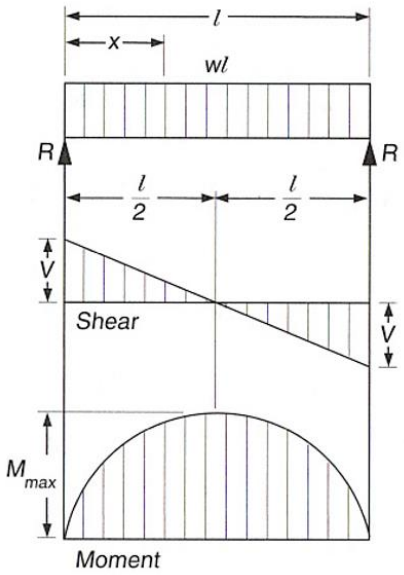

Figure 62 – Bending and shear internal forces distribution for a uniform load on a simply supported member (Canadian Institute of Steel Construction, 2010)

Thanks to R_{pl} *2.0* new possibilities, a complete reprocessing of the numerical simulations was carried out. No additional simulations have been performed. Using equations (59) and (60), the treatment of the results will be more consistent for cases with transverse loads. The following section will describe the numerical simulations of the study.

5.3 – Description of the numerical simulation properties and geometries

This section will describe the various studied models. Four cross-sections and two steel grades will be studied. Table 14 presents the studied member lengths for each cross-section. The steel grades have a Young's modulus E of 210 000 MPa and yield strengths f_y of 355 and 460 MPa. For each cross-section configurations, five load cases will be studied (q1 to q5), as shown in Figure 60. Each of these load cases will be studied for i) varying axial load ratios β as described in equation (61) and for varying member lengths. In total, 1920 numerical simulations have been performed.

Table 14 – Studied cross-sections and their respective lengths

Length [m]	IPE 300	IPE 500	HEB 300	HEB 500
1	x			
2	x	x	x	x
3.5	x	x	x	x
5	x	x	x	x
8	x	x	x	x
10	x	x	x	x
15	x	x	x	x
20	x	x	x	x
25		x	x	x

For each case, the tensile load intensities, were varied according to factor β, as shown in equation (61).

$$\beta = \frac{N_t}{M_z} \tag{61}$$

where N_t is the applied tension load and M_z is the applied bending moment. The tension loading, for various β values, is function of the applied bending moment. The bending moment M_z corresponds to the maximum bending moment at the middle of the member. The ratios β are 0, 0.5, 0.75, 1.0, 1.25 and 1.5. The load combinations were generated to obtain the same maximum bending moment at the center of the members. Because of the various model lengths, the transversal loads applied to the members varied. To attain the given bending moment, shorter beams required a higher intensity of the transversal loads compared to longer members. Therefore, even tough the same maximum bending moment is reached for all members, the load combinations vary. High transversal loads on shorter members will generate high shear internal forces near the supports. Contrarily, lower transversal loads on longer members will generate less internal shear forces near the supports.

The resistance results λ_G and χ_G are obtained following the general steps below:

I. Determine the applied bending moment of the member M_z;

II. Using M_z, the axial load intensities are defined using equation (61). The axial load is constant along the length of the member. The equivalent uniform transversal load q required to reach M_z is calculated;

III. The axial, bending and shear internal forces are calculated at multiple calculations points along the member;

IV. Using the load combinations above, $R_{cr(N,M,V)}$ and $R_{u(N,M,V)}$ values are calculated;

V. Using R_{pl} 2.0, $R_{pl(N,M,V)}$ values are calculated at every calculation point and the critical value is selected. More details on the calculation of R_{pl} values will be presented later;

VI. With $R_{cr(N,M,V)}$, $R_{u(N,M,V)}$ and $R_{pl(N,M,V)}$, the λ_G and χ_G values are calculated.

The section below will describe the procedure used to determine the proper load multiplier R_{pl}.

5.3.1 – Cross-section plastic capacities for $N + M_z + V_y$ load cases

The plastic capacity results calculated using R_{pl} 2.0 will be compared to results obtained in previous works. To properly compare the results, the plastic bending capacities calculated by Epiney (2015) will be transformed into load multipliers. The cross-section plastic capacities $M_{pl,N,Rk}$ were obtained by multiplying the input bending moment by the load factor obtained in R_{pl} *1.0*. Table 15 to Table 18 presents, for all cross-sections ($f_y = 355\ MPa$), the previously-calculated bending moment capacities and their respective plastic capacity load factors. Then, a comparison with the factors obtained with R_{pl} *2.0* and the original load factors will be performed to ensure a coherent continuity of the study. Also, the comparison will indicate which models are the most affected by the shear loading. The complete results tables, for all lengths and materials, can be found in Annex A.

Table 15 – Cross-section plastic capacities of the HEB 300 with f_y = 355 MPa

HEB 300							
		β = 0	β = 0.5	β = 0.75	β = 1.0	β = 1.25	β = 1.5
L = 2m	M_{pl} [kN-m]	663.6	656.8	648.5	637.8	624.6	610.9
	R_{pl} [-]	5.0	5.3	5.4	5.4	5.4	5.5
	R_{pl} *2.0* [-]	2.4	2.6	2.7	2.7	2.8	2.9
	ΔR_{pl} [-]	-51.5%	-51.0%	-50.3%	-49.6%	-48.6%	-47.5%
L = 3.5m	M_{pl} [kN-m]	663.6	656.8	648.5	637.8	624.6	610.9
	R_{pl} [-]	5.0	5.3	5.3	5.4	5.4	5.5
	R_{pl} *2.0* [-]	4.2	4.5	4.6	4.8	4.9	5.0
	ΔR_{pl} [-]	-15.1%	-14.3%	-13.3%	-12.1%	-10.5%	-8.8%
L = 5m	M_{pl} [kN-m]	663.6	656.8	648.5	637.8	624.6	610.9
	R_{pl} [-]	5.0	5.3	5.3	5.4	5.4	5.5
	R_{pl} *2.0* [-]	5.0	5.3	5.4	5.5	5.5	5.5
	ΔR_{pl} [-]	0.9%	1.2%	0.9%	0.8%	0.8%	0.6%

Table 16 - Cross-section plastic capacities of the HEB 500 with f_y = 355 MPa

HEB 500							
		β = 0	β = 0.5	β = 0.75	β = 1.0	β = 1.25	β = 1.5
L = 2m	M_{pl} [kN-m]	1709.4	1676.7	1636.2	1587.1	1531.4	1472.1
	R_{pl} [-]	5.0	5.4	5.5	5.6	5.6	5.6
	R_{pl} *2.0* [-]	2.1	2.3	2.4	2.5	2.6	2.7
	ΔR_{pl} [-]	-59.0%	-58.2%	-57.2%	-55.9%	-54.4%	-52.7%
L = 3.5m	M_{pl} [kN-m]	1709.4	1676.7	1636.2	1587.1	1531.4	1472.1
	R_{pl} [-]	5.0	5.4	5.5	5.6	5.6	5.6
	R_{pl} *2.0* [-]	3.6	3.9	4.1	4.3	4.4	4.6
	ΔR_{pl} [-]	-28.2%	-27.0%	-25.4%	-23.4%	-21.0%	-18.4%
L = 5m	M_{pl} [kN-m]	1709.4	1676.7	1636.2	1587.1	1531.4	1472.1
	R_{pl} [-]	5.0	5.4	5.5	5.6	5.6	5.6
	R_{pl} *2.0* [-]	5.1	5.5	5.6	5.6	5.7	5.7
	ΔR_{pl} [-]	0.9%	0.9%	0.8%	1.0%	0.8%	0.7%

Table 17 - Cross-section plastic capacities of the IPE 300 with f_y = 355 MPa

IPE 300							
		β = 0	β = 0.5	β = 0.75	β = 1.0	β = 1.25	β = 1.5
L = 1m	M_{pl} [kN-m]	223.1	221.9	220.4	218.5	215.9	213.0
	R_{pl} [-]	5.0	5.3	5.4	5.5	5.5	5.6
	R_{pl} *2.0* [-]	2.4	2.5	2.6	2.6	2.7	2.8
	ΔR_{pl} [-]	-52.6%	-52.4%	-52.1%	-51.7%	-51.1%	-50.5%
L = 2m	M_{pl} [kN-m]	223.1	221.9	220.4	218.5	215.9	213.0
	R_{pl} [-]	5.0	5.3	5.4	5.5	5.5	5.6
	R_{pl} *2.0* [-]	4.7	5.0	5.1	5.3	5.4	5.5
	ΔR_{pl} [-]	-5.2%	-4.8%	-4.3%	-3.8%	-2.9%	-1.9%
L = 3.5m	M_{pl} [kN-m]	223.1	221.9	220.4	218.5	215.9	213.0
	R_{pl} [-]	5.0	5.3	5.4	5.5	5.5	5.6
	R_{pl} *2.0* [-]	5.0	5.3	5.4	5.5	5.5	5.6
	ΔR_{pl} [-]	-0.1%	-0.1%	-0.1%	-0.2%	-0.1%	-0.1%

Table 18 - Cross-section plastic capacities of the IPE 500 with f_y = 355 MPa

IPE 500							
		β = 0	β = 0.5	β = 0.75	β = 1.0	β = 1.25	β = 1.5
L = 2m	M_{pl} [kN-m]	779.0	768.9	756.7	740.9	722.6	703.1
	R_{pl} [-]	5.0	5.4	5.5	5.7	5.7	5.8
	R_{pl} *2.0* [-]	3.3	3.6	3.7	3.9	4.0	4.1
	ΔR_{pl} [-]	-34.9%	-34.1%	-33.2%	-31.9%	-30.5%	-28.9%
L = 3.5m	M_{pl} [kN-m]	779.0	768.9	756.7	740.9	722.6	703.1
	R_{pl} [-]	5.0	5.4	5.5	5.7	5.7	5.8
	R_{pl} *2.0* [-]	5.0	5.4	5.5	5.7	5.7	5.8
	ΔR_{pl} [-]	-0.1%	-0.2%	-0.1%	-0.1%	-0.2%	-0.3%
L = 5m	M_{pl} [kN-m]	779.0	768.9	756.7	740.9	722.6	703.1
	R_{pl} [-]	5.0	5.4	5.5	5.7	5.7	5.8
	R_{pl} *2.0* [-]	5.0	5.4	5.5	5.7	5.7	5.8
	ΔR_{pl} [-]	-0.1%	-0.2%	-0.1%	-0.1%	-0.2%	-0.3%

Table 15 to Table 18 show major differences in cross-section plastic capacities when shear is considered. The shear loads influence on the plastic capacity results is particularly noticeable for shorter spans. For spans of 2 meters, the maximum variation, from the original results, is a decrease of approximately 59 % for the HEB 500. The minimum variation corresponds to a decrease of 28.9 % for the IPE 500. These results clearly indicate that for shorter spans, shear loads near the supports govern the plastic resistance of the members. A similar tendency of overestimating the cross-section plastic capacities is observed for spans of 3.5 meters, although less pronounced. Table 15 to Table 18 also show that, for higher β values, the plastic capacity variations reduce slightly.

For longer spans, the member plastic capacity is still governed by bending and axial internal forces, thus the similarity in the plastic capacities results. Therefore, for cases with longer spans, λ_G and χ_G values are not expected to change.

From equations (59) and (60), hypothesis may be drawn to explain the imprecise results shown in Figure 61. A basic observation is that data points have either a slenderness λ_G or a calculated value χ_G that is much smaller than their true values. Because the plastic capacity multiplier R_{pl} is present in both equations, this factor will influence both λ_G and χ_G. In equation (59), for the slenderness of the member to increase, the plastic capacity factor must increase. In equation (60), for the variable χ_G to increase, the plastic capacity must decrease. By incorporating the shear effect on the plastic capacity calculations of cross-sections, the plastic load multiplier is expected to decrease, thus decreasing the slenderness λ_G and increasing χ_G. Because the load multiplier R_{pl} is under a square root in equation (59), a reduction of R_{pl} will induce, simultaneously, a slight decrease in the slenderness but an increase of χ_G.

Using the calculated plastic capacity multipliers, the next section will show the obtained resistance curves calculated using equation (59) and (60).

5.4 – Analysis of λ_G and χ_G results and discussion

This section analyzes the λ_G and χ_G results obtained using the modified plastic capacity multipliers. To see the great improvement of the results, Figure 63 may be compared to the initial results shown in Figure 64. Most of the results under the EC3 curve, as seen in Figure 64, are now directly positioned on the general trend of the resistance curve. The results under the curve, obtained in Epiney (2015), were indeed caused by the omission of the shear loads in the plastic capacity calculations of the cross-sections. To support that fact, Figure 63 shows that the numerical simulations, for high slenderness members, were generally unaffected by the new formulation. Even though that the resistance results now follow the same general trend, multiple buckling curves may be required to properly characterize the member response for low slenderness λ_G values. Detailed figures for the individual cases q1 to q5 will be shown later.

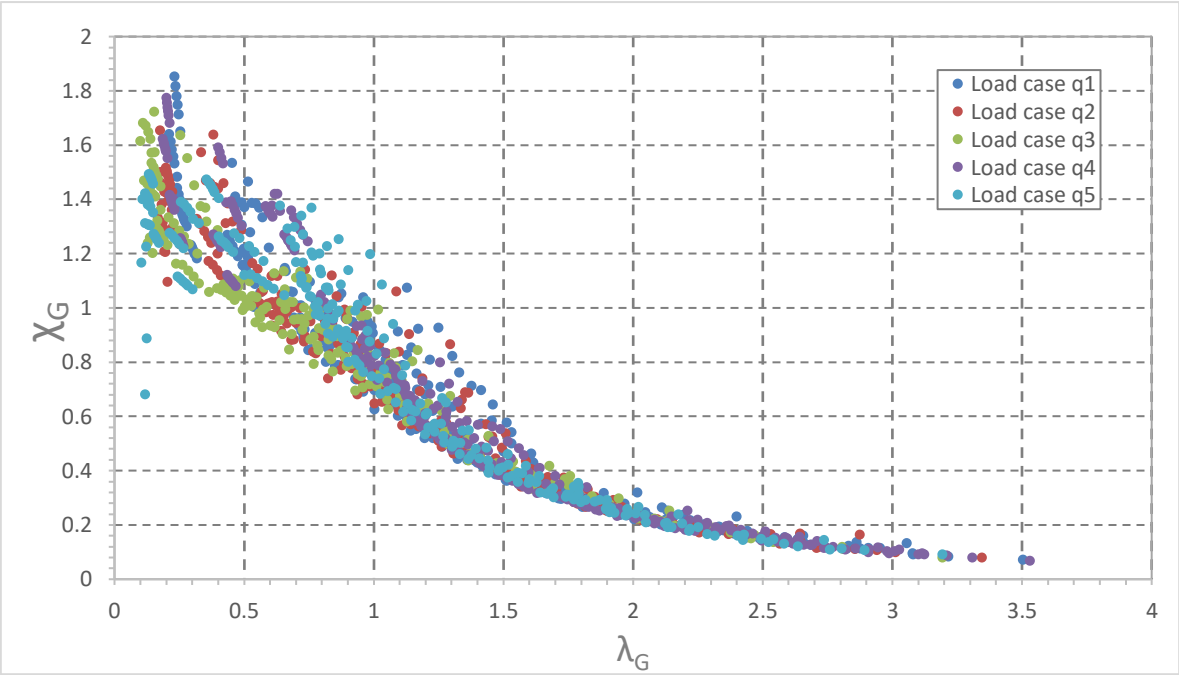

Figure 63 – Results for load cases q1 to q5 considering the shear effects

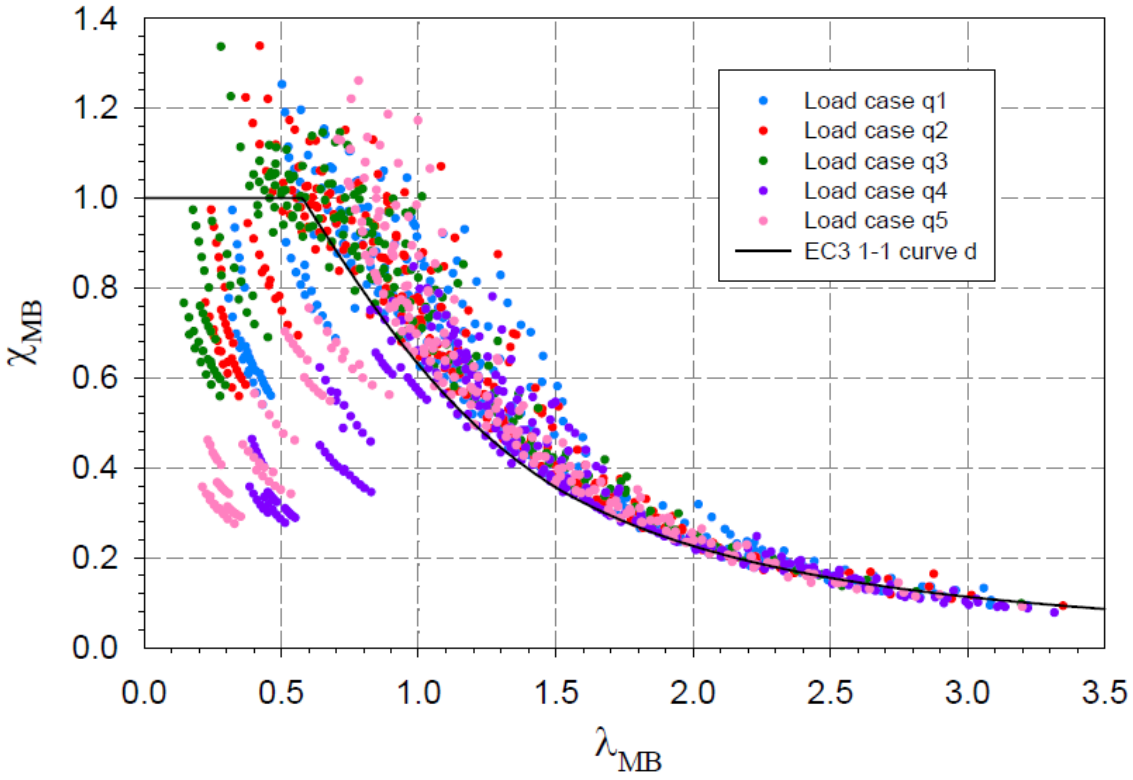

Figure 64- Initial results for load cases q1 to q5

To simplify the analysis of the results, Figure 65 displays the resistance curve results obtained for a specific case. The figure presents the results for the IPE cross-sections for load case q1 and ($\beta = 0.5$). That figure also contains the results obtained in Epiney (2015). The data points that have been affected the most are highlighted on the figure and are detailed in Table 19.

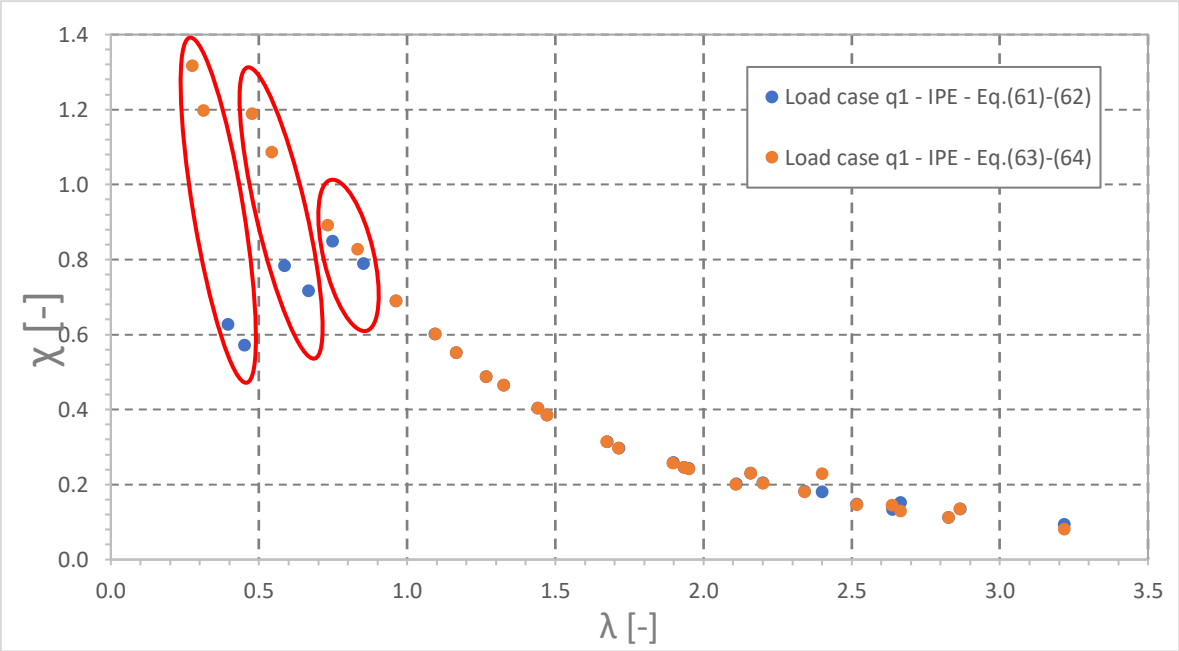

Figure 65 – Resistance curve results comparison for load case q1 - IPE

Figure 65 clearly shows that high slenderness members are practically not affected by the shear loads as the results are nearly identical. However, the new formulation of this study corrected the results of low slenderness members. The results for low slenderness members are now following the general trend of the resistance curve. Table 19 compares the results obtained considering axial and bending forces (N+M) and results obtained considering axial, bending and shear forces (N+M+V).

Table 19 - Comparison of previous and new data points obtained for load case q1 - IPE

Section	L [m]	f_y [MPa]	λ_{N+M} [-]	χ_{N+M} [-]	λ_{N+M+V} [-]	χ_{N+M+V} [-]	ΔR_{pl} [%]	$\Delta\lambda$ [%]	$\Delta\chi$ [%]
IPE 300	1	355	0.396	0.627	0.274	1.317	-52.36	-30.81	110.05
IPE 300	1	460	0.451	0.571	0.311	1.198	-52.34	-31.04	109.81
IPE 300	2	355	0.749	0.849	0.731	0.893	-4.84	-2.40	5.18
IPE 300	2	460	0.853	0.789	0.832	0.829	-4.79	-2.46	5.07
IPE 500	2	355	0.587	0.784	0.477	1.190	-34.09	-18.74	51.79
IPE 500	2	460	0.668	0.716	0.543	1.087	-34.07	-18.71	51.82

By considering the shear forces on the plastic capacity of the cross-sections, the slenderness λ_G has decreased by as much as 30.8% for the IPE 300 members of length of 1 meter. The χ_G parameter, that relates the member cross-section plastic capacities to the ultimate resistance of the beam, has drastically increased by 110%. The slenderness reduction is due to a decrease in member plastic capacity. This indicates that, for stocky members, the overall resistance is governed by the fully plastic region of the buckling curve.

Although the results have been detailed for specific cases, this behavior may be observed for all other results. Figure 66 to Figure 75 present the charts obtained in this study and their respective comparative charts of previous results. These figures present the entirety of the numerical simulations obtained for cases q1 to q5.

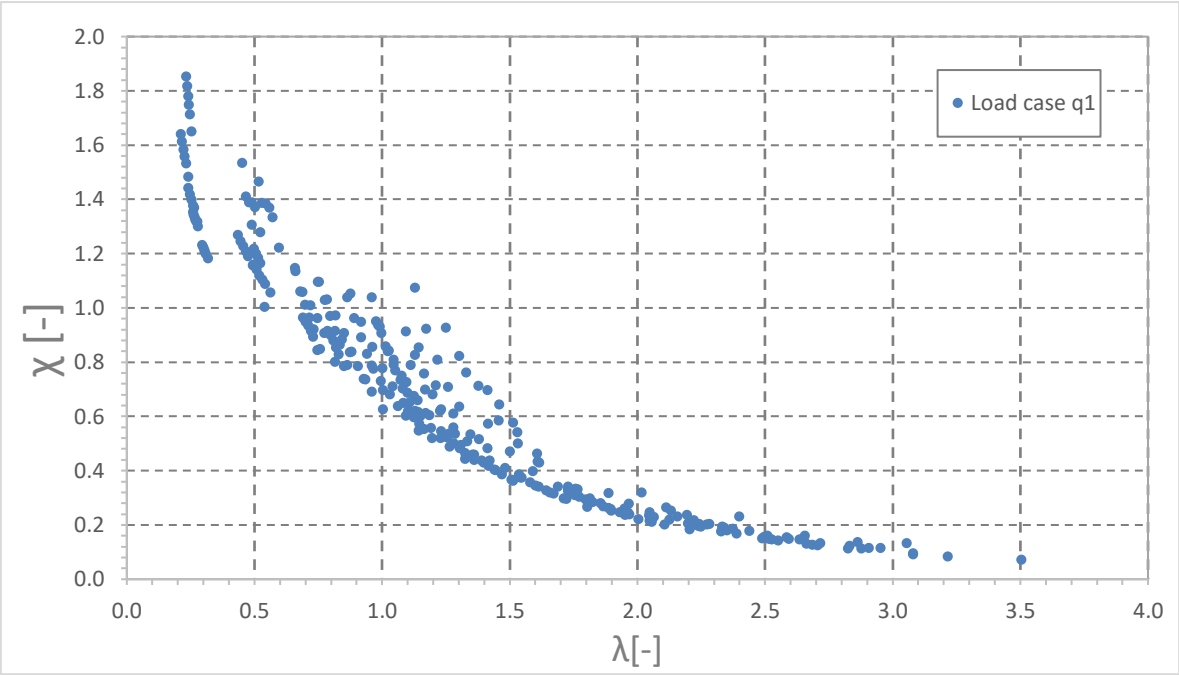

Figure 66 - Resistance curve results for all q1 load cases

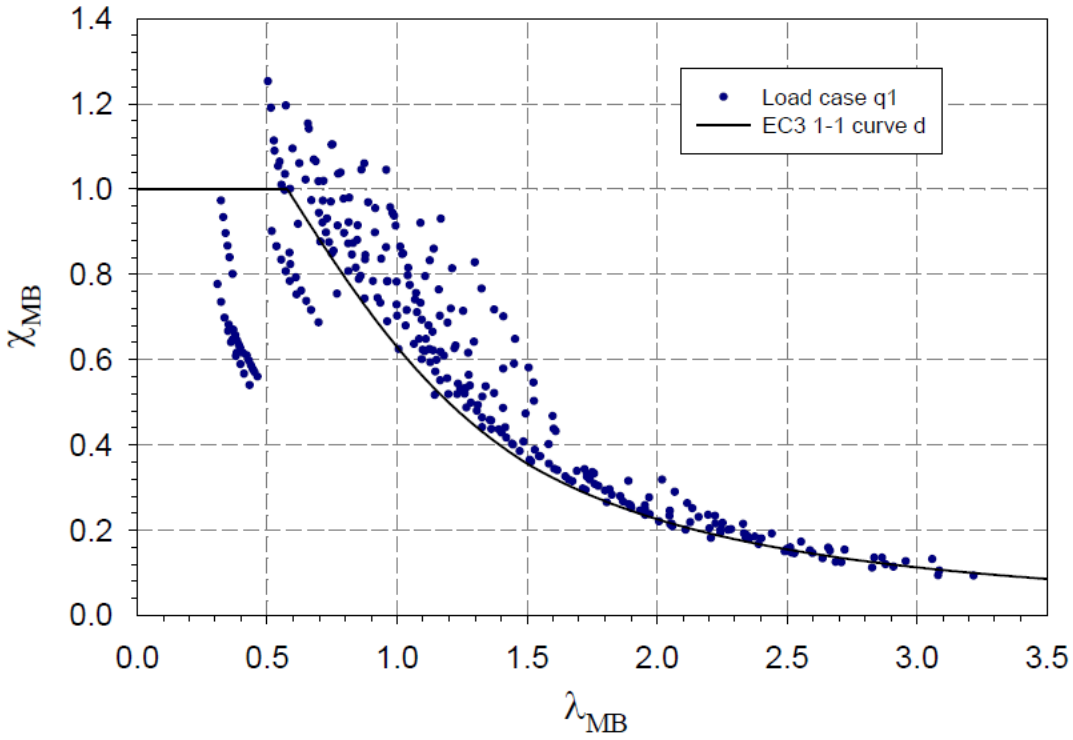

Figure 67 - Resistance curve results for all q1 load cases obtained by Epiney (2015)

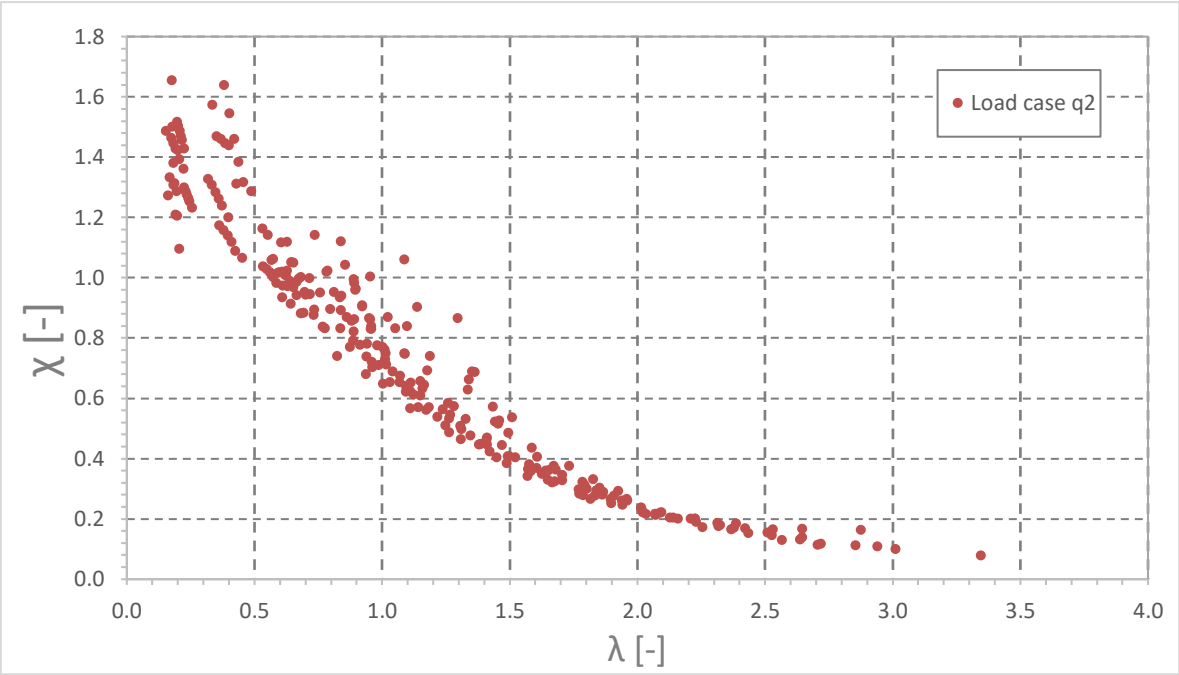

Figure 68- Resistance curve results for all q2 load cases

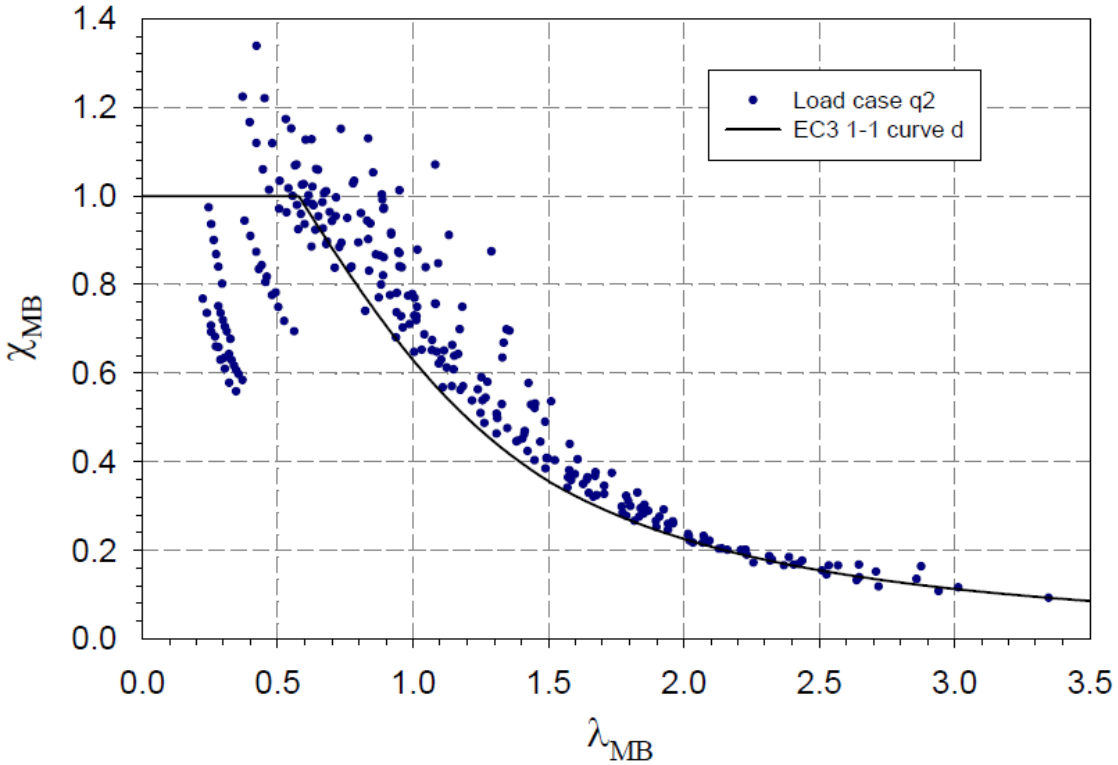

Figure 69 - Resistance curve results for all q2 load cases obtained by Epiney (2015)

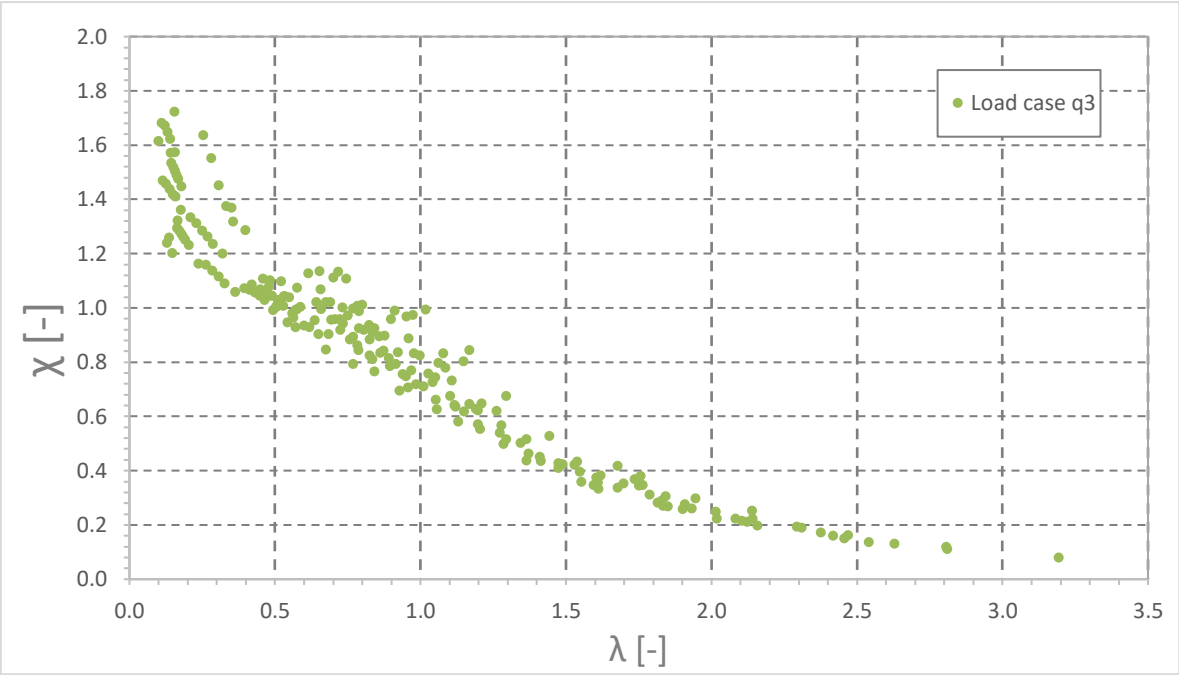

Figure 70- Resistance curve results for all q3 load cases

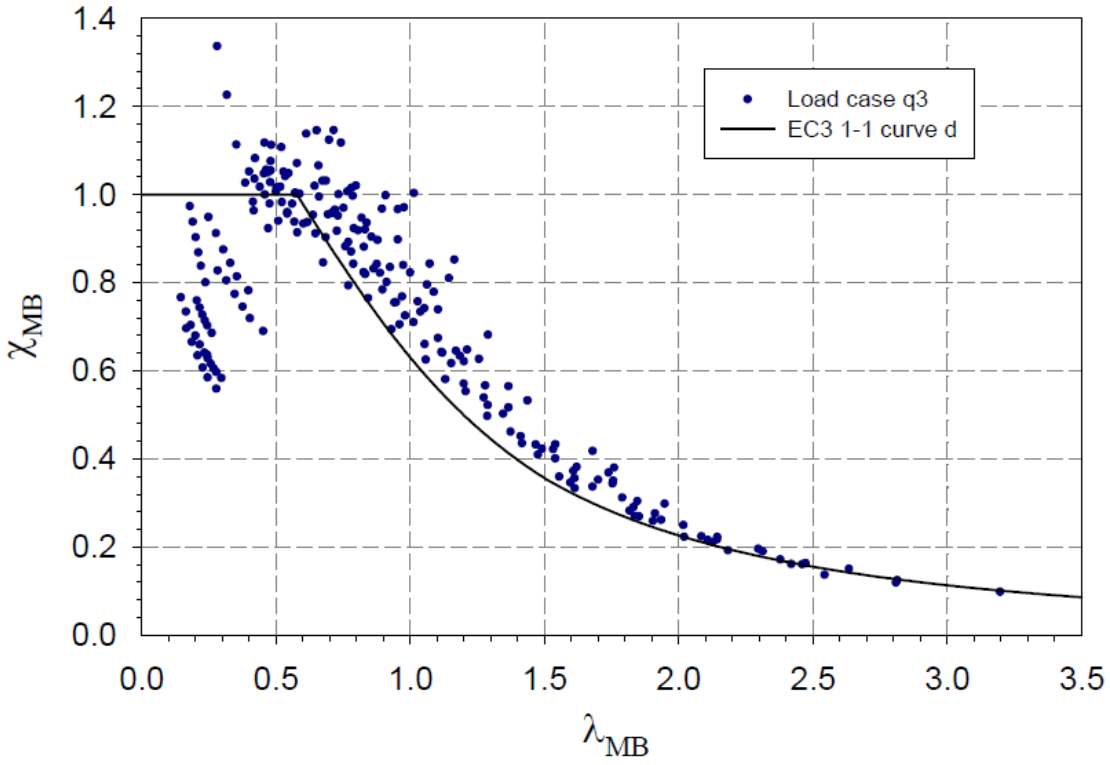

Figure 71 - Resistance curve results for all q3 load cases obtained by Epiney (2015)

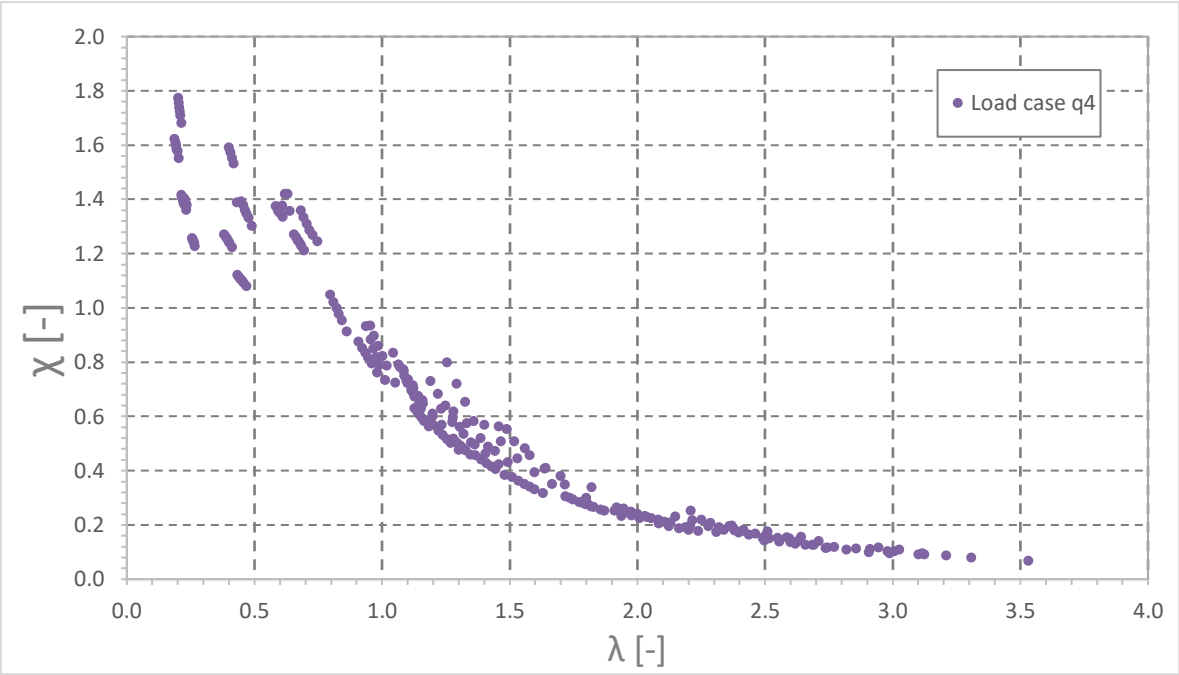

Figure 72 - Resistance curve results for all q4 load cases

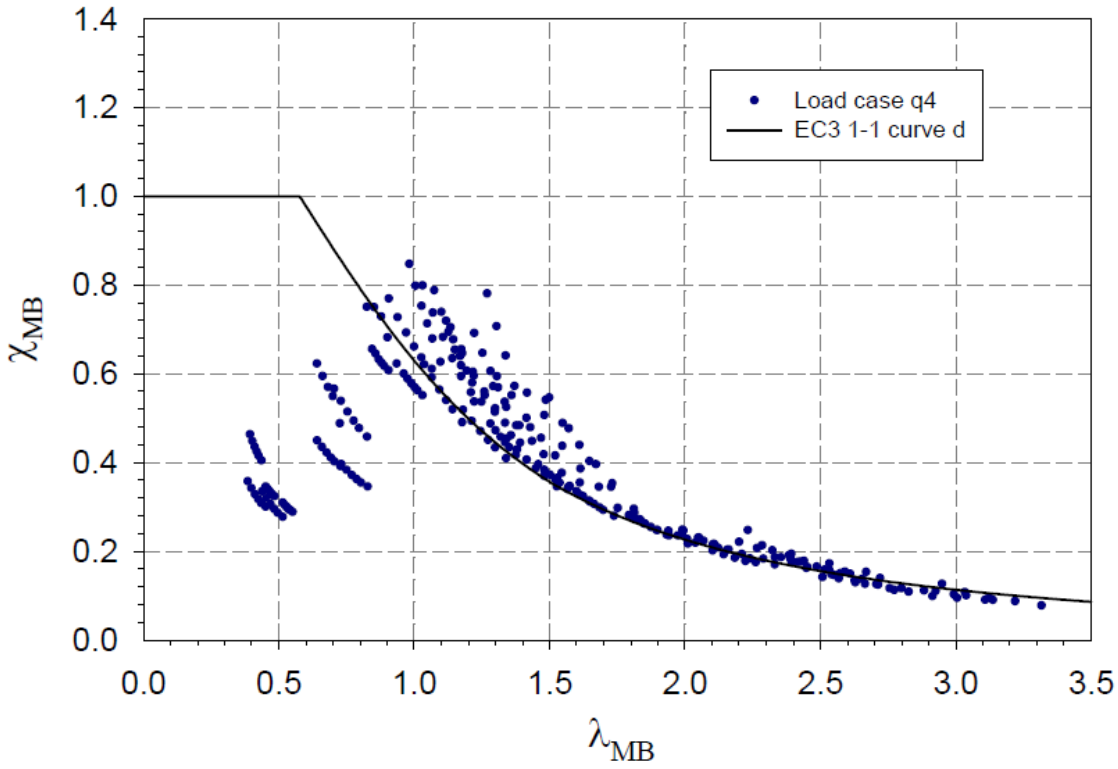

Figure 73 - Resistance curve results for all q3 load cases obtained by Epiney (2015)

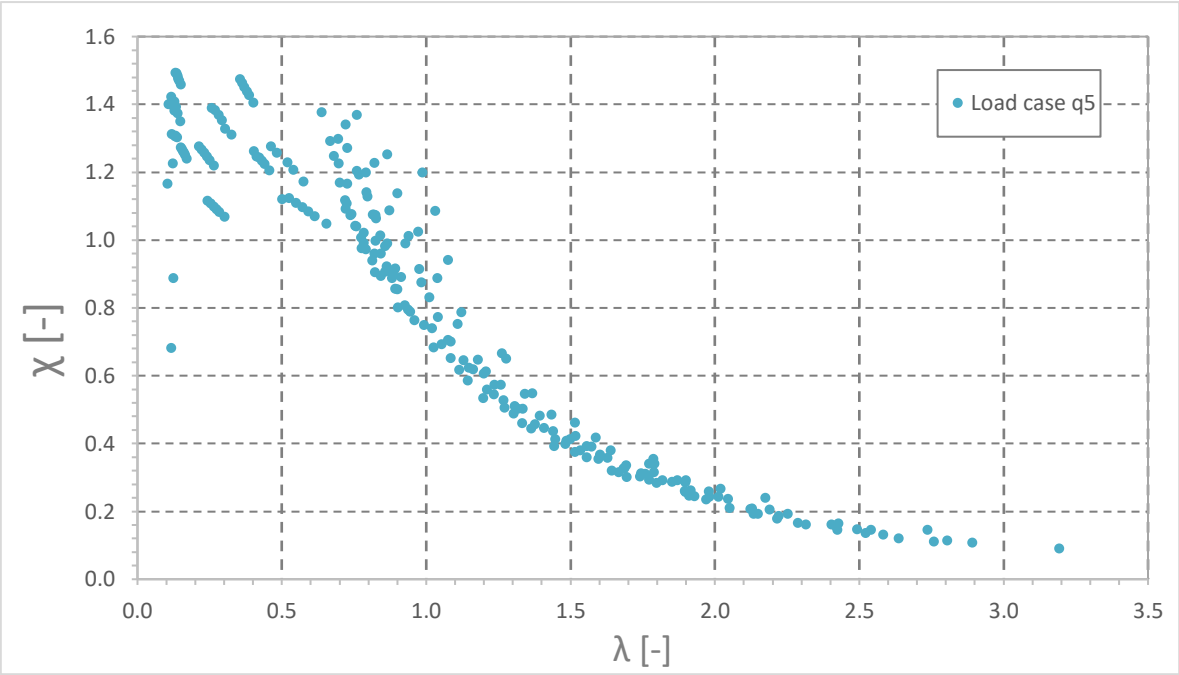

Figure 74 - Resistance curve results for all q5 load cases

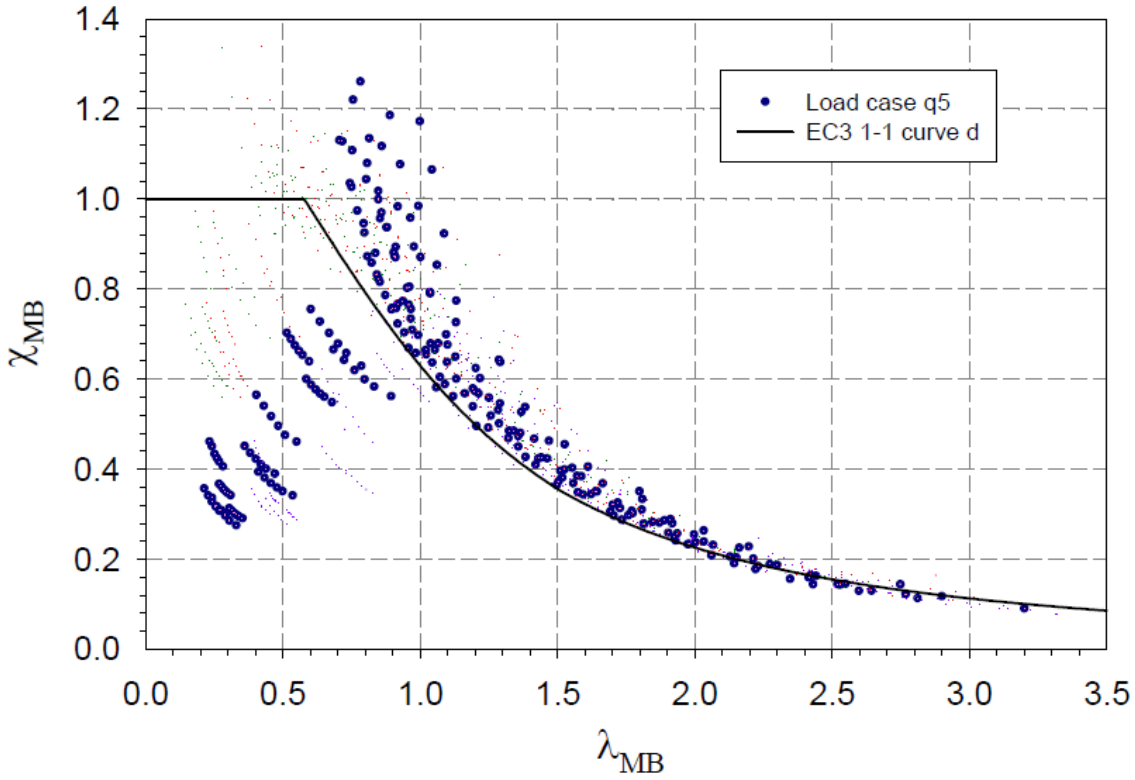

Figure 75 - Resistance curve results for all q5 load cases obtained by Epiney (2015)

This study demonstrated that the plastic resistance of short members is highly influenced by the shear forces near the supports. Multiple numerical tests have confirmed that using reduced bending moment plastic capacities values for short members is not valid. To demonstrate the influence of shear, members of various lengths have been studied. The ultimate resistance behavior of a member largely depends on its length. For short members, the ultimate failure behavior is characterized by the exhaustion of the member plastic capacities. Therefore, for stocky members, using a reduced plastic bending moment, including axial loads only, is not coherent with the failure pattern. To correct this problem, the plastic capacity multiplier, including the axial and shear loads was used. Low slenderness members are generally shorter members with a very high critical stability factor R_{cr}. Short members are not prone to lateral torsional buckling, thus having a higher critical stability factor than slender members. These low slenderness members were the ones with the challenging results, as the effect of shear becomes non-negligible. The high transversal load intensities, for short members, produced high shear forces near the supports. The plastic capacities of the cross-sections, for those cases, were governed by the shear forces. The plastic capacities calculated in this study, for stocky members, were much lower than previously calculated. The lower plastic capacities decreased the slenderness λ_G and greatly increased the χ_G values.

Conclusion

The first objective was to develop a general numerical tool to calculate the plastic capacity of cross-sections for the O.I.C. methodology. The developed numerical tool has the ability to calculate the plastic capacity of cross-sections under axial loads, bi-axial bending moments and shear loads.

The usability of the initial version of R_{pl} was limited. The numerical tool produced valid plastic capacity results for doubly-symmetric cross-sections. Although, after performing numerical tests, the program was shown to be inaccurate for mono-symmetric cross-sections. Also, the shear stresses were not yet included in the program. Following the objective to have a general numerical tool for the O.I.C. method, the initial version of R_{pl} was not sufficient and a more robust and advanced algorithm was required.

A new version of R_{pl} was developed according to the cross-section tangent stiffness method. This method discretizes the cross-section into fibers and requires a non-linear convergence algorithm, such as a Newton-Raphson approach. The fiber method has multiple advantages such as considering any type of cross-section geometries and accepting custom material laws. In the most general case, each fiber may follow a different material stress-strain law. In the cross-section tangent stiffness method reference articles, only the axial loading and bi-axial bending moments were considered and implemented. The shear stresses were not included in the method. As stated before, the program to be developed required the inclusion of shear stresses. The implementation of the shear stresses into the cross-section tangent stiffness method was done using the general shear stress theory and using the von Mises criterion. With the inclusion of the shear stresses, the numerical tool satisfied the first objective of this work.

Before using the newly developped R_{pl} tool, validation tests were required to ensure the accuracy of the calculated plastic capacities. To validate the results, shell models in ABAQUS were used. The accurary of the ABAQUS shell models were validated with mesh density studies and comparisons to theorical values. Mesh density studies were also performed for R_{pl} 2.0. Then, comparisons between R_{pl} 2.0 and ABAQUS were performed for simple load cases. Also, R_{pl} 2.0 results were compared to theorical values. The results comparison was conclusive as R_{pl} 2.0 results, for simple load cases, were accurate.

Following the objective of having a general numerical tool, R_{pl} 2.0 had to be tested for combined load cases. The validation tests were performed using interaction curves for various load combinations. Interaction curves obtained with R_{pl} were compared to interaction curves calculated using *ABAQUS*. Yet again, the results were satisfactory and the R_{pl} program was ready to be used for the second objective of this work.

The second objective of this work was to study the effect of shear stresses on the buckling curves obtained by (Epiney, 2015). Using the O.I.C. approach to generate the buckling curves of beams in tension and bending, some results did not follow the general buckling curve trend and seemed inaccurate. The transversal loads, used to generate the bending moments, develop shear forces along the beam. The effects of those shear forces on the plastic capacities calculations were not considered due to a lack of numerical tools.

The initial R_{pl} tool used was inaccurate for short beams as it did not consider the shear loads. Using the developed numerical tool, the plastic capacity of cross-sections included the effects of the shear forces and buckling curves were calculated using the new plastic capacity results.

The buckling curves for the various models and load cases were processed using the O.I.C. method and the newly developped R_{pl} 2.0 tool. Initially, the buckling curves were generated by omitting the effects of shear on the plastic capacity of cross-sections. For short members, where the failure is mostly governed by the cross-section ultimate capacity, the consideration of shear forces proved to be crucial. The inaccurate results were indeed caused by the omission of shear stresses when calculating the slenderness λ_G and χ_G. The buckling curves are now much smoother and consistent.

Although R_{pl} answered the problem of the plastic capacity of a cross-section with shear stresses, other development and improvements could be added. Other cross-section geometries could be added to the R_{pl} program. Mono-symmetric C-shape cross-sections could be of general interest. Furthermore, sections with no axis of symmetry, such as L-shape cross-sections, could also be of interest. Although, work must be done to consider the shear stresses in those type of sections. Also, additional internal forces could be considered such as torsion and warping. Torsion effects are particularly important for open cross-sections. As R_{pl} uses a fiber approach, each fiber may have a different material and material stress-strain law. The method would therefore be suitable to calculate the plastic capacity of concrete cross-sections

or composite cross-sections including concrete and steel. Some fibers would follow the material stress-strain law of steel and some of concrete.

Bibliography

ArcelorMittal, A. C. (2009). Profilés et Aciers Marchands. Retrieved from https://sections.arcelormittal.com/repo/Sections/Sections_MB_ArcelorMittal_FR_EN_DE.pdf

Bathe, K.-J. (2014). *Finite Element Procedures* (2nd ed.). Klaus-Jurgen Bathe.

Beaulieu, D., Tremblay, R., & Grondin, G. (2005). *Calcul des charpentes d'acier, Tome I*. (C. I. S. C. Canadian Institute of Steel Construction, Ed.) (2 ème).

Beyer, A. (2018). *On the Design of Steel Members with Open Cross-Sections Subject to Combined Axial Force , Bending and Torsion*. Université de Lorraine.

Boissonnade, N., Hayeck, M., Saloumi, E., & Nseir, J. (2017). An Overall Interaction Concept for an alternative approach to steel members design. *Journal of Constructional Steel Research*, *135*, 199–212. https://doi.org/10.1016/j.jcsr.2017.02.030

Canadian Institute of Steel Construction, C. I. S. C. (2010). *Handbook of Steel Construction - Tenth Edition*. (Canadian Institute of Steel Construction, Ed.).

Chen, W. ., & Han, D. . (1989). *Plasticity for structural engineers*. *Journal of Constructional Steel Research* (Vol. 14). https://doi.org/10.1016/0143-974X(89)90075-8

Chiorean, C. G. (2013). A computer method for nonlinear inelastic analysis of 3D composite steel-concrete frame structures. *Engineering Structures*, *57*, 125–152. https://doi.org/10.1016/j.engstruct.2013.09.025

Craig JR., R. R. (2011). *Mechanics of Materials*. John Wiley & Sons.

Crisfield, M. a M. a. (1991). Non-linear finite element analysis of solids and structures, Volume 1. *East*, *58*, 193–212. https://doi.org/10.1017/CBO9781107415324.004

Epiney, V. (2015). *Résistance et stabilité des éléments en acier fléchis et tendus*. Haute École Spécialisée de Suisse occidentale.

Kindmann, R. (2011). *Steel Structures - Design using FEM*. *Ernst & Sohn*.

Mendelson, A. (1968). *PLASTICITY : Theory and Application*. (Macmillan, Ed.).

Santathadaporn, S., & Chen, W. F. (1971). Tangent stiffness method for biaxial bending, *1971*.

Silva, J. T. M. e. (2013). *I-Steel beams under tension: Lateral torsional buckling , behaviour and design*. Instituto Superior Técnico, Lisboa, Portugal.

Villette, M. (2004). *Analyse critique du traitement de la barre comprimée et fléchie et propositions de nouvelles formulations*. University of Liège.

Annexe A

Table 20 – Cross-section plastic capacities of the HEB 300 with f_y = 355 MPa

		β = 0	β = 0.5	β = 0.75	β = 1.0	β = 1.25	β = 1.5
L = 2m	M_{pl} [kN-m]	663.6	656.8	648.5	637.8	624.6	610.9
	R_{pl} [-]	5.0	5.3	5.3	5.4	5.4	5.5
	R_{pl} *2.0* [-]	2.4	2.6	2.7	2.7	2.8	2.9
	ΔR_{pl} [-]	-51.5%	-51.0%	-50.4%	-49.6%	-48.6%	-47.5%
L = 3.5m	M_{pl} [kN-m]	663.6	656.8	648.5	637.8	624.6	610.9
	R_{pl} [-]	5.0	5.3	5.3	5.4	5.4	5.5
	R_{pl} *2.0* [-]	4.2	4.5	4.6	4.8	4.9	5.0
	ΔR_{pl} [-]	-15.1%	-14.3%	-13.3%	-12.1%	-10.5%	-8.8%
L = 5m	M_{pl} [kN-m]	663.6	656.8	648.5	637.8	624.6	610.9
	R_{pl} [-]	5.0	5.3	5.3	5.4	5.4	5.5
	R_{pl} *2.0* [-]	5.0	5.3	5.4	5.5	5.5	5.5
	ΔR_{pl} [-]	0.9%	1.2%	0.9%	0.8%	0.8%	0.6%
L = 8m	M_{pl} [kN-m]	663.6	656.8	648.5	637.8	624.6	610.9
	R_{pl} [-]	5.0	5.3	5.3	5.4	5.4	5.5
	R_{pl} *2.0* [-]	5.0	5.3	5.4	5.5	5.5	5.5
	ΔR_{pl} [-]	1.0%	1.1%	0.9%	0.9%	0.8%	0.7%
L = 10m	M_{pl} [kN-m]	663.6	656.8	648.5	637.8	624.6	610.9
	R_{pl} [-]	5.0	5.3	5.3	5.4	5.4	5.5
	R_{pl} *2.0* [-]	5.0	5.3	5.4	5.5	5.5	5.5
	ΔR_{pl} [-]	1.0%	1.1%	0.9%	0.9%	0.8%	0.7%
L = 15m	M_{pl} [kN-m]	663.6	656.8	648.5	637.8	624.6	610.9
	R_{pl} [-]	5.0	5.3	5.3	5.4	5.4	5.5
	R_{pl} *2.0* [-]	5.0	5.3	5.4	5.5	5.5	5.5
	ΔR_{pl} [-]	1.0%	1.2%	0.9%	0.9%	0.8%	0.7%
L = 20m	M_{pl} [kN-m]	663.6	656.8	648.5	637.8	624.6	610.9
	R_{pl} [-]	5.0	5.3	5.3	5.4	5.4	5.5
	R_{pl} *2.0* [-]	5.0	5.3	5.4	5.5	5.5	5.5

	ΔR_{pl} [-]	1.0%	1.1%	0.9%	0.9%	0.8%	0.7%
L = 25m	M_{pl} [kN-m]	663.6	656.8	648.5	637.8	624.6	610.9
	R_{pl} [-]	5.0	5.3	5.3	5.4	5.4	5.5
	R_{pl} *2.0* [-]	5.0	5.3	5.4	5.5	5.5	5.5
	ΔR_{pl} [-]	1.0%	1.1%	0.9%	0.9%	0.8%	0.7%

Table 21 - Cross-section plastic capacities of the HEB 300 with f_y = 460 MPa

		β = 0	β = 0.5	β = 0.75	β = 1.0	β = 1.25	β = 1.5
L = 2m	M_{pl} [kN-m]	859.9	851.1	840.8	826.4	809.4	790.4
	R_{pl} [-]	5.0	5.3	5.3	5.4	5.4	5.5
	R_{pl} *2.0* [-]	2.4	2.6	2.7	2.7	2.8	2.9
	ΔR_{pl} [-]	-51.5%	-51.0%	-50.4%	-49.6%	-48.6%	-47.4%
L = 3.5m	M_{pl} [kN-m]	859.9	851.1	840.8	826.4	809.4	790.4
	R_{pl} [-]	5.0	5.3	5.3	5.4	5.4	5.5
	R_{pl} *2.0* [-]	4.2	4.5	4.6	4.8	4.9	5.0
	ΔR_{pl} [-]	-15.1%	-14.3%	-13.4%	-12.1%	-10.5%	-8.7%
L = 5m	M_{pl} [kN-m]	859.9	851.1	840.8	826.4	809.4	790.4
	R_{pl} [-]	5.0	5.3	5.3	5.4	5.4	5.5
	R_{pl} *2.0* [-]	5.0	5.3	5.4	5.5	5.5	5.5
	ΔR_{pl} [-]	0.9%	1.1%	0.8%	0.8%	0.8%	0.8%
L = 8m	M_{pl} [kN-m]	859.9	851.1	840.8	826.4	809.4	790.4
	R_{pl} [-]	5.0	5.3	5.3	5.4	5.4	5.5
	R_{pl} *2.0* [-]	5.0	5.3	5.4	5.5	5.5	5.5
	ΔR_{pl} [-]	0.9%	1.1%	0.8%	0.9%	0.8%	0.8%
L = 10m	M_{pl} [kN-m]	859.9	851.1	840.8	826.4	809.4	790.4
	R_{pl} [-]	5.0	5.3	5.3	5.4	5.4	5.5
	R_{pl} *2.0* [-]	5.0	5.3	5.4	5.5	5.5	5.5
	ΔR_{pl} [-]	1.0%	1.2%	0.8%	0.9%	0.8%	0.8%
L = 15m	M_{pl} [kN-m]	859.9	851.1	840.8	826.4	809.4	790.4
	R_{pl} [-]	5.0	5.3	5.3	5.4	5.4	5.5

	R_{pl} *2.0* [-]	5.0	5.3	5.4	5.5	5.5	5.5
	ΔR_{pl} [-]	1.0%	1.2%	0.8%	0.9%	0.8%	0.8%
L = 20m	M_{pl} [kN-m]	859.9	851.1	840.8	826.4	809.4	790.4
	R_{pl} [-]	5.0	5.3	5.3	5.4	5.4	5.5
	R_{pl} *2.0* [-]	5.0	5.3	5.4	5.5	5.5	5.5
	ΔR_{pl} [-]	1.0%	1.2%	0.8%	0.9%	0.8%	0.8%
L = 25m	M_{pl} [kN-m]	859.9	851.1	840.8	826.4	809.4	790.4
	R_{pl} [-]	5.0	5.3	5.3	5.4	5.4	5.5
	R_{pl} *2.0* [-]	5.0	5.3	5.4	5.5	5.5	5.5
	ΔR_{pl} [-]	1.0%	1.1%	0.8%	0.9%	0.8%	0.8%

Table 22 - Cross-section plastic capacities of the HEB 500 with f_y = 355 MPa

		β = 0	β = 0.5	β = 0.75	β = 1.0	β = 1.25	β = 1.5
L = 2m	M_{pl} [kN-m]	1709.4	1676.7	1636.2	1587.1	1531.4	1472.1
	R_{pl} [-]	5.0	5.4	5.5	5.6	5.6	5.6
	R_{pl} *2.0* [-]	2.1	2.3	2.4	2.5	2.6	2.7
	ΔR_{pl} [-]	-59.0%	-58.2%	-57.2%	-55.9%	-54.4%	-52.7%
L = 3.5m	M_{pl} [kN-m]	1709.4	1676.7	1636.2	1587.1	1531.4	1472.1
	R_{pl} [-]	5.0	5.4	5.5	5.6	5.6	5.6
	R_{pl} *2.0* [-]	3.6	3.9	4.1	4.3	4.4	4.6
	ΔR_{pl} [-]	-28.2%	-27.0%	-25.4%	-23.4%	-21.0%	-18.4%
L = 5m	M_{pl} [kN-m]	1709.4	1676.7	1636.2	1587.1	1531.4	1472.1
	R_{pl} [-]	5.0	5.4	5.5	5.6	5.6	5.6
	R_{pl} *2.0* [-]	5.1	5.5	5.6	5.6	5.7	5.7
	ΔR_{pl} [-]	0.9%	0.9%	0.8%	1.0%	0.8%	0.7%
L = 8m	M_{pl} [kN-m]	1709.4	1676.7	1636.2	1587.1	1531.4	1472.1
	R_{pl} [-]	5.0	5.4	5.5	5.6	5.6	5.6
	R_{pl} *2.0* [-]	5.1	5.5	5.6	5.6	5.7	5.7
	ΔR_{pl} [-]	1.0%	0.9%	0.9%	1.0%	0.8%	0.8%
L = 10m	M_{pl} [kN-m]	1709.4	1676.7	1636.2	1587.1	1531.4	1472.1

	R_{pl} [-]	5.0	5.4	5.5	5.6	5.6	5.6
	R_{pl} *2.0* [-]	5.1	5.5	5.6	5.6	5.7	5.7
	ΔR_{pl} [-]	1.0%	0.9%	0.9%	1.1%	0.8%	0.8%
L = 15m	M_{pl} [kN-m]	1709.4	1676.7	1636.2	1587.1	1531.4	1472.1
	R_{pl} [-]	5.0	5.4	5.5	5.6	5.6	5.6
	R_{pl} *2.0* [-]	5.1	5.5	5.6	5.6	5.7	5.7
	ΔR_{pl} [-]	1.0%	1.0%	0.9%	1.0%	0.8%	0.8%
L = 20m	M_{pl} [kN-m]	1709.4	1676.7	1636.2	1587.1	1531.4	1472.1
	R_{pl} [-]	5.0	5.4	5.5	5.6	5.6	5.6
	R_{pl} *2.0* [-]	5.1	5.5	5.6	5.6	5.7	5.7
	ΔR_{pl} [-]	1.0%	1.0%	0.9%	1.0%	0.8%	0.8%
L = 25m	M_{pl} [kN-m]	1709.4	1676.7	1636.2	1587.1	1531.4	1472.1
	R_{pl} [-]	5.0	5.4	5.5	5.6	5.6	5.6
	R_{pl} *2.0* [-]	5.1	5.5	5.6	5.6	5.7	5.7
	ΔR_{pl} [-]	1.0%	1.0%	0.9%	1.0%	0.8%	0.8%

Table 23 - Cross-section plastic capacities of the HEB 500 with f_y = 460 MPa

		β = 0	β = 0.5	β = 0.75	β = 1.0	β = 1.25	β = 1.5
L = 2m	M_{pl} [kN-m]	2215.0	2172.6	2120.1	2056.5	1984.3	1907.5
	R_{pl} [-]	5.0	5.4	5.5	5.6	5.6	5.6
	R_{pl} *2.0* [-]	2.1	2.2	2.4	2.5	2.6	2.7
	ΔR_{pl} [-]	-59.0%	-58.5%	-57.2%	-55.9%	-54.4%	-52.7%
L = 3.5m	M_{pl} [kN-m]	2215.0	2172.6	2120.1	2056.5	1984.3	1907.5
	R_{pl} [-]	5.0	5.4	5.5	5.6	5.6	5.6
	R_{pl} *2.0* [-]	3.6	3.9	4.1	4.3	4.4	4.6
	ΔR_{pl} [-]	-28.2%	-27.0%	-25.4%	-23.4%	-21.0%	-18.4%
L = 5m	M_{pl} [kN-m]	2215.0	2172.6	2120.1	2056.5	1984.3	1907.5
	R_{pl} [-]	5.0	5.4	5.5	5.6	5.6	5.6
	R_{pl} *2.0* [-]	5.1	5.5	5.6	5.6	5.7	5.7
	ΔR_{pl} [-]	0.9%	0.9%	0.8%	0.9%	0.8%	0.7%

L = 8m	M_{pl} [kN-m]	2215.0	2172.6	2120.1	2056.5	1984.3	1907.5
	R_{pl} [-]	5.0	5.4	5.5	5.6	5.6	5.6
	R_{pl} *2.0* [-]	5.1	5.5	5.6	5.6	5.7	5.7
	ΔR_{pl} [-]	1.0%	1.0%	0.9%	1.2%	0.8%	0.8%
L = 10m	M_{pl} [kN-m]	2215.0	2172.6	2120.1	2056.5	1984.3	1907.5
	R_{pl} [-]	5.0	5.4	5.5	5.6	5.6	5.6
	R_{pl} *2.0* [-]	5.1	5.5	5.6	5.6	5.7	5.7
	ΔR_{pl} [-]	1.0%	0.9%	0.9%	1.1%	0.8%	0.8%
L = 15m	M_{pl} [kN-m]	2215.0	2172.6	2120.1	2056.5	1984.3	1907.5
	R_{pl} [-]	5.0	5.4	5.5	5.6	5.6	5.6
	R_{pl} *2.0* [-]	5.1	5.5	5.6	5.6	5.7	5.7
	ΔR_{pl} [-]	1.0%	1.0%	0.9%	1.0%	0.8%	0.8%
L = 20m	M_{pl} [kN-m]	2215.0	2172.6	2120.1	2056.5	1984.3	1907.5
	R_{pl} [-]	5.0	5.4	5.5	5.6	5.6	5.6
	R_{pl} *2.0* [-]	5.1	5.5	5.6	5.6	5.7	5.7
	ΔR_{pl} [-]	1.0%	0.9%	0.9%	1.0%	0.8%	0.8%
L = 25m	M_{pl} [kN-m]	2215.0	2172.6	2120.1	2056.5	1984.3	1907.5
	R_{pl} [-]	5.0	5.4	5.5	5.6	5.6	5.6
	R_{pl} *2.0* [-]	5.1	5.5	5.6	5.6	5.7	5.7
	ΔR_{pl} [-]	1.0%	0.9%	0.9%	1.0%	0.8%	0.8%

Table 24 - Cross-section plastic capacities of the IPE 300 with f_y = 355 MPa

		β = 0	β = 0.5	β = 0.75	β = 1.0	β = 1.25	β = 1.5
L = 1m	M_{pl} [kN-m]	223.1	221.9	220.4	218.5	215.9	213.0
	R_{pl} [-]	5.0	5.3	5.4	5.5	5.5	5.6
	R_{pl} *2.0* [-]	2.4	2.5	2.6	2.6	2.7	2.8
	ΔR_{pl} [-]	-52.6%	-52.4%	-52.1%	-51.7%	-51.1%	-50.5%
L = 2m	M_{pl} [kN-m]	223.1	221.9	220.4	218.5	215.9	213.0
	R_{pl} [-]	5.0	5.3	5.4	5.5	5.5	5.6
	R_{pl} *2.0* [-]	4.7	5.0	5.1	5.3	5.4	5.5

	ΔR_{pl} [-]	-5.2%	-4.8%	-4.3%	-3.8%	-2.9%	-1.9%
L = 3.5m	M_{pl} [kN-m]	223.1	221.9	220.4	218.5	215.9	213.0
	R_{pl} [-]	5.0	5.3	5.4	5.5	5.5	5.6
	R_{pl} *2.0* [-]	5.0	5.3	5.4	5.5	5.5	5.6
	ΔR_{pl} [-]	-0.1%	-0.1%	-0.1%	-0.2%	-0.1%	-0.1%
L = 5m	M_{pl} [kN-m]	223.1	221.9	220.4	218.5	215.9	213.0
	R_{pl} [-]	5.0	5.3	5.4	5.5	5.5	5.6
	R_{pl} *2.0* [-]	5.0	5.3	5.4	5.5	5.5	5.6
	ΔR_{pl} [-]	-0.1%	-0.1%	-0.1%	-0.2%	-0.1%	-0.1%
L = 8m	M_{pl} [kN-m]	223.1	221.9	220.4	218.5	215.9	213.0
	R_{pl} [-]	5.0	5.3	5.4	5.5	5.5	5.6
	R_{pl} *2.0* [-]	5.0	5.3	5.4	5.5	5.5	5.6
	ΔR_{pl} [-]	-0.1%	-0.1%	-0.1%	-0.2%	-0.1%	-0.1%
L = 10m	M_{pl} [kN-m]	223.1	221.9	220.4	218.5	215.9	213.0
	R_{pl} [-]	5.0	5.3	5.4	5.5	5.5	5.6
	R_{pl} *2.0* [-]	5.0	5.3	5.4	5.5	5.5	5.6
	ΔR_{pl} [-]	-0.1%	-0.1%	-0.1%	-0.2%	-0.1%	-0.1%
L = 15m	M_{pl} [kN-m]	223.1	221.9	220.4	218.5	215.9	213.0
	R_{pl} [-]	5.0	5.3	5.4	5.5	5.5	5.6
	R_{pl} *2.0* [-]	5.0	5.3	5.4	5.5	5.5	5.6
	ΔR_{pl} [-]	-0.1%	-0.1%	-0.1%	-0.2%	-0.1%	-0.1%
L = 20m	M_{pl} [kN-m]	223.1	221.9	220.4	218.5	215.9	213.0
	R_{pl} [-]	5.0	5.3	5.4	5.5	5.5	5.6
	R_{pl} *2.0* [-]	5.0	5.3	5.4	5.5	5.5	5.6
	ΔR_{pl} [-]	-0.1%	-0.1%	-0.1%	-0.2%	-0.1%	-0.1%

Table 25 - Cross-section plastic capacities of the IPE 300 with f_y = 460 MPa

		β = 0	β = 0.5	β = 0.75	β = 1.0	β = 1.25	β = 1.5
L = 1m	M_{pl} [kN-m]	289.1	287.5	286.0	283.0	279.7	276.0
	R_{pl} [-]	5.0	5.3	5.4	5.5	5.5	5.6

	R_{pl} *2.0* [-]	2.4	2.5	2.6	2.6	2.7	2.8
	ΔR_{pl} [-]	-52.6%	-52.3%	-52.1%	-51.6%	-51.1%	-50.5%
L = 2m	M_{pl} [kN-m]	289.1	287.5	286.0	283.0	279.7	276.0
	R_{pl} [-]	5.0	5.3	5.4	5.5	5.5	5.6
	R_{pl} *2.0* [-]	4.7	5.0	5.1	5.3	5.4	5.5
	ΔR_{pl} [-]	-5.2%	-4.8%	-4.5%	-3.7%	-2.9%	-1.9%
L = 3.5m	M_{pl} [kN-m]	289.1	287.5	286.0	283.0	279.7	276.0
	R_{pl} [-]	5.0	5.3	5.4	5.5	5.5	5.6
	R_{pl} *2.0* [-]	5.0	5.3	5.4	5.5	5.5	5.6
	ΔR_{pl} [-]	-0.2%	-0.2%	-0.3%	-0.2%	-0.2%	-0.2%
L = 5m	M_{pl} [kN-m]	289.1	287.5	286.0	283.0	279.7	276.0
	R_{pl} [-]	5.0	5.3	5.4	5.5	5.5	5.6
	R_{pl} *2.0* [-]	5.0	5.3	5.4	5.5	5.5	5.6
	ΔR_{pl} [-]	-0.2%	-0.2%	-0.3%	-0.2%	-0.2%	-0.2%
L = 8m	M_{pl} [kN-m]	289.1	287.5	286.0	283.0	279.7	276.0
	R_{pl} [-]	5.0	5.3	5.4	5.5	5.5	5.6
	R_{pl} *2.0* [-]	5.0	5.3	5.4	5.5	5.5	5.6
	ΔR_{pl} [-]	-0.2%	-0.2%	-0.3%	-0.2%	-0.2%	-0.2%
L = 10m	M_{pl} [kN-m]	289.1	287.5	286.0	283.0	279.7	276.0
	R_{pl} [-]	5.0	5.3	5.4	5.5	5.5	5.6
	R_{pl} *2.0* [-]	5.0	5.3	5.4	5.5	5.5	5.6
	ΔR_{pl} [-]	-0.2%	-0.2%	-0.3%	-0.2%	-0.2%	-0.2%
L = 15m	M_{pl} [kN-m]	289.1	287.5	286.0	283.0	279.7	276.0
	R_{pl} [-]	5.0	5.3	5.4	5.5	5.5	5.6
	R_{pl} *2.0* [-]	5.0	5.3	5.4	5.5	5.5	5.6
	ΔR_{pl} [-]	-0.2%	-0.2%	-0.3%	-0.2%	-0.2%	-0.2%
L = 20m	M_{pl} [kN-m]	289.1	287.5	286.0	283.0	279.7	276.0
	R_{pl} [-]	5.0	5.3	5.4	5.5	5.5	5.6
	R_{pl} *2.0* [-]	5.0	5.3	5.4	5.5	5.5	5.6
	ΔR_{pl} [-]	-0.2%	-0.2%	-0.3%	-0.2%	-0.2%	-0.2%

Table 26 - Cross-section plastic capacities of the IPE 500 with f_y = 355 MPa

		β = 0	β = 0.5	β = 0.75	β = 1.0	β = 1.25	β = 1.5
L = 2m	M_{pl} [kN-m]	779.0	768.9	756.7	740.9	722.6	703.1
	R_{pl} [-]	5.0	5.4	5.5	5.7	5.7	5.8
	R_{pl} *2.0* [-]	3.3	3.6	3.7	3.9	4.0	4.1
	ΔR_{pl} [-]	-34.9%	-34.1%	-33.2%	-31.9%	-30.5%	-28.9%
L = 3.5m	M_{pl} [kN-m]	779.0	768.9	756.7	740.9	722.6	703.1
	R_{pl} [-]	5.0	5.4	5.5	5.7	5.7	5.8
	R_{pl} *2.0* [-]	5.0	5.4	5.5	5.7	5.7	5.8
	ΔR_{pl} [-]	-0.1%	-0.2%	-0.1%	-0.1%	-0.2%	-0.3%
L = 5m	M_{pl} [kN-m]	779.0	768.9	756.7	740.9	722.6	703.1
	R_{pl} [-]	5.0	5.4	5.5	5.7	5.7	5.8
	R_{pl} *2.0* [-]	5.0	5.4	5.5	5.7	5.7	5.8
	ΔR_{pl} [-]	-0.1%	-0.2%	-0.1%	-0.1%	-0.2%	-0.3%
L = 8m	M_{pl} [kN-m]	779.0	768.9	756.7	740.9	722.6	703.1
	R_{pl} [-]	5.0	5.4	5.5	5.7	5.7	5.8
	R_{pl} *2.0* [-]	5.0	5.4	5.5	5.7	5.7	5.8
	ΔR_{pl} [-]	-0.1%	-0.2%	-0.1%	-0.1%	-0.2%	-0.3%
L = 10m	M_{pl} [kN-m]	779.0	768.9	756.7	740.9	722.6	703.1
	R_{pl} [-]	5.0	5.4	5.5	5.7	5.7	5.8
	R_{pl} *2.0* [-]	5.0	5.4	5.5	5.7	5.7	5.8
	ΔR_{pl} [-]	-0.1%	-0.2%	-0.1%	-0.1%	-0.2%	-0.3%
L = 15m	M_{pl} [kN-m]	779.0	768.9	756.7	740.9	722.6	703.1
	R_{pl} [-]	5.0	5.4	5.5	5.7	5.7	5.8
	R_{pl} *2.0* [-]	5.0	5.4	5.5	5.7	5.7	5.8
	ΔR_{pl} [-]	-0.1%	-0.2%	-0.1%	-0.1%	-0.2%	-0.3%
L = 20m	M_{pl} [kN-m]	779.0	768.9	756.7	740.9	722.6	703.1
	R_{pl} [-]	5.0	5.4	5.5	5.7	5.7	5.8
	R_{pl} *2.0* [-]	5.0	5.4	5.5	5.7	5.7	5.8
	ΔR_{pl} [-]	-0.1%	-0.2%	-0.1%	-0.1%	-0.2%	-0.3%

L = 25m	M_{pl} [kN-m]	779.0	768.9	756.7	740.9	722.6	703.1
	R_{pl} [-]	5.0	5.4	5.5	5.7	5.7	5.8
	R_{pl} *2.0* [-]	5.0	5.4	5.5	5.7	5.7	5.8
	ΔR_{pl} [-]	-0.1%	-0.2%	-0.1%	-0.1%	-0.2%	-0.3%

Table 27 - Cross-section plastic capacities of the IPE 500 with f_y = 460 MPa

		β = 0	β = 0.5	β = 0.75	β = 1.0	β = 1.25	β = 1.5
L = 2m	M_{pl} [kN-m]	1009.4	996.2	980.5	960.1	936.3	910.9
	R_{pl} [-]	5.0	5.4	5.5	5.7	5.7	5.8
	R_{pl} *2.0* [-]	3.3	3.6	3.7	3.9	4.0	4.1
	ΔR_{pl} [-]	-34.9%	-34.1%	-33.2%	-31.9%	-30.5%	-28.9%
L = 3.5m	M_{pl} [kN-m]	1009.4	996.2	980.5	960.1	936.3	910.9
	R_{pl} [-]	5.0	5.4	5.5	5.7	5.7	5.8
	R_{pl} *2.0* [-]	5.0	5.4	5.5	5.7	5.7	5.8
	ΔR_{pl} [-]	-0.1%	-0.1%	-0.1%	-0.1%	-0.2%	-0.3%
L = 5m	M_{pl} [kN-m]	1009.4	996.2	980.5	960.1	936.3	910.9
	R_{pl} [-]	5.0	5.4	5.5	5.7	5.7	5.8
	R_{pl} *2.0* [-]	5.0	5.4	5.5	5.7	5.7	5.8
	ΔR_{pl} [-]	-0.1%	-0.1%	-0.1%	-0.1%	-0.2%	-0.3%
L = 8m	M_{pl} [kN-m]	1009.4	996.2	980.5	960.1	936.3	910.9
	R_{pl} [-]	5.0	5.4	5.5	5.7	5.7	5.8
	R_{pl} *2.0* [-]	5.0	5.4	5.5	5.7	5.7	5.8
	ΔR_{pl} [-]	-0.1%	-0.1%	-0.1%	-0.1%	-0.2%	-0.3%
L = 10m	M_{pl} [kN-m]	1009.4	996.2	980.5	960.1	936.3	910.9
	R_{pl} [-]	5.0	5.4	5.5	5.7	5.7	5.8
	R_{pl} *2.0* [-]	5.0	5.4	5.5	5.7	5.7	5.8
	ΔR_{pl} [-]	-0.1%	-0.1%	-0.1%	-0.1%	-0.2%	-0.3%
L = 15m	M_{pl} [kN-m]	1009.4	996.2	980.5	960.1	936.3	910.9
	R_{pl} [-]	5.0	5.4	5.5	5.7	5.7	5.8
	R_{pl} *2.0* [-]	5.0	5.4	5.5	5.7	5.7	5.8
	ΔR_{pl} [-]	-0.1%	-0.1%	-0.1%	-0.1%	-0.2%	-0.3%

L = 20m	M_{pl} [kN-m]	1009.4	996.2	980.5	960.1	936.3	910.9
	R_{pl} [-]	5.0	5.4	5.5	5.7	5.7	5.8
	R_{pl} *2.0* [-]	5.0	5.4	5.5	5.7	5.7	5.8
	ΔR_{pl} [-]	-0.1%	-0.1%	-0.1%	-0.1%	-0.2%	-0.3%
L = 25m	M_{pl} [kN-m]	1009.4	996.2	980.5	960.1	936.3	910.9
	R_{pl} [-]	5.0	5.4	5.5	5.7	5.7	5.8
	R_{pl} *2.0* [-]	5.0	5.4	5.5	5.7	5.7	5.8
	ΔR_{pl} [-]	-0.1%	-0.1%	-0.1%	-0.1%	-0.2%	-0.3%